Bound excitons and exciton-polaritons in Zinc Oxide

vorgelegt von

Diplom-Physiker

Thomas Kure

ORCID: 0000-0002-6514-422X

von der Fakultät II - Mathematik und Naturwissenschaften

der Technischen Universität Berlin

zur Erlangung des akademischen Grades

Doktor der Naturwissenschaften

- Dr.rer.nat. -

genehmigte Dissertation

Promotionsausschuss:
Vorsitzender: Prof. Dr. Michael Lehmann
Gutachter: Prof. Dr. Axel Hoffmann
Gutachter: Prof. Dr. Markus R. Wagner
Gutachter: Prof. Dr. Jean-Michel Chauveau

Tag der wissenschaftlichen Aussprache: 25. Februar 2022

Berlin 2022

Zusammenfassung

In einer systematischen Untersuchung von Antimon-dotierten Zinkoxid-Nanodrähten mit unterschiedlichen Dotierungskonzentrationen kann eine Emissionslinie in der Photolumineszenz-Spektroskopie bei $3,3642\ \mathrm{eV}$ einem gebundenen Exziton an einer Antimon-Störstelle zugeordnet werden. Durch eine weiterführenden Analyse kann aufgrund des optischen und thermischen Verhaltens gefolgert werden, dass die Emissionslinie die Rekombination eines gebundenes Exzitons an einer neutralen Störstelle ist. Die in der jüngsten Diskussion aufgeworfene Frage, ob diese neue Antimon-Störstelle als Donator oder Akzeptor wirkt, kann eindeutig durch magneto-optische Messungen dieser Linie beantwortet werden, die ein typisches Verhalten eines an einem neutralen Donator gebundenen Exzitons zeigt. Darüber hinaus zeigen ortsaufgelöste Messungen einen höheren Einbau von Antimon an der Spitze der Nanodrähte. Für diese Schlussfolgerung wurden hochauflösende Kathodolumineszenzmessungen in einem Rastertransmissionselektronenmikroskop, Mikrophotolumineszenz, Mikrokathodolumineszenz und spitzenverstärkte Raman-Spektroskopie für einzelne Nanodrähte aufeinander abgeglichen. Für die letztgenannte Messung wurden in der Probe mit Raman-Spektroskopie Antimon-abhängige lokale Schwingungsmoden identifiziert.

Der unbeabsichtigte Einbau von Kohlenstoff und seinen Einfluss auf die optischen Eigenschaften von Antimon-dotierten Nanodrähten wurde untersucht. Durch Co-Dotierung mit Wasserstoff konnte die Emissionsintensität der Nanodrähte drastisch erhöht werden indem die Konzentration nicht-strahlender Rekombinationszentren reduziert und Emissionslinien der Kohlenstoff-dotierung unterdrückt werden. In Kohlenstoff-dotierten Zinkoxid-Nanodrähten wurde das Auftreten von vier Emissionslinien beobachtet, bezeichnet als Z-Linien bei $3,3606\ \mathrm{eV}$, $3,3611\ \mathrm{eV}$, $3,3615\ \mathrm{eV}$, und $3,3618\ \mathrm{eV}$. Diese Linien konnten als Exzitonen an neutralen Donatorzuständen des eingebundenen Kohlenstoffs identifiziert werden. Durch Co-Dotierung mit Wasserstoff wurde ebenfalls die Emissionsintensität erhöht.

Das Konzept von Exziton-Polaritonen basiert auf einer Kopplung von Licht und Exziton. In einer m-plane ZnO-Schicht werden Exziton-Polaritonen in einer Rückstreugeometrie in Photolumineszenz- und Reflexionsmessung sichtbar. In beiden Messungen sind zusätzliche Wellen sichtbar, die als Fabry-Pérot-Interferenzmuster identifiziert wurden. Das Reflexionsvermögen in der Nähe des A- und B-Exzitons wurde durch ein Zwei-Oszillator-Modell modelliert. Als Ergebnis wurde die detaillierte

Exziton-Polariton-Dispersionskurve der oberen, unteren und mittleren Polariton-Zweige berechnet. Die gezeigte geringe Dämpfung der A- und B-Exzitonenmoden ist entscheidend und die Hauptursache dafür, dass das Fabry-Pérot-Interferenzmuster in der m-Plane-Probe auftritt und zuvor nie in der Literatur für ZnO berichtet wurde.

Abstract

In a systematic study of antimony-doped zinc oxide nanowires with different doping concentrations, a distinct emission line in photoluminescence spectroscopy at $3.3642\ \mathrm{eV}$ can be attributed to a bound exciton involving an antimony impurity. In a further analysis, based on its optical and thermal behavior, it can be concluded that the emission line is the recombination of an exciton bound to a neutral impurity. The question raised in the recent discussion whether this new antimony-related impurity acts as a donor or an acceptor can unambiguously be answered by magneto-optical measurements of that particular line that show a typical behavior of an exciton bound to a neutral donor. Moreover, spatially resolved measurements reveal higher incorporation of antimony at the tip of the nanowires. For this conclusion, high-resolution cathodoluminescence measurements in a scanning transmission electron microscope, micro-photoluminescence, micro-cathodoluminescence, and tip-enhanced Raman spectroscopy have been aligned for single nanowires. For the latter measurement, exclusively antimony related local vibrational modes have been identified in the sample in Raman spectroscopy.

The unintentional incorporation of carbon has been investigated and its impact on the optical performance of antimony doped nanowires. The effect of hydrogen co-doping drastically enhances the optical performance of these nanowires by reducing the concentration of non-radiative recombination centers and suppressing carbon-related emission lines. In intentionally related carbon-doped zinc oxide nanowires the appearance of four emission lines denoted as Z-lines at $3.3606\ \mathrm{eV}$, $3.3611\ \mathrm{eV}$, $3.3615\ \mathrm{eV}$, and $3.3618\ \mathrm{eV}$ have been analyzed and determined that these lines are as well carbon-related excitons bound to neutral donor states. With hydrogen co-doping, the optical performance was also enhanced.

The concept of exciton-polaritons is based on a coupling of light and exciton. In a m-plane ZnO layer, exciton-polaritons become visible in a backscattering geometry in photoluminescence and reflectance measurement. In both measurements additional waves identified as a Fabry-Pérot interference pattern are visible. The reflectance in the vicinity of the A and B-exciton has been modeled by a two-oscillator model. As a result, the detailed exciton-polariton dispersion curve of the upper, lower, and intermediate polariton branches was calculated. The revealed low damping of the A and B-exciton modes is crucial and the main cause why the Fabry-Pérot interference pattern occurs in the m-plane sample and was never reported in the literature for ZnO before.

Contents

1 Introduction

Our modern society has been significantly shaped by applications based on semiconductors so that it is still appropriate to describe the present as the age of semiconductors. From all devices in electronics, transistors are the most famous and still the backbone of modern chips in information technology. Semiconductors will also carry the next technological transformation from electronic devices to light-based photonic devices, where optoelectronic devices such as light-emitting diodes (LED) and laser diodes (LD) gain more importance. Zinc oxide (ZnO) is a wide band-gap direct semiconductor that has been studied for several decades. The main challenge for the commercialization of optoelectronic devices based on ZnO is the lack of stable and reproducible p-type doping. Many different elements have been studied for their capability to form shallow acceptor states to achieve p-type doping. Recently Antimony (Sb) gained much attention due to its theoretical capability to form a shallow acceptor as a complex impurity. Undesired impurities such as the incorporation of Carbon (C) can be unavoidable during the growth process but can also have a huge impact on the optical performance of the material. In addition, the material form can also improve performance. One dimensional nanowire can be grown on lattice-mismatched substrates with lower defect densities and therefore a higher crystalline quality due to the reduced influence of the substrate. All related material properties can be analyzed by the investigation of bound excitons in photoluminescence (PL) and reflectance spectroscopy. Since these methods are based on the interaction of the material with light, the concept of exciton-polaritons in the case of strong coupling between exciton and photon is also of importance.

1.1 Thesis structure

In the following, the general properties of the material ZnO are described in chapter 2 like its crystal structure together with some basic concepts like the definition of excitons and the concept of exciton-polaritons. In the following chapter 3, the used methodology is explained including a description of the used devices and setup for the analysis. Chapter 4 presents the investigation on the subject of Sb-doped ZnO nanowires indicate their properties and decide whether a donor or an acceptor is formed. The following chapter 5 focuses on the analysis of C-doped ZnO nanowires as well as C and Hydrogen (H) co-doped ZnO nanowires. In the last chapter 6, the

concept of exciton-polaritons is applied on a sample that show a distinct Fabry-Pérot interference pattern.

2 General properties of zinc oxide

Zinc oxide (ZnO) is a II-VI semiconductor and probably one of the best known representatives of the oxide materials besides magnesium oxide (MgO) and cadmium oxide (CdO). It predominantly crystallizes in a wurtzite structure and has a direct wide bandgap at the Γ-point of $3.37\ \mathrm{eV}\ (368\ \mathrm{nm})$ which corresponds to the ultraviolet band A (UVA) and a large exciton binding energy of $60\ \mathrm{meV}$. The ternary alloy system Zn(Mg,Cd)O covers the entire spectral range from UV to infrared (IR). This makes ZnO a competitor to gallium nitride (GaN) and its ternary alloy system with aluminum nitride (AlN) and indium nitride (InN).

Although the focus lies here on its application and properties as a semiconductor in optical and electrical devices it should be mentioned that ZnO has today a variety of different applications. For instance, ZnO is used as a pigment in cosmetics, as an additive in the production of rubber, a medical ointment, or UV absorber in sunscreens. This indicates that ZnO consists of inexpensive and non-toxic chemical components which makes the fabrication of ZnO devices even more advantageous.

There exist a variety of different growth techniques to gain ZnO as single crystals, thin films, or nanostructures. The most common method to form single crystals is the hydrothermal growth from the gas phase by oxidation of Zn-vapor. This can be archived in a chemical vapor transport (CVT) technique with a chamber reactor of different temperatures. On one side the temperature is high enough to form Zn-vapor from a Zn-source and then the vapor is transported to a colder side where it can oxidize and condense to form crystals. With this method also very large crystals can be fabricated which can even be processed further to substrates. There are also reports of unintentional growth of ZnO crystals in a zinc-smelter as a by-product of industrial zinc white production, where the Zn-vapor reacts with oxygen in a not completely sealed furnace forming large crystals of up to $2\ \mathrm{kg}$ with different colors and mostly fluorescent in UV-light [1]. Thin films or nanostructures can be grown i.e. by metalorganic vapor-phase epitaxy (MOVPE) and molecular beam epitaxy (MBE). Further general details on different growth methods can be found in Morkoç [2], Klingshirn [3], and Ramachandra [4].

The analyzed Sb-doped ZnO nanowires in chapter 4, the Sb and H co-doped nanowires in chapter 5.1 as well as the C and H co-doped nanowires in chapter 5.2 have been grown by MOCVD and the analyzed ZnO thin film in chapter 6 have been grown by MBE.

2.1 Crystal structure

Besides the fabrication of artificial crystals, ZnO occurs also as a natural mineral refereed to as zincite (see figure 2.1).

Minerals have been systematically analyzed and classified in the "*Strukturbericht*" in the years 1919-1949 by X-ray diffraction and many of the findings apply also to artificial crystals since the chemicals properties as the bond type or atomic radius of the components are the same [5].

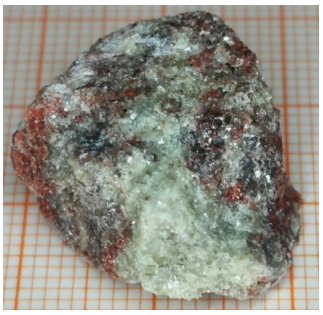

Fig. 2.1.: Natural zincite from a zinc mine in Gouverneur, New York, USA

In the methodology first described and published by W. Friedrich, P. Knippig and M. Laue in 1912 [6] X-rays are diffracted by a bulk crystal and the interference pattern is recorded on a film and hence named "*Lauephotogram*". Based on the famous equitation named after Bragg

$$2d \sin\theta = n\lambda \qquad \text{(Bragg)}$$

these patterns give insight into atom distances and symmetries of crystals. Max von Laue eventually was awarded the Nobel price in physics in 1914 [@7], William Lawrence Bragg and his father William Henry Bragg in 1915 [@8]. ZnO can have three different types of crystal structures which are denoted as B1, B3 and B4 according to the "*Strukturbericht*", where B is the designation for compound material of the form AB. Today, these crystal structures are more often named after a prominent representative of the group. B1 is a face-centered cubic lattice and is often referred to as rocksalt (or Rochelle salt) since sodium chloride (NaCl) has this form. B3 is also a face-centered cubic lattice and resembles the diamond form but with two different atoms. A prominent representative is Zinc sulfide (ZnS) or sphalerite which also is known as zincblende if crystallized in this particular α-phase. B4 is a hexagonal crystal structure often referred to as wurtzite, again named after ZnS but in its more

rare β-phase [9]. ZnO, however, crystallizes predominantly in the B4 hexagonal wurtzite form and all investigated samples in this work are also wurtzite ZnO.

To get crystallographic details for a material, crystal structures can be found in open-access databases [@10], such as this zincite information from Aminoff [11] on COD [@12]. From this, we can visualize the primitive unit cell (see figure 2.2a) the hexagon (see figure 2.2b) and the hexagon unit cell (see figure 2.2c).

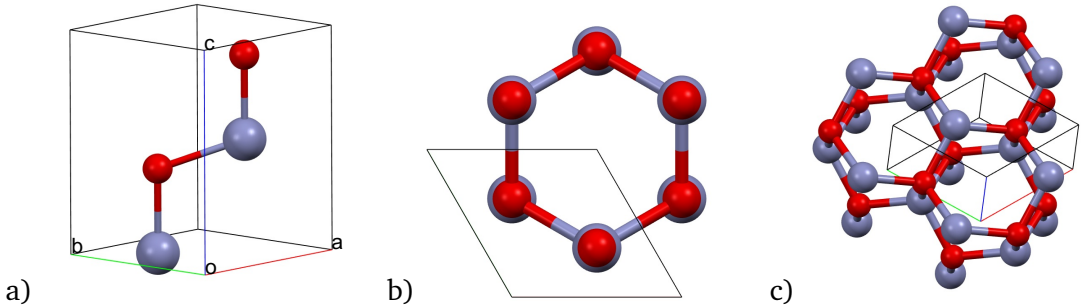

a) b) c)

Fig. 2.2.: a) Primitive unit cell of wurtzite ZnO as ball-stick-visualization (with Mercury 4.0 [13]). Zn-atoms are purple, O-atoms in red, with the axis a, b and c start from the origin o. b) Expanded crystal to visualize the hexagon shape (view from above compared to a)). c) Further expanded crystal. This is commonly referred as the hexagonal unit cell.

Besides the atomic components, the symmetries of the crystal structure play an important role regarding the properties. The symmetries are described by point and space groups. There are different types of notations of how to indicate these symmetries, like the Schönflies notation. The wurtzite structure has a 6-fold rotational symmetry with a vertical symmetry axis in the Schönflies notation described as C_{6v}. As figure 2.2 shows, this results in alternate hexagonal planes of Zn and O layers along the c-axis which is the cause for pyroelectricity in ZnO along the c-axis.

The unit cell in reciprocal space is called the first Brillouin zone and points of high symmetries are called critical points. The center of the Brillouin zone is referred to as the Γ-point.

2.2 Conduction and valence bands

The most prominent key figure of a semiconductor is most likely its bandgap which is the energetic offset between the conduction band minimum to the valence band maximum. Both the minimum of the conduction band as well as the maximum of the valence band are located at the Γ-point in ZnO making it a direct semiconductor.

The dispersion relation $E(\mathbf{k})$ of the bands also fulfill certain symmetries. The s-like conduction band results in a Γ_7 symmetry at the Γ-point, whereas the valence band is p-like resulting in a Γ_{15} symmetry. Due to crystal field and spin-orbit coupling, the valence band splits into three double degenerate bands with different energy levels, A, B, and C are labeled in descending energetic order. In wurtzite crystals two of these bands have Γ_7 and one has Γ_9 symmetry and the ordering of the bands depends on the crystal field and spin-orbit coupling. The ordering in ZnO was disputed for a long time and changed from its first investigation by Thomas and Hopfield in 1960 [14, 15] who concluded that the symmetry ordering is Γ_9, Γ_7, Γ_7 for the A, B, and C valence band respectively like in GaN and InN. Based on many different experiments it is commonly excepted today that the A and C valence band has Γ_7 and the B valence band has Γ_9 symmetry, hence a Γ_7, Γ_9, Γ_7 ordering [16, 17, 18] as for AlN. The symmetry of the bands at the Γ-point is important for the selection rules.

2.3 Excitons and exciton-polaritons

If an energy quantum is absorbed by the crystal and its energy exceeds the bandgap an electron can be excited from the valence band into the conduction band resulting also in a hole in the valence band. Since both particles have opposite charge they are attracted to each other by Coulomb force. If the group velocity of the electron equals the group velocity of the hole both can follow each other and bind. The group velocity is related to the band's curvature $\nabla_{\mathbf{k}}\epsilon_c = \nabla_{\mathbf{k}}\epsilon_v$ whereas the formation of excitons is possible at every critical point. The spontaneous recombination of an exciton results in the emission of a photon with an energy equal to the bandgap reduced by the binding energy of the exciton. The selection rules for the A, B, and C free exciton are summarized in table 2.1.

Tab. 2.1.: Selection rules for excitons in ZnO based on the symmetry of the conduction band Γ_c, valence band Γ_v and the envelope function Γ_{Env} for $n = 1$ states. The Number in brackets indicate degenerated states. States with a high oscillator strength are marked with an asterisk. [3, 19]

Exciton	Symmetry $\Gamma_{Env} \otimes \Gamma_c \otimes \Gamma_v$		allowed $E \parallel c$		allowed for $E \perp c$		Forbidden
A	$\Gamma_1(1) \otimes \Gamma_7(2) \otimes \Gamma_7(2)$	=	$\Gamma_1(1)$	$\oplus$	$\Gamma_5^*(2)$	$\oplus$	$\Gamma_2(1)$
B	$\Gamma_1(1) \otimes \Gamma_7(2) \otimes \Gamma_9(2)$	=		$\oplus$	$\Gamma_5^*(2)$	$\oplus$	$\Gamma_6(2)$
C	$\Gamma_1(1) \otimes \Gamma_7(2) \otimes \Gamma_7(2)$	=	$\Gamma_1^*(1)$	$\oplus$	$\Gamma_5(2)$	$\oplus$	$\Gamma_2(1)$

The absorbed energy quantum required to create an exciton in an optical experiment stem in most cases from an absorbed photon. It should be noted that an

exciton can also be created resonantly. In this case, the energy absorbed equals the photon emitted by the recombined exciton. Since an exciton can hence emit a photon which energy is sufficient to create another exciton in the crystal, both exciton and photon, cannot be described individually anymore and are referred to as an exciton-polariton. Individually, exciton and photon have different dispersion relations (see figure 2.3).

In the case of an exciton-polariton with a coupling between photon and exciton, both dispersion curves repel each other where they would normally cross. The result of this quantum-mechanical non-crossing rule is two new dispersion curves denoted as lower polariton branch (LPB) and upper polariton branch (UPB). In the vicinity of the frequencies of the longitudinal (ω_L) and transverse (ω_0 or ω_T) component of the electromagnetic wave, the two branches are commonly referred as exciton-like and in the opposite case photon-like. It can be derived that in ZnO only transverse exciton-polaritons (i.e. for $E \perp k$) exists and in the opposite longitudinal case (i.e. for $E \parallel k$) only longitudinal excitons [21]. For the intermediate case with an arbitrary angle between k and c so-called mixed-modes occur. The coupling between photon and exciton is reduced compared to the transverse case, which results in a decrease of the gap between the UPB and LPB.

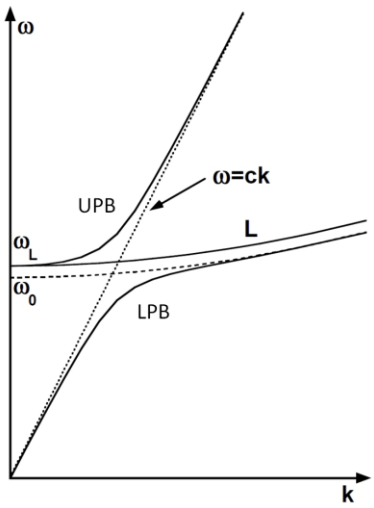

Fig. 2.3.: Exciton-polariton dispersion with the upper polariton branch (UPB) and lower polariton branch (LPB) with the frequency ω and wave-vector k. The dashed curves represent the dispersion relation of the uncoupled exciton and photon. [20]

2.4 Bulk, layers and nanowires

Besides the attributes determined by the semiconductor material itself also the dimensionality of the structure can have a huge impact on the resulting electrical, optical and vibronic properties. General statements regarding a semiconductor crystal are normally only applicable for a crystal that is in all three dimensions extended into infinity. In practice, this could be approximated with a large bulk crystal if the effects caused by its interfaces are negligible. If one dimension is further reduced in length this is often referred to as platelets. The samples investigated here

comparable to this dimensionality were grown epitaxial on a substrate and therefore referred to as layers. The main difference to platelets is the existence of an interface of the layer to the substrate or between different layers if there is more than one. These layers can have different properties especially if they are made out of different materials (heteroepitaxial) but even if these layers share the same semiconductor material (homoepitaxial) the resulting properties vary for each layer e.g. regarding strain or defect densities. If the one reduced dimensionality is reduced to an extent that confinement has to be regarded as well, this structure is commonly called a quantum well.

If we reduce the crystal in two dimensions the terms nanorods or nanowires are commonly used. There is no clear distinction between both terms so that they can be used as synonyms. However, as a rule of thumb nanorods are thicker in diameter and shorter than nanowires or in other words, have a smaller aspect ratio (length divided by width). Again, if we reduce both dimensions further so that confinement takes place, quantum wire is also commonly used. The investigated samples in Section 4 are nanowires. Due to the large surface-to-volume ratio, this structure can be beneficial for instance for better light extraction. Also, these wires have been grown epitaxially on a substrate. Compared to a layer the influence of the substrate can be reduced due to the smaller interface.

2.5 Doping

Besides its fundamental bandgap, another main property of a semiconductor is its ability to be doped with other elements with the goal to increase charge carriers and still maintain its crystal properties. To achieve n-type conductivity the doping adds free electrons while p-type conductivity can be achieved by adding holes. The ability to dope the material both ways is vital for most applications and therefore an important task in research. In wide bandgap materials such ZnO, ZnSe [22], and GaN [23] p-type conductivity was the main challenge to achieve for many decades. Both GaN and ZnO are normally intrinsic n-type which needs to be compensated first. Eventually, Mg turned out to be the dopant of choice in GaN and its efficiency has been improved always on. Due to its broad application in nowadays blue and white LEDs Isamu Akasaki, Hiroshi Amano, and Shuji Nakamura were awarded jointly the Nobel Prize in 2014 [@24]. More details can be found in the book "*The Blue Laser Diode*" [25].

Contrary to this, in ZnO p-type conductivity remains a challenge and could not be solved comparable to GaN. But unlike a race where the winner takes it all, it would still have a huge impact if this problem could be overcome in ZnO. Additionally doping whether by acceptors or donors can give further insight into the material properties itself. Intentionally undoped ZnO exhibits n-type conduction due to the intrinsic defects, such as zinc interstitials (Zn_i) [26], oxygen vacancies (V_O), as well as undesired hydrogen impurities during the growth process. A variety of different attempts have been made predominantly to substitute with an element of a lower group, for example, Zn with Cu[27], Ag [3], or Li [28], and O with N [29], P [30], As [31], and Sb [32]. In these cases, an acceptor would be formed if the dopant is incorporated on a lattice site substituting the desired element but a donor is formed if the dopant substitutes the undesired element or if the dopant is incorporated as an interstitial. From the already mentioned, N was the most promising candidate to achieve p-type conductivity since the atomic radii of O and N are quite similar. Calculations and experiments however revealed that the resulting acceptor is a deep state of approximately $1.3\ \mathrm{eV}$ [33, 34] which exceeds the thermal energy at room temperature of $26\ \mathrm{meV}$ by far.

Recently other doping structures have been proposed like F on an interstitial place [35] or a resulting complex structure based on doping with As or Sb [36]. Especially the latter method gained a lot of attention and in many publications, a p-type conductivity has been claimed but the results were also disputed [37, 38, 39, 40, 41]. In this proposed case based on first-principles calculations, Sb or As substitute Zn, which would result in a three-fold donor state but in addition two Zn vacancies form spontaneously where each can accept up to two electrons. This would lead to a residual shallow acceptor state. The calculated formation energies E_{Form} for different doping defects are summarized in table 2.2.

Tab. 2.2.: Formation energy E_{Form} of doping defects for Sb doping. [36]

Defect	Charge	E_{Form} (eV)
Sb_{Zn}	3+	-0.80
	+	0.74
$Sb_{Zn} - V_{Zn}$	+	1.08
	-	3.04
$Sb_{Zn} - 2V_{Zn}$	0	2.00
	-	2.16
	3-	5.33
Sb_O	0	11.20
	-	12.82

In chapter 4 and chapter 5.1 the Sb-doped samples are analyzed to determine which doping defect or complex is present and compared with typical dopants which yield a donor state such as gallium or indium.

3 Methodology

This section explains the analytical methods used in the experiments which generated the measurements discussed later. The focus is hereby not only on the description of the experimental setups but also on the introduction of its underlying physical principles.

3.1 Optical and electron microscopes

To determine the morphology of the samples a microscope (Olympus BX61) has been used with a variety of different objectives (5x - 100x) and magnifications. Macroscopic distortions and scratches from the dispersion of the samples can be seen easily but for single nanowires, the resolution necessary would be well below the Abbe-Limit:

$$d = \frac{\lambda}{2n \sin \alpha} = \frac{\lambda}{2\mathrm{NA}_{obj}} \qquad \text{(Abbe-Limit)}$$

To overcome this resolutions limit an electron microscope was utilized at the Otto-von-Guericke University in Magdeburg, Germany. Due to the small De-Broglie-wavelength for electrons a higher resolution is possible. For a higher contrast in the images, secondary electrons have been detected rather than the direct back-scattered electrons of the electron beam.

3.2 Photoluminescence spectroscopy

The analysis of the interaction of light with matter is one of the most used techniques to determine fundamental properties of semiconductors. In a first attempt to categorize the possible interactions it can be argued that light either can pass (transmission), vanish (absorption) or change its direction of propagation (reflection or scattering) and hence give insights into the refractive index of the material. In all these cases, however, light interacts with matter but does not change its color. In "On the Change of Refrangibility of Light" published in 1852 by G.G. Stokes[42] firstly an additional interaction named *dispersive reflexion* was described where the color (i.e. wavelength) of the light does not necessarily remain constant. In photoluminescence spectroscopy, the change in color of the light is the key process that

gives insights. The semiconductor gets excited by a laser normally with an energy above its band-gap and re-emits light after absorption, generally with a lower energy. The emitted light corresponds to the band-gap, free or bound exciton-recombination or other characteristic energy states.

In the standard photoluminescence setup, a helium-cadmium (HeCd) laser (Omnichrome 3074) has been used as excitation source with a laser wavelength of of $325\ \mathrm{nm}$ ($3.81\ \mathrm{eV}$) and excitation power of $5\ \mathrm{mW}$. The sample was placed in a continuous-flow microscopy cryostat (Janis ST-500) and cooled down with liquid helium to $5\ \mathrm{K}$. The laser was reflected via a small mirror into the beam path and focused via a UV-lens (suprasil glass)onto the sample. The re-emitted light collected by the same lens was then focused with a second lens to adjust the aperture into the entrance slit of the spectrometer. The spectrometer consist of a Czerny-Turner double-monochromator (SPEX 1404) with a focal length of $0.85\ \mathrm{m}$ and two gratings with $1.200\ \mathrm{l/mm}$ and a blaze of $500\ \mathrm{nm}$ as well as a UV-enhanced 330x1100 CCD (ST-138, Roper Scientific).

3.2.1 Micro-photoluminescence spectroscopy

In the micro-photoluminescence (μ-PL) setup the focusing lens is replaced by a 20x UV-microscope-objective (Thorlabs, LMUL-20X-UVB) mounted on a closed-loop 3D-Piezo actuator (PI, NanoCube P-611.3s) which allows lateral depending photoluminescence maps. Due to the objective, a smaller spot size and therefore a higher excitation density is possible. The collected light is again focused on a spectrometer to adjust to the correct aperture. In the μ-PL setup a single Czerny-Turner monochromator (SPEX 1704) with a focal length of $1\ \mathrm{m}$ has been used. The gratings are interchangeable and a $150\ \mathrm{l/mm}$ (blaze $300\ \mathrm{nm}$) has been used to obtain overview spectra, a $1.200\ \mathrm{l/mm}$ (blaze $300\ \mathrm{nm}$) for the regular spectra with highest light throughput and a $1.200\ \mathrm{l/mm}$ (blaze $500\ \mathrm{nm}$) used in 2. order for high resolution spectra. Again a UV-enhanced 550x2048 CCD (Princeton Instruments) has been used as a detector. Due to the small aperture of the objective a 30:70 UV beam-splitter is used to achieve a backscattering geometry instead of a small mirror.

3.2.2 Photoluminescence excitation spectroscopy

The setup used for photoluminescence excitation spectroscopy (PLE) is based on the standard PL setup described in 3.2, but instead of an excitation source with a fixed wavelength, a laser source with a tunable wavelength was used. For the PLE the HeCd-Laser was replaced by a dye laser (Lambda Physik FL 3002). The used dye DMQ (2-Methyl-5-t-butyl-p-quaterphenyl) (Lamdachrome, LC3590) was solved in

dioxane and has a wide laser range in the UV (346 nm-388 nm). The wavelength was tuned by an intra-cavity grating which acts as a dispersive mirror. The dye laser was pumped by a xenon monochloride (XeCl) excimer laser with a wavelength of 308 nm. The pulsed laser system had a pulse length of 20 ns and a tunable repetition rate of up to 100 Hz.

3.2.3 Zeeman spectroscopy

In atomic physics, discrete spectral lines can split up into different energy states indicating a fine structure under the influence of an external magnetic field. The degeneracy of the energy states is removed by the magnetic field. This so-called Zeeman-Effect was named after Pieter Zeeman who conjointly with Hendrik A. Lorentz received the Nobel prize in 1902 [@43] for this phenomenon. Analogous also energy states with a residual magnetic moment in semiconductors e.g. exciton states show a splitting under the influence of an external magnetic field. The splitting itself as well as the thermalization behavior of the split components can be observed in a static magnetic field and give insight into the origin of the energy states.

The used static magnetic field strength of up to 5 T is small compared to the binding energy of the free exciton so that only two major effects need to be considered, the described Zeemann splitting as well as the diamagnetic shift

$$\Delta E_{Dia} = \frac{1}{2} c^2 a_B^2 B^2 / \mu \tag{3.1}$$

where a_B is the exciton Bohr radius. The diamagnetic shift is negligible compared to the Zeeman splitting for low magnetic field strengths and small exciton radii like the $n = 1$ state of the free excitons. For higher exciton states the diamagnetic shift becomes more important to consider even for low static magnetic fields due to its quadratic dependency.

The Zeeman splitting of an exciton state under an external magnetic field $\mathbf{B}$ depends on the Bohr magneton μ_B as well as the g-factor (magnetic moment) $\mathbf{g}_{exc}$ of the exciton:

$$\Delta E_Z = \mathbf{g}_{exc} \mu_B \mathbf{B} \tag{3.2}$$

The exciton g-factor $\mathbf{g}_{exc}$ is depicted as a tensor here since its value in general depends on the orientation of the applied magnetic field vector with respect to the crystal. $\mathbf{g}_{exc}$ is the resulting magnetic moment of the electron and hole of the exciton and hence,

$$\mathbf{g}_{exc} = |\mathbf{g}_e \pm \mathbf{g}_h| \tag{3.3}$$

In wurtzite ZnO, the anisotropy of the g-factor of the electron and hole can be expressed with two components, one where the magnetic field vector is parallel to the crystals c-axis ($\mathbf{B} \parallel \mathbf{c}$) denoted with $g^{\parallel}$ and one where the magnetic field vector is perpendicular to the crystals c-axis ($\mathbf{B} \perp \mathbf{c}$) denoted with $g^{\perp}$. For an arbitrary angle θ between the magnetic field and the c-axis the g-factor is then

$$g = \sqrt{\left|g^{\parallel}\right|^2 \cos^2\theta + \left|g^{\perp}\right|^2 \sin^2\theta} \tag{3.4}$$

The anisotropy of the electrons g-factor is very small compared to the g-factor of the hole and typically cannot be resolved in PL measurements here but in electron paramagnetic resonance (EPR) [44, 45] or optically detected electron-paramagnetic-resonance (ODMR) spectra [46] and therefore it can be simplified with

$$g_e^{\parallel} = g_e^{\perp} = g_e \tag{3.5}$$

and equation 3.4 is hence only used for the holes g-factor g_h.

The Zeeman splitting of an exciton depends strongly on the circumstance whether the exciton is free, bound to a neutral or ionized donor or acceptor or to an other type of defect. In the case of a neutral-bound exciton one of the particles, electron or hole of the exciton, is involved in the binding to the dopant, where the other unpaired particle determines the splitting behavior. In the case of a free or ionized bound exciton both particles are unpaired. In the following the behavior of these two cases is described in more detail.

Exciton bound to neutral donors or acceptors

A donor has a weakly bound electron and a positively charged atomic core, whereas an acceptor has a weakly bound hole and a negatively charged atomic core. This is the ground state of a neutral-bound exciton transition. In the excited state, an exciton is bound to the neutral impurity due to the formation of pairs with anti-parallel spin of the two like particles. This leaves an unpaired particle in the exciton.

Figure 3.1 illustrates the expected transitions in the two geometric cases with respect to the normal PL ($\mathbf{B} = 0$) transition ($\mathbf{E}_0$) for acceptors and donors respectively. In the Faraday configuration, the magnetic field is purely parallel to the c-axis of the crystal ($\mathbf{B} \parallel c$). In the opposite case, in the Voigt configuration, the magnetic field is purely perpendicular to the c-axis ($\mathbf{B} \perp c$). The ground state for a donor is determined by the unpaired electron with its nearly isotropic g-factor g_e, hence an identical splitting for both geometric cases, Voigt and Faraday. In the

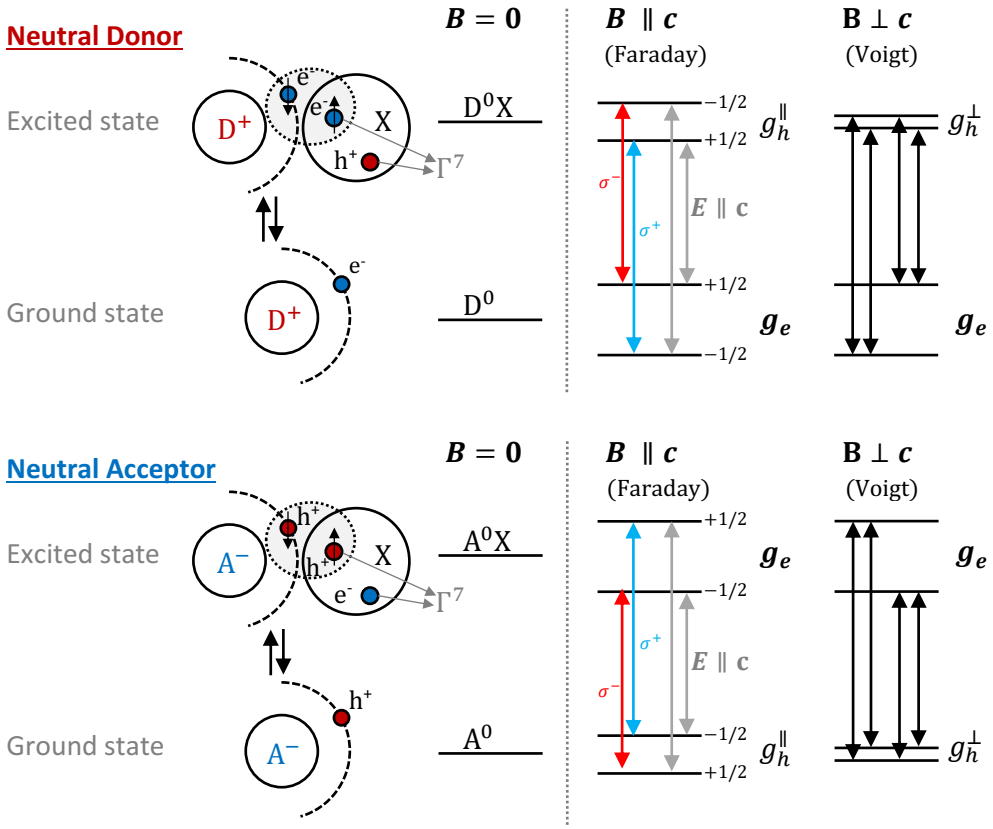

Fig. 3.1.: Zeeman splitting of neutral-bound exciton complexes involving Γ^7 electron states and Γ^7 hole states of the exciton (A-exciton) in a constant external magnetic field with $\mathbf{B} \parallel \mathbf{c}$ (Faraday-configuration) and $\mathbf{B} \perp \mathbf{c}$ (Voigt-configuration). The g-values of the ground and excited states depend on the spin of the unpaired particles. Circular polarized transitions are indicated by blue (σ^+) and red (σ^-) lines.

excited state the excitons electron pairs with the donor's electron and the splitting is hence determined by the unpaired hole of the exciton. Due to the anisotropy of the holes g-factor the splitting differs in both geometric cases. For an acceptor the splitting is mirrored since the ground state is determined by an unpaired hole of the acceptor and the excited stated by an unpaired electron left in the exciton.

The bound exciton in figure 3.1 is assumed to be an A-exciton since the measured PL transitions in the following chapters exclusively involve A-excitons. Based on the valence band ordering of Γ^7, Γ^9, Γ^7 of the A, B, and C valence bands, both the electron and hole of the A-exciton have a Γ^7-symmetry. Considering group theory [17, 18] four transitions are visible in the Voigt configuration with an overall smaller splitting due to

$$g_e > g_h^{\parallel} > g_h^{\perp}. \tag{3.6}$$

In the Faraday configuration, two of the four transitions are only visible if $E \parallel c$ and therefore not visible in the used backscattering geometry. The remaining two transitions are circularity polarized with σ^+ for the energetically higher and σ^- for the lower transition. All four transitions become visible if the sample is tilted with an arbitrary angle between the Faraday and Voigt configuration. The fourfold energy splitting in all geometries is determined by the prior derived g-factors:

$$\begin{aligned} E^{\pm} &= E_0 \pm \frac{1}{2}\mu_B(g_e \pm g_h)B \\ &= E_0 \pm \frac{1}{2}\mu_B \left(g_e \pm \sqrt{|g_h^{\parallel}|^2 \cos^2\theta + |g_h^{\perp}|^2 \sin^2\theta} \right) B \end{aligned} \tag{3.7}$$

whereby $\theta = 0$ corresponds to the pure Faraday and $\theta = 90°$ to the Voigt configuration.

Since the energetic splitting is mirrored for donors and acceptors a direct distinction based on their spectral position is not possible. Nonetheless, a distinction can be made based on the thermalization behavior. The largest splitting occurs in the Voigt configuration since the largest and smallest g-factor is involved. The large splitting based on the electrons g-factor occurs for a donor in the ground state and an acceptor in the excited state. While the thermalization behavior in absorption is caused by the ground state, the thermalization behavior is caused by the excited state in PL [17, 18]. Hence both main components of an acceptor bound exciton transition should have the same thermalization behavior (intensity with increasing temperature) in absorption but different in PL resulting in a changing intensity ratio of the two components. In the case of a donor-bound exciton transition, both components should have a changing intensity ratio in absorption but identical (no change of the intensity ratio) for PL. Therefore temperature-dependent PL with a high magnetic field in the Voigt configuration can be used to identify whether an impurity acts as a donor or as an acceptor.

Free excitons and excitons bound to ionized donors or acceptors

Free excitons and excitons bound to an ionized donor or acceptor have similar properties regarding the splitting behavior in PL under the influence of an external magnetic field. Similar to the prior chapter the energy splitting is illustrated in figure 3.2. Based on group theory the free A-Exciton (see table 2.1) consists of a Γ^5, Γ^2 and Γ^1 state, where only the Γ^5-state (allowed for $E \perp c$) is normally visible for c-plane samples in a back-scattering PL. The Γ^1 is weakly allowed with $E \parallel c$ and the Γ^2 transition is forbidden. The symmetries of the energetic states are the same in the case of a weakly bound exciton to an ionized impurity since the particles do

not pair with opposing spins. The ground state represents the recombination of the electron-hole-pair with Γ^1-symmetry.

In the case of an external magnetic field, the excited states split only in the Faraday configuration. The Γ^5-state splits into two circular polarized states for $E \perp c$ and remains the only transitions visible in a normal backscattering PL for c-plane samples. In the Voigt-configuration no splitting occurs but both transitions become visible for both polarities $E \perp c$ and $E \parallel c$. This appearance of an additional line under an external magnetic field rather than a splitting is hence a clear indicator for an exciton bound to an ionized donor or acceptor.

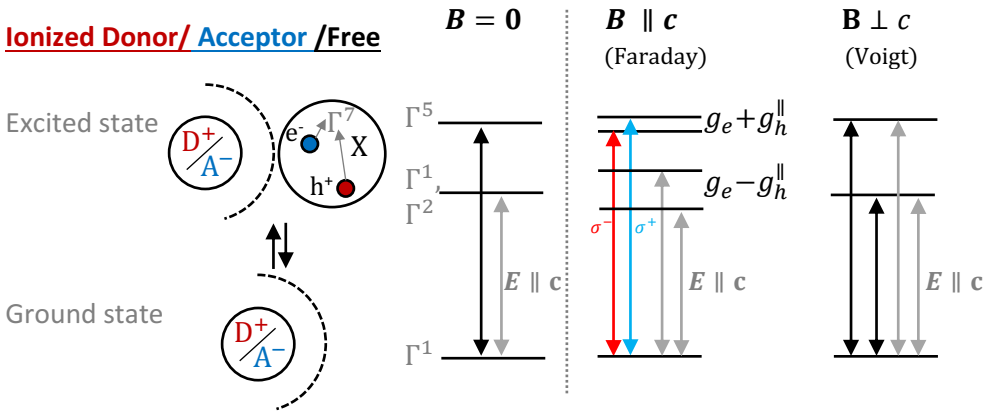

Fig. 3.2.: Zeeman splitting of ionized bound exciton complexes involving Γ^7 electron states and Γ^7 hole states of the exciton (A-exciton) in a constant external magnetic field with $\mathbf{B} \parallel \mathbf{c}$ (Faraday-configuration) and $\mathbf{B} \perp \mathbf{c}$ (Voigt-configuration). Circular polarized transitions are indicated by blue (σ^+) and red (σ^-) lines.

Used measurement setup

The measurement setup was almost identical to the PL setup (see chapter 3.2), hence a macro-PL setup with a helium-cadmium-Laser as the excitation source. The main difference was that the sample was mounted in an Oxford bath cryostat with liquid helium cooled superconducting niobium split coils. The coils can induce a magnetic field up to 7 T but to avoid a quench of the cryostat a maximum magnetic field of 5 T was used. The sample was located in the middle of the cryostat on a turnable sample holder and was submerged into superfluid helium for the low temperature (less than 2 K) measurements. For temperature-dependent measurements the sample was gradually cooled down with cold helium gas. For the angle-dependent measurement an optical rotary encoder was placed on the sample holder to determine the angle. The sample could then be rotated in the magnetic field. To achieve the two main configurations, Faraday and Voigt, the cryostat was rotated as a whole and the

rest of the setup remained unchanged. To differentiate different polarizations a $\lambda/4$-plate for the UV range from B-Halle was used to convert circular polarized into linear polarized light. A linear polarizer was then used as an analyzer in front of the entrance slit of the spectrometer to filter a specific polarization. To avoid any contributions of the subsequent optics, i.e. the grating, the analyzer was fixed and the $\lambda/4$-plate was rotated to change the polarization.

3.2.4 Reflectance

The reflectance was measured as an ideal additional method within the micro-PL setup. Instead of an excitation laser, a commercially available InGaN LED with a peak luminescence at around $365\ \mathrm{nm}$ and a half-width of $9\ \mathrm{nm}$ was used. The UV-LED (Nichia NVSU233A) had a power consumption of $1030\ \mathrm{mW}$. The reflected light was analyzed with the same components as the micro-PL setup. The resulting reflection spectrum of the the sample can give a more direct insight rather than PL that involves the absorption of the excitation laser and radiative and non-radiative decays. In addition, also selection rules are different for both methods.

3.3 Raman spectroscopy

The inelastic scattering of photons (typically in the visible range) with matter is called Raman-scattering or Raman-effect, where the residual energy of this process either increases or decreases the vibronic state of the system. Under the irradiation of monochromatic light, a liquid, gas or solid the scattering does not only consist of photons of the same energy and therefore wavelength but also with a part with lower energy (higher wavelength) referred as Stokes shift as well as a part with higher energy (lower wavelength) referred as Anti-Stokes shift. In contrast, the elastic scattering which is mostly several magnitudes of order higher in intensity is referred to as Rayleigh-scattering. In the case of solid-state materials such as semiconductor crystals, the attributed quasiparticle to these collective vibrations is called a phonon. While Raman-scattering in solid states involves optical phonons, the analog process regarding acoustic phonons is called Brillouin scattering. The considered Raman-effect in the later experiments involves mainly only one phonon, hence referred to as first-order Raman [47, 48]. The used laser had an energy below the bandgap to avoid luminescence.

At the beginning of the 20th century, theoretical physicists attempted to describe optical phenomena with Einstein's quantum theory of light. In 1922 Austrian physicist Adolf Smekal proposed a model to describe the dispersion of light consistent

with the new quantum theory [49] as a response to an unsuccessful attempt of one of his English colleagues and grandson of Charles Darwin, Charles Galton Darwin [50]. In his work, he expects that monochromatic light would also consist of wavelengths with higher and lower energy after scattering with the occurrence of "*'Translationsquantenübergangen*"' (translation quantum transitions). Today this work is often considered as the prediction of Raman-scattering.
The Indian physicists C.V. Raman and K.S. Krishnan discovered "*A New Type of Secondary Radiation*"' in an attempt to find an analog effect to the Compton-effect (X-ray scattering with electrons) for the visible photon range. They used a telescope with a blue-violet filter, the sun as light source and a yellow filter to attenuate the elastic Rayleigh-scattering to systematically analyze sixty different common liquids and their dust-free vapors. The letter where they report their findings was published in *nature* in March 1928 [51]. Notably, this letter did not contain any spectrum. Only two years later C.V. Raman was awarded the Nobel Prize in Physics [@52].
In the same year when C.V. Raman published his letter also two soviet physicists Gr. Landsberg and L. Mandelstam published their results about the inelastic scattering of photons in crystals (quartz and calcite) using a mercury lamp as light source [53]. This paper was received in July 1928, only four months after Raman. To honor this contribution the scattering process is sometimes also referred to as Raman-Landsberg-Mandelstam-scattering. A more detailed summary of the history and its controversy can be found elsewhere [54].

3.3.1 Macroscopic derivation of the Raman-effect

In the following the macroscopic derivation of the Raman-effect is presented to give a brief introduction and can be found in full length elsewhere [55].

If we consider an incident light beam with its electric field $\mathbf{E}$

$$\mathbf{E}(\mathbf{r},t) = \mathbf{E}_i(\mathbf{r}_i,\omega_i)\cos(\mathbf{k}_i\cdot\mathbf{r}-\omega_i t) \tag{3.8}$$

inducing a corresponding polarization $\mathbf{P}$ in the medium.

$$\mathbf{P}(\mathbf{r},t) = \mathbf{P}(\mathbf{r}_i,\omega_i)\cos(\mathbf{k}_i\cdot\mathbf{r}-\omega_i t) \tag{3.9}$$

Polarization $\mathbf{P}$ and the electric Field $\mathbf{E}$ are connected by the susceptibility $= \boldsymbol{\chi}$

$$\mathbf{P}(\mathbf{r}_i,\omega_i) = \boldsymbol{\chi}(\mathbf{k}_i,\omega_i)\mathbf{E}_i(\mathbf{k}_i,\omega_i) \tag{3.10}$$

so that the induced Polarization $\mathbf{P}$ can be expressed by

$$\mathbf{P}(\mathbf{r},t) = \boldsymbol{\chi}(\mathbf{k}_i,\omega_i)\mathbf{E}_i(\mathbf{k}_i,\omega_i)\cos(\mathbf{k}_i\cdot\mathbf{r}-\omega_i t) \tag{3.11}$$

the collective lattice vibrations, the phonons, can be expressed as displacements with generalized coordinates

$$\mathbf{Q}(\mathbf{r},t) = \mathbf{Q}(\mathbf{q},\omega_P)\cos(\mathbf{q}\cdot\mathbf{r}-\omega_P t) \tag{3.12}$$

so that also the susceptibility $= \boldsymbol{\chi}$ can be expressed and be developed into a Taylor series

$$\boldsymbol{\chi}(\mathbf{k}_i,\omega_i,\mathbf{Q}) = \boldsymbol{\chi}_0(\mathbf{k}_i,\omega_i) + \left(\frac{\partial\boldsymbol{\chi}}{\partial\mathbf{Q}}\right)_0\mathbf{Q}(\mathbf{r},t) + \cdots \tag{3.13}$$

Equation 3.13 insert in equation 3.11 with restriction to the first two term expresses the two different scattering processes (elastic and inelastic) mentioned above. The 0. order represents the Rayleigh-scattering:

$$\mathbf{P}_0(\mathbf{r},t) = \boldsymbol{\chi}_0(\mathbf{k}_i,\omega_i)\mathbf{E}_i(\mathbf{k}_i,\omega_i)\cos(\mathbf{k}_i\cdot\mathbf{r}-\omega_i t) \tag{3.14}$$

The 1. order represents the Raman-scattering

$$\mathbf{P}_{ind}(\mathbf{r},t,\mathbf{Q}) = \left(\frac{\partial\boldsymbol{\chi}}{\partial\mathbf{Q}}\right)_0\mathbf{Q}(\mathbf{q},\omega_P)\cos(\mathbf{q}\cdot\mathbf{r}-\omega_P t)\cdot\mathbf{E}_i(\mathbf{k}_i,\omega_i)\cos(\mathbf{k}_i\cdot\mathbf{r}-\omega_i t)-\omega_i t) \tag{3.15}$$

The last equation 3.15 can be rearranged to emphasize the two components:

$$= \frac{1}{2}\left(\frac{\partial\boldsymbol{\chi}}{\partial\mathbf{Q}}\right)_0\mathbf{Q}(\mathbf{q},\omega_P)\cdot\mathbf{E}_i(\mathbf{k}_i,\omega_i)\cdot(\cos\left[(\mathbf{k}_i+\mathbf{q})\cdot\mathbf{r}-(\omega_i+\omega_P)t)\right]+ \quad \text{(Stokes)}$$

$$\cos\left[(\mathbf{k}_i-\mathbf{q})\cdot\mathbf{r}-(\omega_i-\omega_P)t)\right]) \quad \text{(Anti-Stokes)} \tag{3.16}$$

A necessary condition that equation 3.15 does not vanish is that the susceptibility $\boldsymbol{\chi}$ changes with respect to the generalized coordinates, or in other words the Raman-tensor

$$\mathbf{R}_{ijm} = \left(\frac{\partial\boldsymbol{\chi}_{ij}}{\partial\mathbf{Q}_m}\right) \quad \text{(Raman-Tensor)}$$

is unequal to zero.

3.3.2 Microscopic derivation of the Raman-effect

The derivation can also be done with the use of quantum mechanics and perturbation theory as a microscopic theory. The lengthy derivation can be found again

elsewhere [55]. However, since this derivation focuses on the involved quasiparticles it will be outlined briefly in the following.

We can simplify that the incident light from equation 3.8 is monochromatic hence all photons have the same discrete energy. The Raman-scattering process can be described by three steps. First, the photon is absorbed by the medium and creates an electron-hole pair. Second, the electron-hole pair is scattered and emits (create) a phonon (Stokes case) or absorbs (annihilates) a phonon (Anti-Stokes case) and hence changes its energy. Third, the electron-hole-pair recombines and emits a photon with a different energy as the absorbed one. Figure 3.3 shows a sketch for the Stokes and Anti-Stokes case. Solid lines represent real electronic states (i.e. minimum and maximum of the conduction and valence band respectively) and dashed lines virtual states. Normally the involved intermediate states are virtual states but could also be real states (i.e. defect states). In the latter case, the Intensity of the Raman-scattered light is increased due to higher probabilities for the involved transitions and is used for resonant-Raman spectroscopy [56].

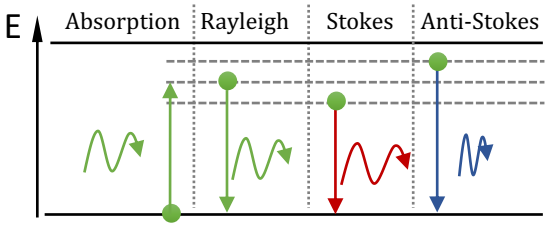

Fig. 3.3.: Rayleigh, Stokes, and Anti-Stokes processes of Raman-scattering.

3.3.3 Raman modes in ZnO

In a classical approach, a crystal can be modeled with point masses (atoms) with interconnecting springs between the masses (binding). If the unit cell contains only one atom, transverse and longitudinal acoustic vibrational modes can occur. If the unit cell contains 2 atoms additional modes are possible where the 2 atoms move in the opposite direction resulting in transverse and longitudinal optical vibrational modes. In general, in crystals with n atoms in the unit cell 3 acoustic modes and 3(n-1) optical modes occur. Since the unit cell of ZnO contains four atoms, its spectrum is characterized by twelve vibrational modes: three acoustic phonon modes(two transverse and one longitudinal) and nine optical phonon modes. For first-order Raman spectroscopy, only the phonons in the center of the Brillouin zone at the Γ-point are relevant. The optical modes are commonly denoted with their Mullikan-symbol

$$\Gamma_{opt} = A_1 \oplus 2B_1 \oplus E_1 \oplus 2E_2 \tag{3.17}$$

where A-modes are symmetric vibrations along with the c-axis B-modes are asymmetric vibrations along the c-axis E-modes vibrations perpendicular to the c-axis and twofold degeneracy. The A_1 and $E1$ modes are both Raman and infrared-active, the $E2$ is only Raman active and the B_1-modes are silent. [57]. The corresponding Raman-Tensors for wurtzite material are: [56]

$$E_2^{(1)}(x = \begin{pmatrix} d & 0 & 0 \\ 0 & -d & 0 \\ 0 & 0 & 0 \end{pmatrix}, E_2^{(2)} = \begin{pmatrix} 0 & d & 0 \\ d & 0 & 0 \\ 0 & 0 & 0 \end{pmatrix}, E_1(x) = \begin{pmatrix} 0 & 0 & c \\ 0 & 0 & 0 \\ c & 0 & 0 \end{pmatrix},$$
$$E_1(y) = \begin{pmatrix} 0 & 0 & 0 \\ 0 & 0 & c \\ 0 & c & 0 \end{pmatrix}, A_1(z) = \begin{pmatrix} a & 0 & 0 \\ 0 & a & 0 \\ 0 & 0 & b \end{pmatrix}.$$

In wurtzite ZnO, the A_1 and $E1$ modes split at the Γ-point into transverse (TO) and longitudinal (LO) modes due to the macroscopic crystal field caused by the anisotropy of the ZnO crystal. [58]. The non-polar E_2-modes have two frequencies denoted as E_2^{high} (high frequency) and E_2^{low} (low frequency). The $E_2^{low}$is associated with the vibrations of the Zn sublattice, while the E_2^{high} is related to the vibrations of the O-ions [56].

The scattering intensity of the Raman modes depend on the geometric orientation with

$$I_s = |\mathbf{e}_i \cdot \mathbf{R} \cdot \mathbf{e}_s|^2 \tag{3.18}$$

were $\mathbf{e}_i$ and $\mathbf{e}_s$ are the polarization vectors of the incident and scattered light respectively, and $\mathbf{R}$ the Raman tensor. The orientation of the incidents of the light (x_i) and its polarization (p_i), as well as the orientation of the scattered light (x_s) and its polarization (p_s) is commonly summarized in the Porto notation:

$$x_i(p_i, p_s)x_s \tag{3.19}$$

Table 3.1 shows the active (A) Raman modes for different orientations, as well as their expected position in a Raman spectrum.

3.3.4 Used measurement setup

The Raman setup consists of an Horiba HR800 LabRAM spectrometer, based on a $800\ \mathrm{mm}$ focal length Czerny-Turner-monochromator and a 1024x256 pixel Synapse CCD. The spectrometer was equipped with different gratings which could be selected for the measurement. For larger spectral distances a $600\ \mathrm{l/mm}$ was used while a $1800\ \mathrm{l/mm}$ grating was used for spectra with higher resolution. As excitation source

Tab. 3.1.: Expected Raman-modes for wurtzite ZnO for different orientations. A stands for active.

Mode	Pos. [59] (cm^{-1})	$z(x,x)\bar{z}$ $z(y,y)\bar{z}$	$z(x,y)\bar{z}$	$x(y,y)\bar{x}$ $y(x,x)\bar{y}$	$x(z,z)\bar{x}$ $y(z,z)\bar{y}$	$x(y,z)\bar{x}$	$x(z,y)\bar{y}$
$A_1(TO)$	378			A	A		
$A_1(LO)$	574	A					
B_1^{low}	silent						
B_1^{high}	silent						
$E_1(TO)$	410					A	A
$E_1(LO)$	590						A
E_2^{low}	99	A	A	A			
E_2^{high}	438	A	A	A			

a helium-neon-laser (HeNe) was used with a wavelength of $632.8\ \mathrm{nm}$ $(1.96\ \mathrm{eV})$. To attenuate the much higher Rayleigh scattering a notch filter for the specific wavelength of the laser has been used which simultaneously acts as a beamsplitter in the setup. The laser from the excitation path is reflected by the notch filter and focused on the sample. The Raman signal with a different wavelength can pass the filter into the detection path of the spectrometer. An Olympus 100X MPlan objective, with a numerical aperture of $NA = 0.9$, was used to focus the laser on the sample and collect the scattered light.

3.3.5 Tip-enhanced Raman spectroscopy

Since Raman spectroscopy uses light for detection, the lateral resolution is also limited by the Abbe-limit like in a normal optical microscope. In tip-enhanced Raman spectroscopy (TERS) the Raman signal gets enhanced in the presents of a metallic atomic force microscope (AFM) cantilever resulting in a localized origin of the signal with respect to the apex of the cantilever. The resolution of the lateral information can therefore be increased by a smaller diameter of the apex reducing the contact between the cantilever and the sample and therefore also exceed the Abbe-limit. The interaction of the cantilever and the sample is related to a different effect. In 1974 researchers reported an anomalously strong Raman scattering from pyridine adsorbed on silver electrodes [60] and later interpreted as surface-enhanced Raman scattering (SERS) [61] likely due to the excitation localized surface plasmons on the metallic surface. TERS utilizes this SERS-enhancement of a metallic surface by the AFM cantilever. The exact mechanism behind the SERS as well as TERS enhancement is still under debate and there are already numerous effects identified

which contribute to the enhancement individually and combined. [62, 63]

For the measurements, a coupled system consisting of a Horiba Hr800, as used for the standard Raman measurements, and a Park XE 100 AFM was used. Both parts were connected by a tubed beam path and the laser could be flipped by a flip mirror. Again, the excitation source was the $632.8\ \mathrm{nm}$ ($1.96\ \mathrm{eV}$) laser line of a HeNe. The sample was placed into the AFM and the custom-made gold cantilever approached the surface by a piezo-stage. The laser was then focused with an Olympus SLMPLN 50X long distance ($18\ \mathrm{mm}$) objective with a numerical aperture of $NA = 0.35$ at an incident angle of $60°$ with respect to the surface normal vector of the sample. The alignment was done by a piezo stage moving the objective. Once the alignment was done the relative position of the laser spot and the cantilever tip was locked. To spatially scan the sample a third piezo stage was used. The Raman scattered light was collected via the same objective and transferred to the Raman spectrometer. The AFM was operated in tipping-mode during the measurement. The gold cantilever with an apex of typically $15\ \mathrm{nm}$ had also a flat angle of incidence with respect to the sample surface resulting in an elliptical shape contact. However, in the setup a spatial resolution of $35\ \mathrm{nm}$ was achieved. [64]

3.4 Calibration and data processing

All photoluminescence and reflectance spectra have been recorded in wavelength, calibrated and converted into energy. The calibration was done by recording a reference spectrum of a mercury calibration lamp (Quantum Design - pen-ray LSP035). The Raman spectra were calibrated by a custom-made neon lamp. The energy conversion was then calculated by

$$E = \frac{hc}{n\lambda_{Air}} \tag{3.20}$$

with Planck's constant h, the speed of light in vacuum c and the refractive index of air n. To consider the wavelength dependency of n the values obtained by Ciddor [65] for standard air were used.

The used CCD detectors have a limited range of counts resulting in an overflow of the spectrum if the integration time is too long. However, if the integration time is restricted to prevent such an overflow for the maximum peak, the shorter integration time limits the signal-to-noise ratio of the smaller peaks in the spectrum. To enhance the dynamic of the detector, several spectra were recorded and then combined. In figure 3.4 the single spectra for different integration times are plotted. Only the spectrum with the lowest integration time of $0.01\ \mathrm{s}$ contains the peaks

with the highest intensity and for the smallest features a poor signal-to-noise ratio is visible. For the higher integration times an overflow with a flat horizontal line is visible. The small features have the best signal-to-noise ratio in the spectrum with the longest integration time of 10 s. The spectra with the different integration times have been adjusted in heights and combined to an spectrum with a high dynamic range (HDR). Different spectra with an intensity scale of arbitrary units in a single graph are shifted for clarity.

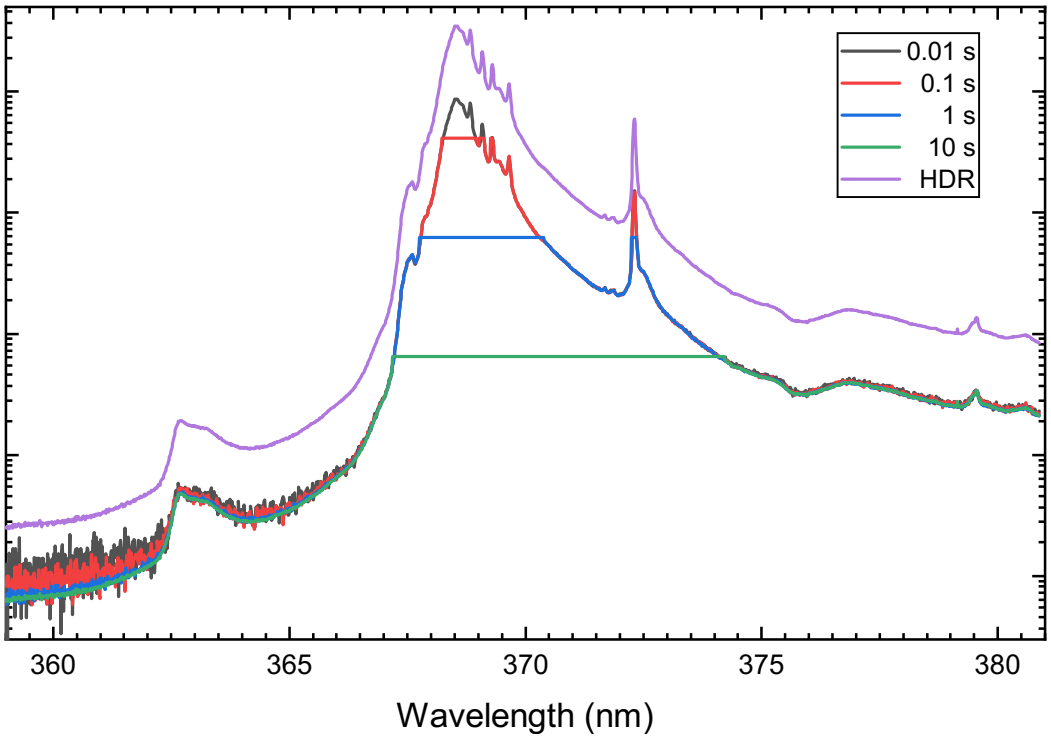

Fig. 3.4.: Photoluminescence spectra for the same sample at different integration times. The resulting merged high dynamic range (HDR) spectrum is shifted for clarity.

4 Antimony doped zinc oxide nanowires

This chapter focuses on the analysis of Antimony (Sb) doped Zinc Oxide (ZnO) nanowires (NW). As described in Chapter 2 the potential of ZnO as a semiconductor with a large bandgap for optoelectronic applications is hindered by its challenges to achieve sufficient p-type doping. As described further, Sb could be a promising candidate to master this challenge and gained therefore much attention recently. The overall assessment of whether Sb acts like an acceptor and p-type conductivity is feasible is however still controversial.

In order to increase clarity to this subject, a consistent sample series with different doping concentrations of Sb has been grown and analyzed. The growth process and the sample series will be described in the following section 4.1. The analyzing methods and setups described in chapter 3 have been used to find answers to the still open questions: Does antimony incorporate into the ZnO crystal and what are the optical traces of this doping? What are the properties of the doping states? Does Sb act as a donor or as an acceptor? For a satisfying answer, photoluminescence measurements are necessary, in particular under the influence of an external magnetic field. In what form does Sb incorporate into the lattice? Are there lateral differences within a single nanowire? For high lateral resolution micro-PL (μ-PL), cathodoluminescence with a standard electron microscope (CL) as well as with a scanning transmission electron microscope (STEM-CL) have been used. All questions regarding the lattice have a direct impact on the phonons in the material and can therefore be investigated with Raman spectroscopy, in particular impurity sensitive local vibrational modes. To lateral differentiate within a single nanowire tip-enhanced Raman spectroscopy (TERS) was used.

4.1 Growth

The analyzed samples have been grown by metalorganic vapor-phase epitaxy (MOVPE) at the Simon-Frazer University in Vancouver, Canada within the research group of Prof. Simon Watkins.

For this growth technique, a substrate is needed to be stored and heated in a growth chamber also referred to as the reactor. The deposition of the desired

material at the surface of this substrate is a result of a chemical reaction of different vapors in the chamber. Therefore, this growth technique belongs also to the category of metalorganic chemical vapor deposition (MOCVD) just with the particularity of an epitaxial deposition (growth layer-by-layer). The reagents, i.e. oxygen and zinc have to be present as vapors in the chamber. The source for the metal is normally stored in a stainless steel canister (bubbler) containing a liquid metalorganic compound (precursor). The reagents are transported with the use of a carrier gas which is passed through the bubbler until the gas is saturated with the precursor material and then directed into the chamber. The source for the reactive nonmetal, i.e. oxygen, in this case, is a suitable gas that can directly be passed into the chamber. Both gases react at the surface of the substrate and a crystal appears to grow under certain ambient conditions. Undecomposed precursors and byproducts of the growth reaction can leave the chamber via an exhaust at the end.

For the heteroepitaxial growth of the analyzed samples prior annealed epi-ready c-sapphire (Al_2O_3) substrates heated to a temperature of $600\ °C$ have been used in a horizontal reactor with an ambient pressure of $700\ \mathrm{Torr}$. dimethylzinc (DMZn - $(CH_3)_2Zn$) and trimethylantimony (TMSb - $(CH_3)_3Sb$) have been used as zinc and antimony sources respectively and nitrogen (N_2) as carrier gas. The Sb-doping concentration was controlled by the gas flow rate of the saturated mixed gas of the bubblers. Gaseous nitrogen dioxide (NO_2) on the other hand has been used as a source for oxygen. Under these conditions, ZnO nanowires grow spontaneously on the surface of the sapphire substrate. The investigated sample series consists of 7 different samples with one intentionally undoped control sample.

Measurements on the as-grown samples are referred to as *ensemble* measurements since a variety of different nanowires contribute to the detected signal depending on the laser spot size. To be able to measure a subensemble of nanowires down to even a single nanowire some of the nanowires have been scratched off of the original sample with a scalpel and dispersed to a new sapphire or silicon dioxide (SiO_2) substrate.

4.2 Morphology of antimony doped nanowires

Bulk ZnO with high crystalline quality and low defect density has low absorption in the visible range and is therefore transparent for the human eye. With the increase of defects in the crystal, the appearance changes often to a transparent crystal with a light yellowish color. Here, the analyzed samples appeared to be opaque white with no tint of color (see fig. 4.1 a). The scratched areas where nanowires have been removed, however, can be seen clearly on the surface. Under the microscope

(fig. 4.1 b) with Nomarski contrast single nanowires are visible in the proximity of the scratched surface as well as single dispersed nanowires on a (SiO_2) substrate with a hole grid (fig. 4.1 c).

a) 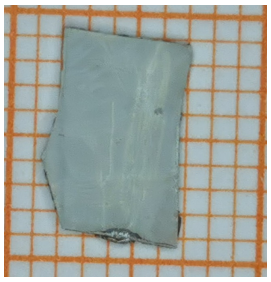 b) 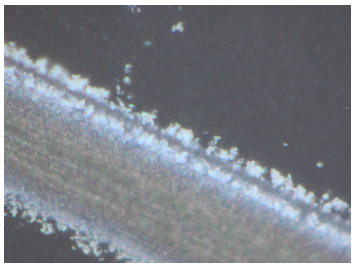 c) 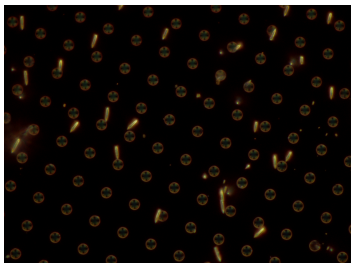

Fig. 4.1.: a) Photo of a sample b) Microscopic image of a scratch for dispersion c) Microscopic image (Nomarski contrast) of dispersed nonowires on $Si0_2$ with a grid of 10x10 μm.

Since the nanowires are too small to measure size and form accurately directly on the as-grown samples with an optical microscope, images have been taken with a high resolution secondary-electron microscope (SEM) for the doping series at the Otto-von-Guericke University in Magdeburg, Germany. As can be seen in figure 4.2 the nanowires grow dominantly along the c-axis on the sapphire substrate for the undoped as well as the whole doping series. Only a minority is tilted or coalesced with neighboring nanowires. On average the diameter size varies between $200\ \mathrm{nm}$ and $600\ \mathrm{nm}$. The average length of the nanowires varies between $1\ \mu\mathrm{m}$ and $3\ \mu\mathrm{m}$. With the increase of Sb-doping, the nanowires decrease in size and length. What should be noticed is the cone-shaped tip of the nanowires, as well as the increase of the diameter from the bottom to the top.

The change in size of the nanowires also changes the density of the sample as can be seen in the top-view images.

4.3 Antimony related bound exciton transition

For the ensemble photoluminescence (PL) measurements the samples have been mounted into a constant flux cryostat (see chapter 3.2 for setup description) and have been excited with a helium-cadmium (HeCd) laser with a wavelength of $325\ \mathrm{nm}$ ($3.81\ \mathrm{eV}$). Figure 4.3 shows a low resolution spectrum for a wider spectral overview at $5\ \mathrm{K}$ from $2.8\ \mathrm{eV}$ to $3.6\ \mathrm{eV}$.

The emission is dominated by the near band edge (NBE) luminescence where sharp peaks from the free and bound excitons can be expected in the range from $3.3\ \mathrm{eV}$ to $3.4\ \mathrm{eV}$. This area will be further analyzed in the high resolution measurement in figure 4.4. At the low energy part down from $3.3\ \mathrm{eV}$ a periodic signal is observed with

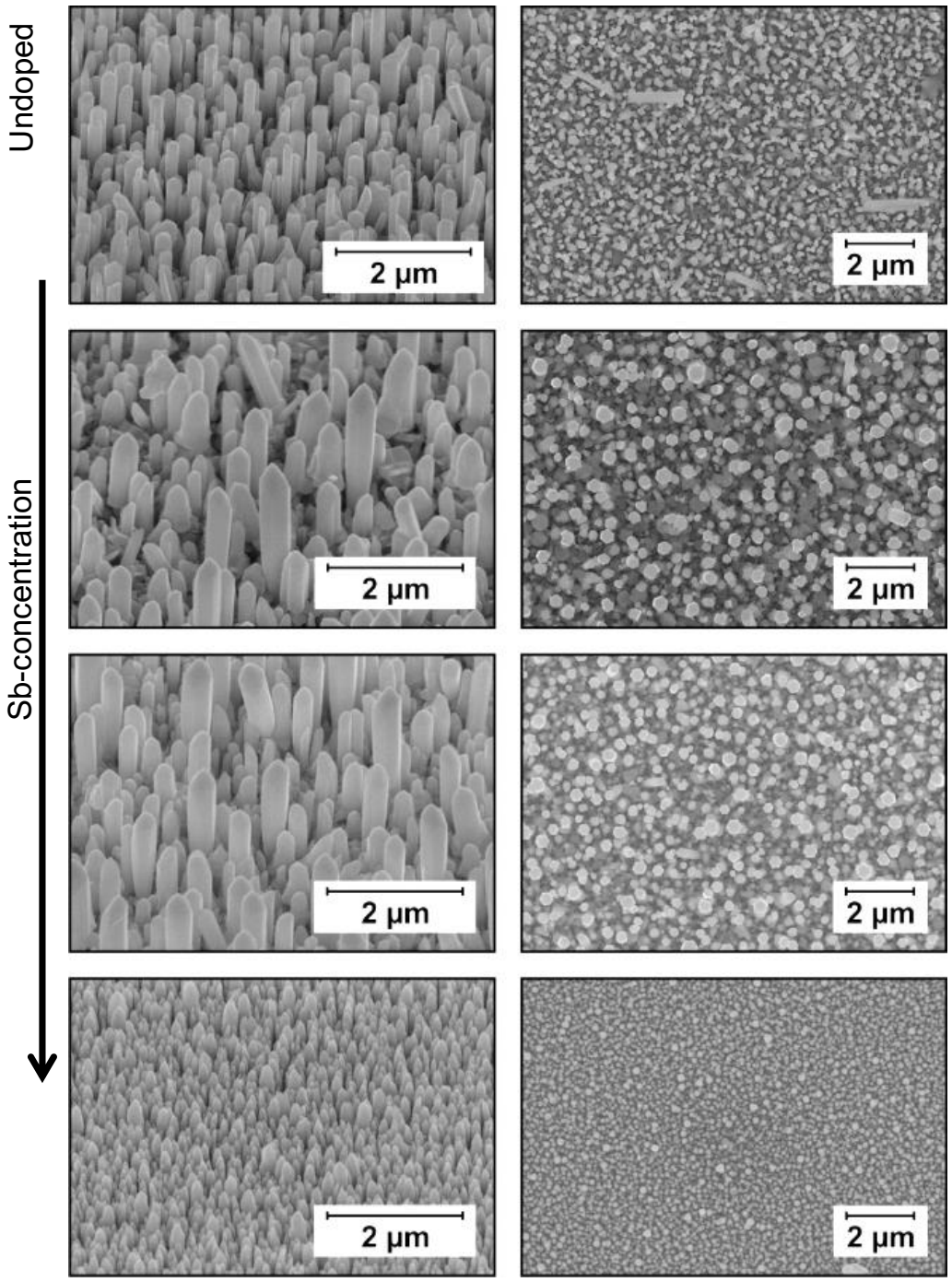

Fig. 4.2.: Secondary-electron microscope (SEM) taken at Otto-von-Guericke University in Magedburg, Germany. Side-view (left) and top-view (right) of the undoped; low, medium, and high doped sample.

an energetic distance of $72\ \mathrm{meV}$. This characteristic energy indicates that the NBE luminescence appears repetitive times in the spectra with the same recombination

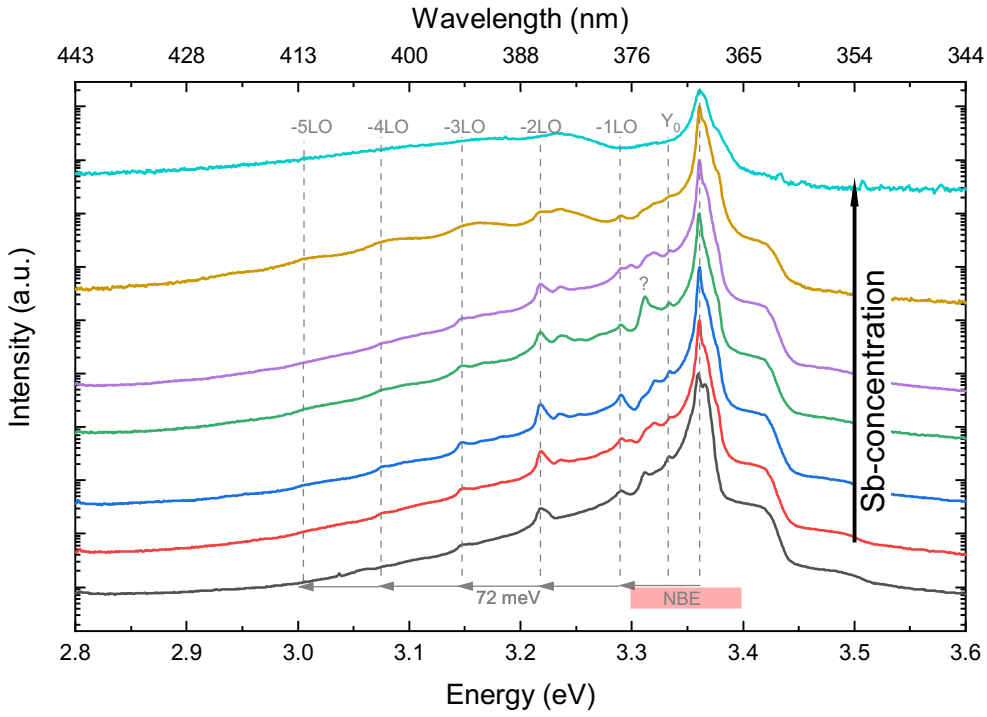

Fig. 4.3.: Low resolution photoluminescence spectra of ensemble Sb-doped nanowires (doping series) at 5 K from 2.8 eV to 3.6 eV.

process but in addition with the assistance (creation) of one or more longitudinal optical (LO) phonons of 72 meV, hence the reduction of energy. The peaks are therefore labeled with -LO and an integer indicating the number of phonons created in the process. Although the overall intensity declines for the highest doped samples it is notable that the characteristic of the dominant NBE luminescence persists throughout the series. This indicates that the samples crystal structure does not deteriorate significantly or degenerate since in this case a Moss–Burstein effect with no exciton luminescence would be expected.

A more detailed focus on the NBE at 5 K from 3.30 eV to 3.39 eV in figure 4.4 reveals several sharp peaks which can be labeled based on their energetic position in the spectra based on Meyer et al. [66]. The dominant peak is I_8 at 3.3597 eV, a neutral donor bound exciton (D^0X) with gallium as chemical origin. Since this peak is already present in the nominal undoped sample a gallium contamination of the growth reactor or the precursors is the most likely cause for it. The peak labeled I_1 is the corresponding ionized donor bound exciton (D^+X) (I_8^+) transition at 3.3714 eV. The free exciton luminescence at the high energy side is a broadened peak with two components, the transverse component of the free A exciton (A_T) at 3.3753 eV and a longitudinal component (A_L) at 3.3772 eV. The broad transition at 3.366 eV comes from a surface-bound exciton (SX) [67] which can be seen best as a

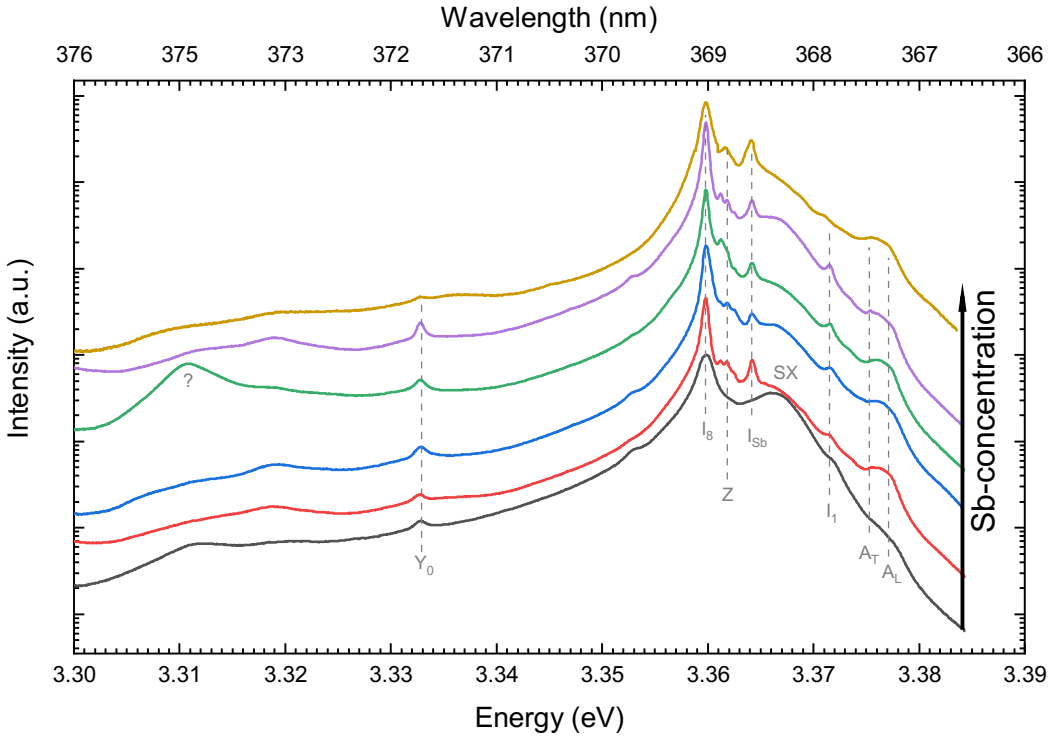

Fig. 4.4.: High resolution photoluminescence spectra focused on the NBE emission of ensemble Sb-doped nanowires (doping series) at 5 K from 3.30 eV to 3.39 eV.

symmetrical feature in the undoped sample. Its appearance is more intense in these nanowire structures than in bulk material due to the large surface-to-volume ratio. The transition Y_0 at 3.3328 eV is associated with an exciton bound to an extended structural defect [68]. Details on the specific origin of the SX and Y_0 transitions are still unknown.

Corresponding to the nominal increase of the doping an additional line I_{Sb} emerges at 3.3642 eV and suggests a causality for the incorporation of Sb. Based on a PL study by Cullen et al. [69] where ZnO had been doped with the radioactive silver isotope ^{121}Ag which decays through a chain to stable ^{121}Sb and hence shows an emerging and increasing peak in the spectrum correlated with the characteristic half-life where the chemical origin can certainly be attributed to Sb. Between I_8 and I_{Sb} three narrow lines appear mostly referred to as Z-lines at 3.3612 eV, 3.3618 eV, and 3.3623 eV. Reports of similar lines in this region have been reported earlier and denoted as X-lines [70]. Due to a systematic study of carbon-doped ZnO NW in chapter 5.2 it is evident that the Z lines originate from the incorporation of carbon. All further investigations on this doping series are carried out for the medium doped sample (green in fig. 4.4) if not indicated otherwise.

In figure 4.5 the photoluminescence spectrum is compared with its corresponding reflection spectrum.

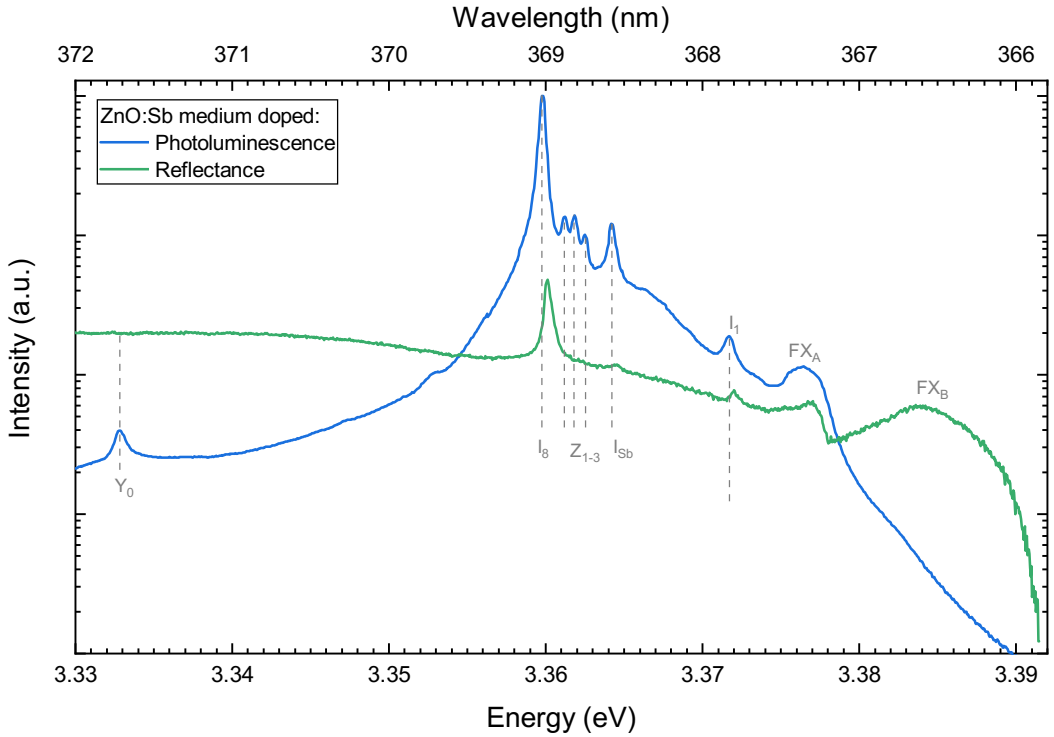

Fig. 4.5.: Comparison of high resolution photoluminescence and reflectance spectra of the medium Sb-doped ensemble nanowires at 5 K.

The individually different tilted surfaces of the nanowires with respect to the substrate surface results in a strong scattering of the light rather than a clean reflection compared to a uniform surface. This is also the reason for the optically opaque appearance. Although this makes the samples not ideal for this kind of measurement, since most of the light is lost for detection after the scattering, it is remarkable that the dominant features are still visible in the reflection spectrum. The emission peak in the photoluminescence corresponds to the turning point of the exciton oscillation in the reflection spectrum, hence the small peak shift if both measurements are compared. In addition to the free A exciton (FX_A) in the PL spectrum, the free B exciton (FX_B) is also visible on the higher energy side of the reflection spectrum.

4.3.1 Thermalization behavior

Although there is already strong evidence that the transition I_{Sb} is directly dependent on the incorporation of Sb as prior described, the specific kind of exciton transitions still need to be determined. Temperature-dependent measurements contribute to decide whether I_{Sb} is a bound exciton in a ground state such as a neutral donor/acceptor bound exciton (D^0X/A^0X) or an exciton in an excited state such as an

exciton bound to an ionized donor/acceptor (D^+X/A^+X) or a rotational/vibrational state. Due to the possible direct comparison of I_{Sb} to I_8, which is a D^0X and I_1, which is a D^+X state, as well as Y_0 where the exciton is bound to an extended structural defect, unique attributes of the nanowires which might have an influence can be excluded.

The medium doped sample was mounted as prior for figure 4.4 and the temperature was varied between 4.6 K and 120.0 K.

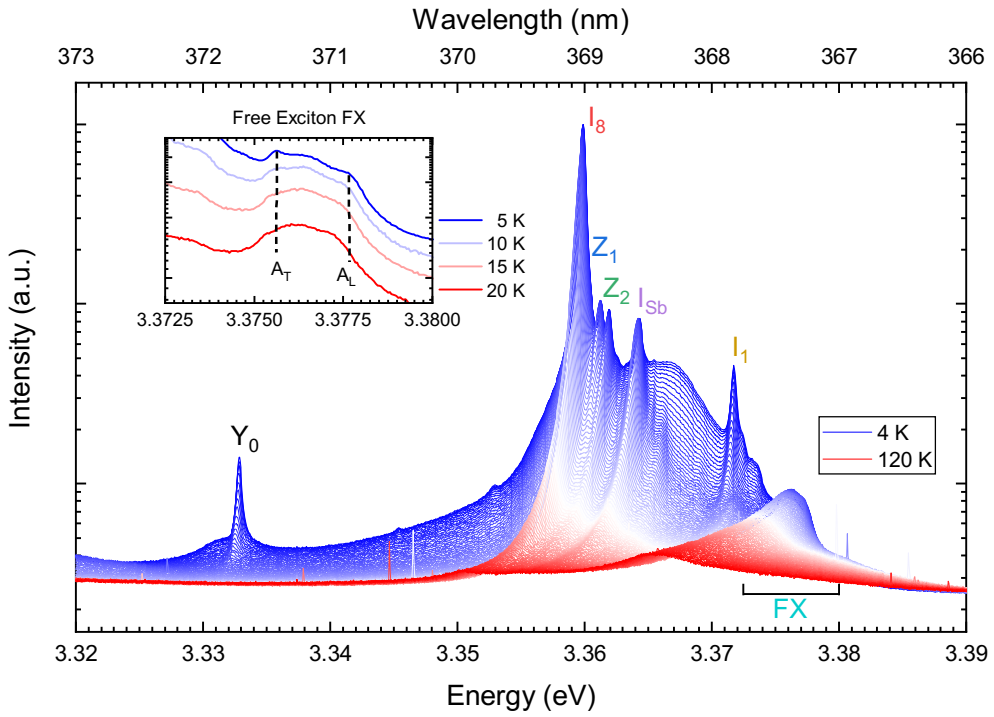

Fig. 4.6.: High resolution photoluminescence spectra focused on the NBE emission of ensemble medium Sb-doped nanowires (temperature series). Low (blue) to high (red) temperatures between 4.6 K and 120.0 K.

Figure 4.6 shows all spectra at different temperatures from low (blue) to high (red) temperatures. In general, the overall intensity of the spectrum decreases with the increase in temperature, where bound excitons dominate at low temperatures and free excitons dominate at high temperatures. In addition, all peaks shift to lower energy due to bandgap renormalization. The change in the peak form of the free exciton can be seen in the inset. At slightly more elevated temperatures the two components A_T and A_L cannot be separated anymore resulting in a broad but symmetrical peak FX. The free exciton transition is hence analyzed as a single peak. Both effects, change of intensity and position, are further analyzed separately. Figure 4.7 a) shows the change of the energetic position for different transitions based on a single Gaussian fit for every identified line in figure 4.6. Due to the

weak intensity only Z_1 and Z_2 at 3.3612 eV and 3.3618 eV respectively have been considered further in the analysis.

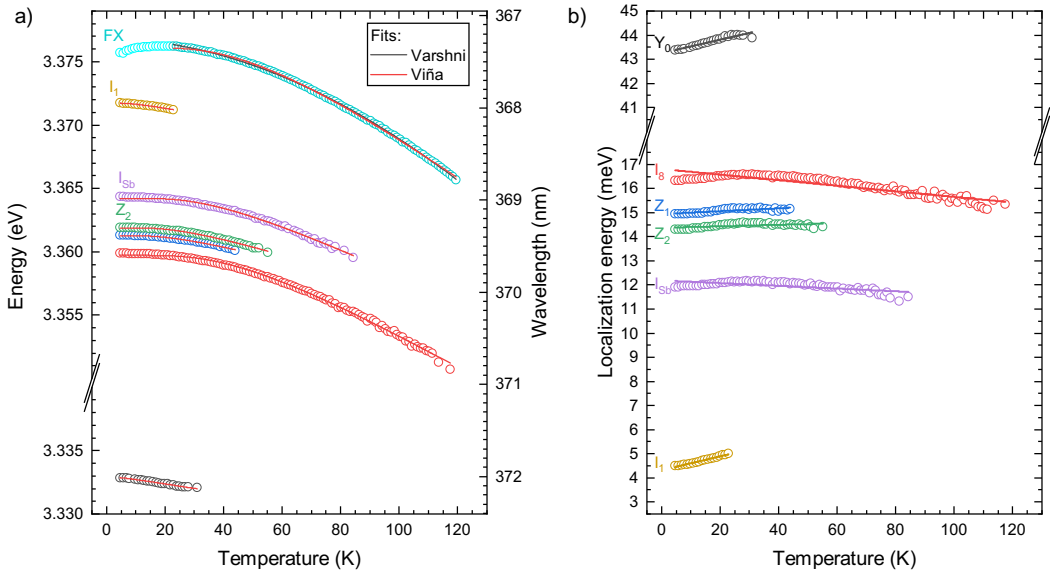

Fig. 4.7.: Energetic position of different transitions at temperatures between 4.6 K and 120.0 K. Fitted with a model by Viña [71] and Varshni [72]

.

All transitions decrease initially with increasing temperature besides the free exciton (FX), again due to the two components A_T and A_L. The A_T component quenches first when the temperature increases resulting in an initial increase. To reduce the influence of this the positions up to 20 K have been neglected for the following analysis.

There are different models to explain the shift in position with temperature [72, 73, 74, 71, 75, 76].The purely phenomenological model by Varshni [72] is used mostly throughout the literature to describe the temperature dependence of the band-gap of different materials but its coefficients α and β (see equation Varshni) are not directly connected to certain material properties. The

$$E(T) = E(0) - \frac{\alpha T^2}{\beta + T} \qquad \text{(Varshni)}$$

The free exciton is the best representative to quantify the change of the bang-gap resulting in an α and β of $(8.7 \pm 0.8) \cdot 10^{-4}$ eV/K and (1004 ± 111) K respectively which is higher than usually reported for bulk ZnO [66]. For cryogenic temperatures, however, the model by Varshni is considerably inadequate and more robust concerning its parameters at higher temperatures [76].

In contrast to Varshni the model by Viña et al. [71] (see equation Viña) is based on a Bose-Einstein model.

$$E\,(T) = E(0) - \frac{\alpha}{\exp(\theta/T) - 1} \qquad \text{(Viña)}$$

The parameter α considers the electron-phonon coupling, and θ is the effective phonon temperature.

In figure 4.7 a) all spectral positions have been fitted with the Viña model. Table 4.1 summarizes the results of the fits for the different models.

Tab. 4.1.: Fit results of the temperature-dependent PL based on the Viña model.

Line	α (meV/K)	Θ (K)
FX_A	27.8 ± 0.4	157 ± 1.6
I_1	1.1 ± 0.5	26 ± 1
I_{Sb}	13.0 ± 0.5	114 ± 3
Z_2	6.0 ± 0.4	80 ± 3
Z_1	4.5 ± 0.4	72 ± 3
I_8	19.4 ± 0.6	140 ± 3
Y_0	0.4 ± 0.2	13 ± 5

The difference between the position of the free exciton (more accurately the traverse part A_T) to the other transitions is referred to as the localization energy E_{loc}. Figure 4.7 b) indicates the temperature-dependent difference. By comparison, I_{Sb} and I_8 have a similar temperature dependency and both differ significantly compared to the Y_0 and I_1 lines. The differences are especially pronounced in the temperature behavior of the localization energy. The localization energy of Y_0 and I_1 increases persistent with increasing temperature where the localization energy for I_{Sb} and I_8 increased initially up to 20 K and then decreases. The initial increase is again caused by the simplification of the fit for the free exciton position. The decrease in the localization energy with increasing temperature is explained by an increase of free charge carriers and the accompanied screening of the impurity potential.

The change in intensity for bound excitons follows a Boltzmann statistics (see equation Boltzmann)

$$I(T) = \frac{I(0)}{1 + g \exp\left(-E_{act}/T k_B\right)} \qquad \text{(Boltzmann)}$$

where $I(O)$ is the emission intensity at $T = 0$ K, E_{act} is the activation energy, k_B is the Boltzmann constant and g is the degeneracy ratio of the considered energy levels.

Since the intensity has a reciprocal temperature dependency the data is commonly presented in an Arrhenius plot (see fig. 4.8).

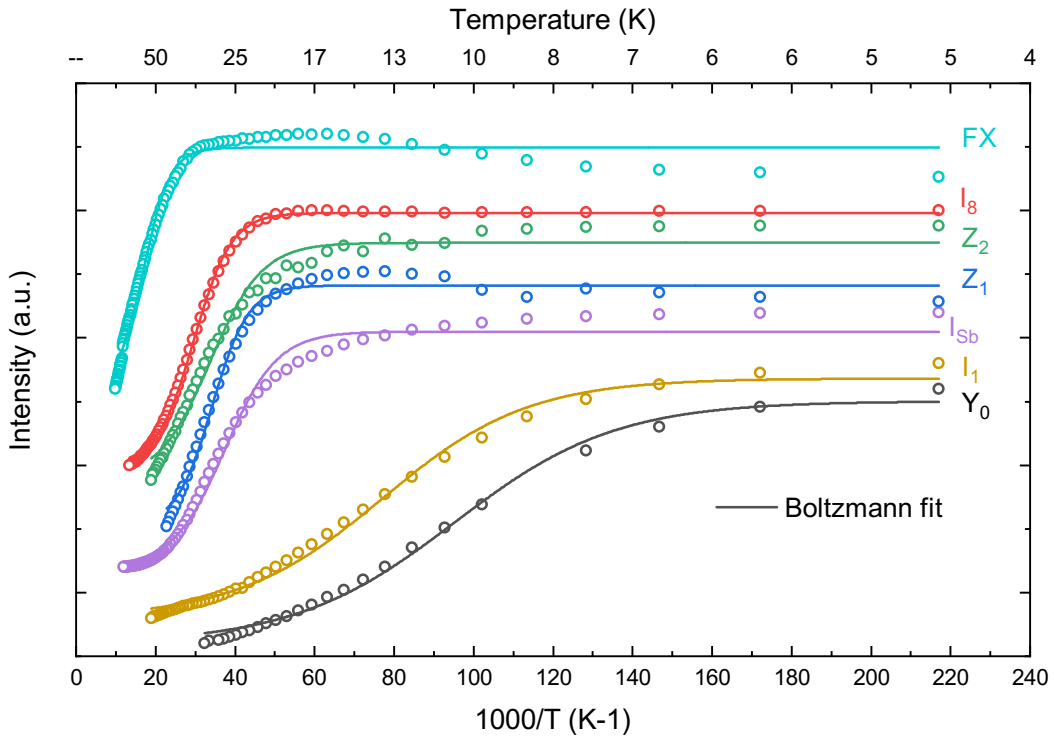

Fig. 4.8.: Arrhenius plot: Temperature-dependent change in emission intensity

The resulting activation energies are presented in table 4.2.

Tab. 4.2.: Activation energies (E_{act}) based on a Boltzmann model with g as the degeneracy ratio of the considered energy levels. Localization energies (E_{loc} as reference.)

	E_{act} (meV)	g	E_{loc} (meV)
FX_A	26.0 ± 1.0	163 ± 29	-
I_1	4.71 ± 0.14	68 ± 7	4.1
I_{Sb}	13.2 ± 0.5	305 ± 55	11.6
Z_2	13.2 ± 1.7	178 ± 43	14.2
Z_1	19.0 ± 1.9	1883 ± 675	14.7
I_8	18.4 ± 0.3	574 ± 53	16.1
Y_0	4.2 ± 0.2	111 ± 20	43.1

Although Y_0 has the highest localization energy its determined activation energy is considerable less indicating that the involved bound exciton is not bound as a whole quasiparticle to the defect center which results in a lower energy required to detach the exciton. This discrepancy to the normal trend of an exciton bound to a donor impurity has been reported for bulk ZnO in Wagner et al. [68]. For the other lines, the activation energy is similar to the localization energy. The offset in the

activation energies compared to the respected localization energies especially for Z_1 and Z_2 could be explained be underlying broader emission of the surface-bound exciton (SX) which also has a particular temperature dependence, as well as the close proximity of the lines to each other.

Based on the photoluminescence behavior in direct comparison to the I_8 transition it can be concluded that I_{Sb} is a new ground state bound-exciton transition and not an excited state of an already existing bound-exciton state as a rotational state or an ionized bound exciton. Based on the position and localization energy of the bound-exciton Sb creates a shallow state. To determine whether this state acts as a donor or as an acceptor the behavior of the transition in photoluminescence under the influence of an external magnetic field is decisive.

4.3.2 Magneto-optical properties

Photoluminescence (PL) measurements with an additional external magnetic field utilize the Zeeman effect to give further insight into the nature of the involved energy states of a transition. Section 3.2.3 explains the general concept and describes the used setup. A significant change to the prior setup is the use of a bath cryostat with a superconducting split coil to generate the magnetic field with a strength up to $5\ \mathrm{T}$. Since the orientation of the magnetic field within the cryostat is fixed the sample has to be turned by 90 degrees as well as the whole cryostat to be able to measure in the two distinct orientations (Voigt and Faraday orientation). The sample is cooled with superfluid helium whereby the low temperature measurements were done at $2\ \mathrm{K}$. Instead of a microscope objective a UV transmissive lens was used due to the required larger working distance in the cryostat. Early results on the magneto-optical properties and thermalization of Zeeman components are published in Hegde et al. [77].

For the measurement, the magnetic field has been changed continuously while the PL spectrum has been detected in short time intervals of less than a second. Figure 4.9 shows a subset of the retrieved data for integer values of the magnetic field in the region of the I_8 and I_{Sb}.

The linear line splitting in the Faraday configuration is significantly smaller than in the Voigt configuration. The dotted black and red lines indicate the different circular polarization components at $5\ \mathrm{T}$. The higher (lower) energy Zeeman component is σ^+ (σ^-) circular polarized in the Faraday configuration, whereas no polarization dependency could be observed in the Voigt configuration. Besides the polarization dependency both lines have approximately the same intensity. For the angle-dependent

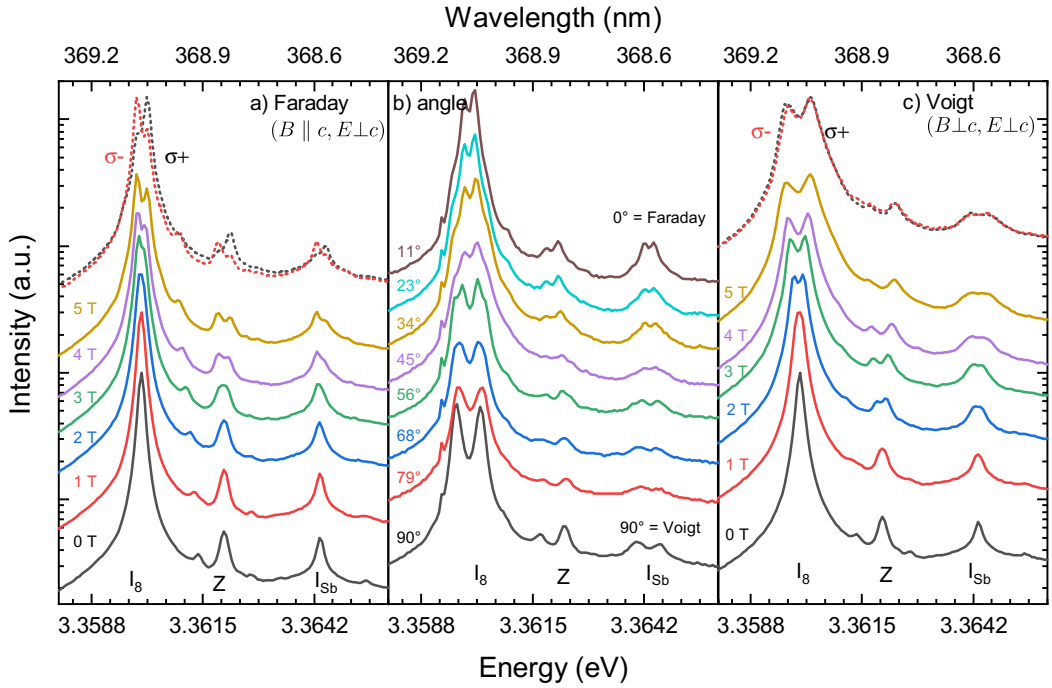

Fig. 4.9.: Photoluminescence spectra for different magnetic fields in the region of the ground-state bound excitons. a) Faraday configuration ($B \parallel c$). b) angle between B and c at 5 T c) Voigt configuration ($B \perp c$)

measurement the sample was initially set in the Voigt configuration ($\theta = 90°$) at 5 T and then rotated to change the angle between B and c. Simultaneously also the angle between E and c changed accordingly allowing not only $E \perp c$ components to contribute but also $E \parallel c$ components. The result is a 4-fold splitting with additional peaks in the shoulders of the linear split lines. In figure 4.10 the acquired spectra are presented in a contour plot for the Faraday and Voigt configuration as well as the spectral position of the I_8 and I_{Sb} line based on multiple Lorentzian fit. There are less data points for I_{Sb} due to the lower intensity compared to I_8.

To determine the electron and hole g-factors the data in the angle-dependent measurement have been fitted based on equation 3.7. Based on these values (see table 4.3) the complete 4-fold splitting for the I_8 and I_{Sb} transitions are reconstructed and presented as solid lines in figure 4.10.

Tab. 4.3.: Electron and hole g-factors for I_8 and I_{Sb}.

Line	g_e	$g_h^{\parallel}$	$g_h^{\perp}$	Ref.
I_8	1.92 ± 0.01	-1.08 ± 0.02	0.10 ± 0.04	this work
	1.92	-1.25	0.25	[17, 18]
	1.92	-1.24	0.08	[78]
I_{Sb}	1.93 ± 0.04	-1.25 ± 0.06	0.11 ± 0.12	this work

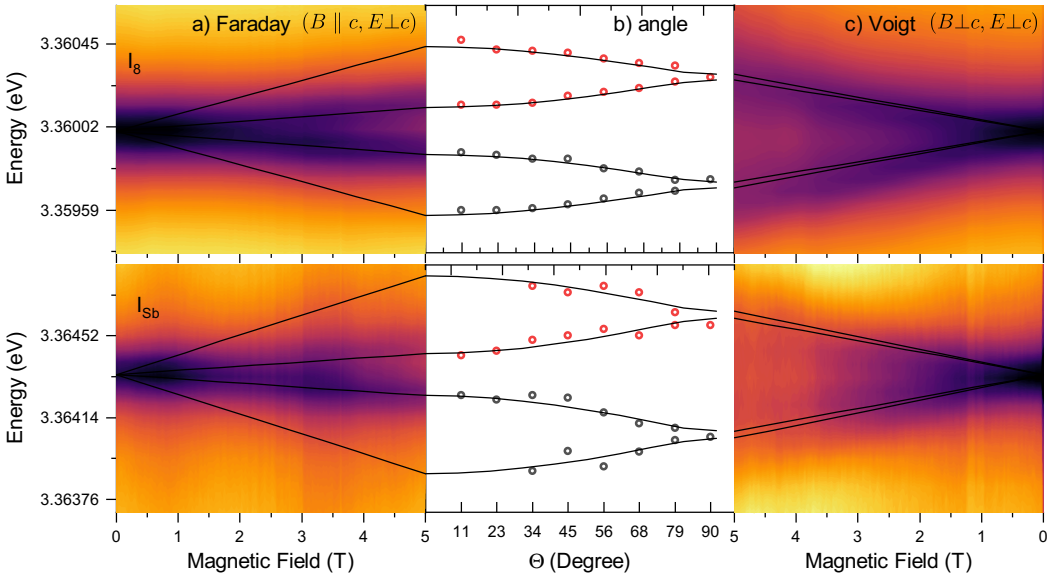

Fig. 4.10.: Zeeman splitting of the I_8 and I_{Sb} transition. All spectra as are presented in a contour plot for the a) Faraday and c) Voigt configuration. The data points in b) are based on multiple Lorentzian fits for the angle-dependent measurement at 5 T.

Both lines I_8 and I_{Sb} show similar splitting behavior with a much large splitting of the inner branches in the Voigt configuration and an additional small splitting of the outer branches to the inner branches which could not be observed in the experiment. In the Faraday configuration, the splitting of the inner branches is smaller as compared to the Voigt configuration due to $\left|g_h^{\parallel}\right| > \left|g_h^{\perp}\right|$ but show opposite circular polarization where in the Voigt configuration no polarization effect is visible. The outer branches in the Faraday configuration have a large splitting to their inner counterpart but are forbidden in this measurement geometry and were hence also not visible. In the angle-dependent measurement, the outer branches can be observed, however, due to the mixed geometry. Since no crossing of the inner branches occurred it can be concluded that no exciton with a hole of Γ_9-symmetry is involved. In contrast to the neutral-bound excitions, no splitting for the ionized-bound excition is expected. This can be seen in figure 4.11 which shows the spectra for the D^+X region up to the free A-exciton.

At higher magnetic fields additional lines appear and rise with magnetic field strength at the lower end of the I_1 and FX line. These peaks are the corresponding transverse components of I_1 and FX which are normally (weakly) forbidden in this geometry and become allowed with an additional magnetic field [79]. To determine whether I_{Sb} is an acceptor or rather a donor-bound exciton like I_8 the renormalization ratio of the Zeeman components is crucial. Figure 4.12 shows the peak shift and change in intensity for I_8 (top) and I_{Sb} (bottom).

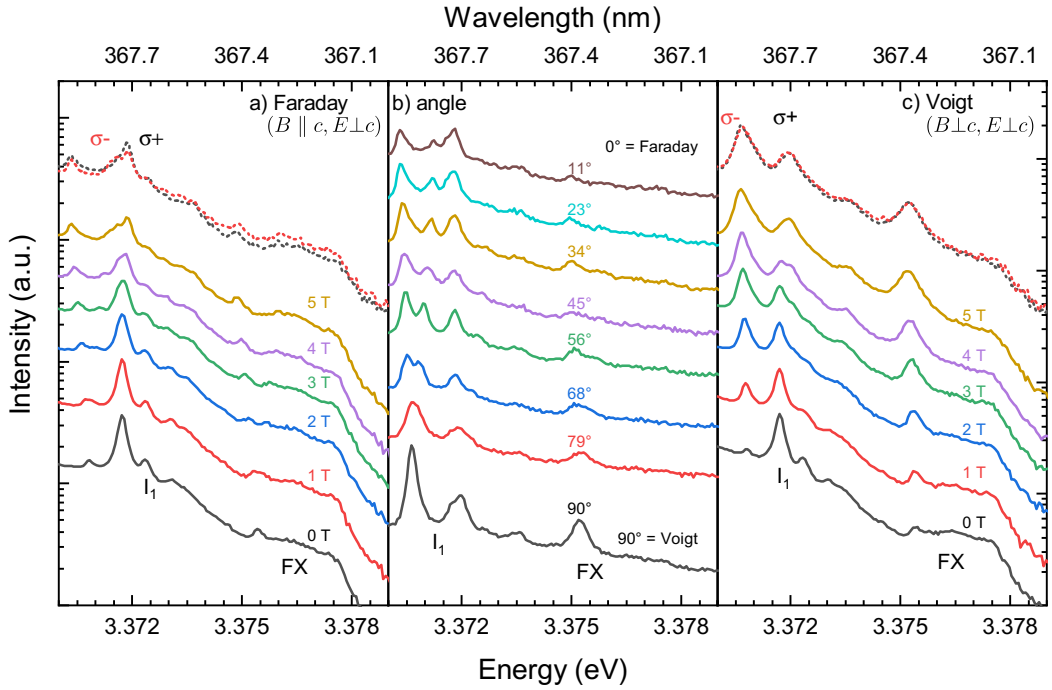

Fig. 4.11.: Photoluminescence spectra for different magnetic field in the region of the ionized-state bound and free excitons. a) Faraday configuration ($B \parallel c$). b) angle between B and c at 5 T c) Voigt configuration ($B \perp c$)

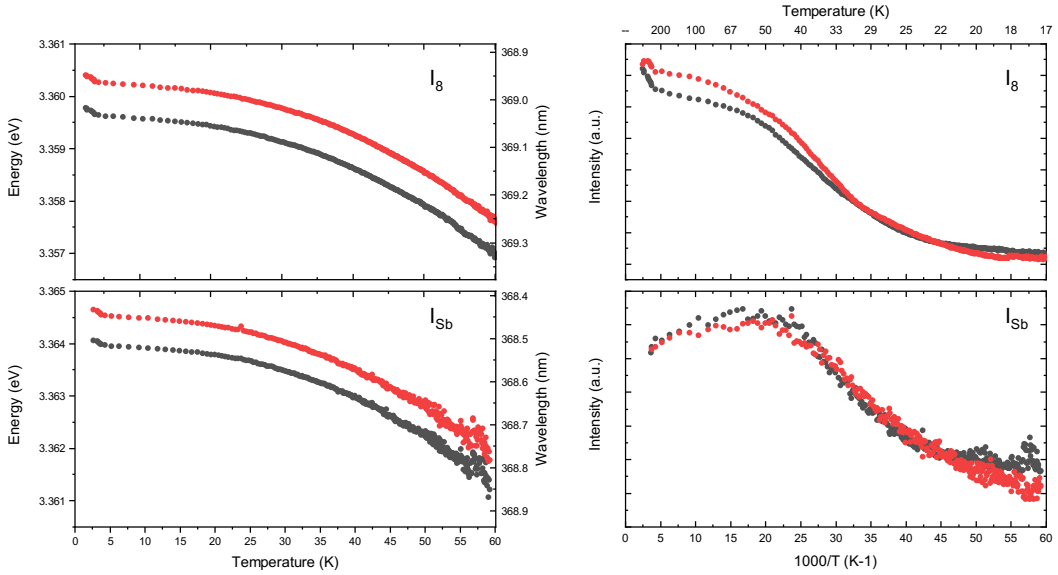

Fig. 4.12.: Temperature dependency of the I_8 (top) and I_{Sb} (bottom) transition at 5 T

As described in 3.2.3 the Zeeman splitting is determined by the corresponding g-value, where g_e for an electron is significantly greater than for the hole g_h. Since the exciton binds with its electron (hole) on a donor (acceptor) the Zeeman splitting is predominantly defined by the ground (excited) state splitting. In PL the thermal-

ization is in contrast to absorption dependent on the splitting of the excited state. Both Zeeman components do however quench simultaneously for the I_8 and I_{Sb} transition. Both lines are hence neutral donor bound excitons D^0X involving an A-exciton with Γ_7-symmetry for the electron and hole.

4.3.3 Excited states

While in photoluminescence (PL) the excitation energy normally exceeds the bandgap, the detected emission is also normally off-resonant. Contrary in photoluminescence excitation (PLE) spectroscopy the excitation energy is tuned so that in the case of a resonant excitation an enhancement of the intensity can be detected and reveal additional associated states.

As a tunable source, a dye laser has been used as described in chapter 3.2.2. Since the dye-laser is optically pumped by an excimer-laser the main difference to the prior measurements is the pulsed excitation with ns-pulses, a repetition rate of $100\ \mathrm{Hz}$ and therefore a repetition time of $10\ \mathrm{ms}$. This yields two disadvantages: Firstly, the laser excites the sample only within the pulse duration and since the transient time of the photoluminescence is normally short (fs to ps) the emission from the sample is also emitted as a ns-puls. The CCD however can detect photons throughout the whole repetition time which drastically reduces the signal-to-noise ratio since most of the time the sample does not emit any photons. Secondly, a higher excitation density within the laser puls can result in the generation of much more free carriers as in the case of continuous excitation which could make the formation of excitons impossible due to screening. To avoid this the excitation power was reduced drastically. Both effects combined prevent the detection of an ordinary photoluminescence spectrum as in figure 4.4. Therefore a spectrum with a helium-cadmium (He-Cd) laser was measured prior to the PLE. The dye-laser is initially set to an energy above the bandgap of the nanowires and then tuned down while the CCD detects the PL signal.

In figure 4.8 the different excitation-dependent PL spectra are oriented horizontally as a contour plot. The reflected laser is also detected to calibrate the excitation energy. The detection is logarithmically scaled and two additional peaks on each side of the laser can be seen which comes from the laser setup itself. The positions of the regarded PL transitions are labeled on top of the graph. As can be seen, the intensity of these lines varies significantly depending on the excitation energy. To get the PLE spectrum for each transition vertical profiles are taken out of this contour plot and plotted with the reference He-Cd PL spectrum in figure 4.14.

In the PLE spectrum, distinct excitation channels are visible and labeled with integers. The corresponding ground state to each PLE spectrum is marked in the PL spectrum. Transitions involving a hole from the B-valence band are reported

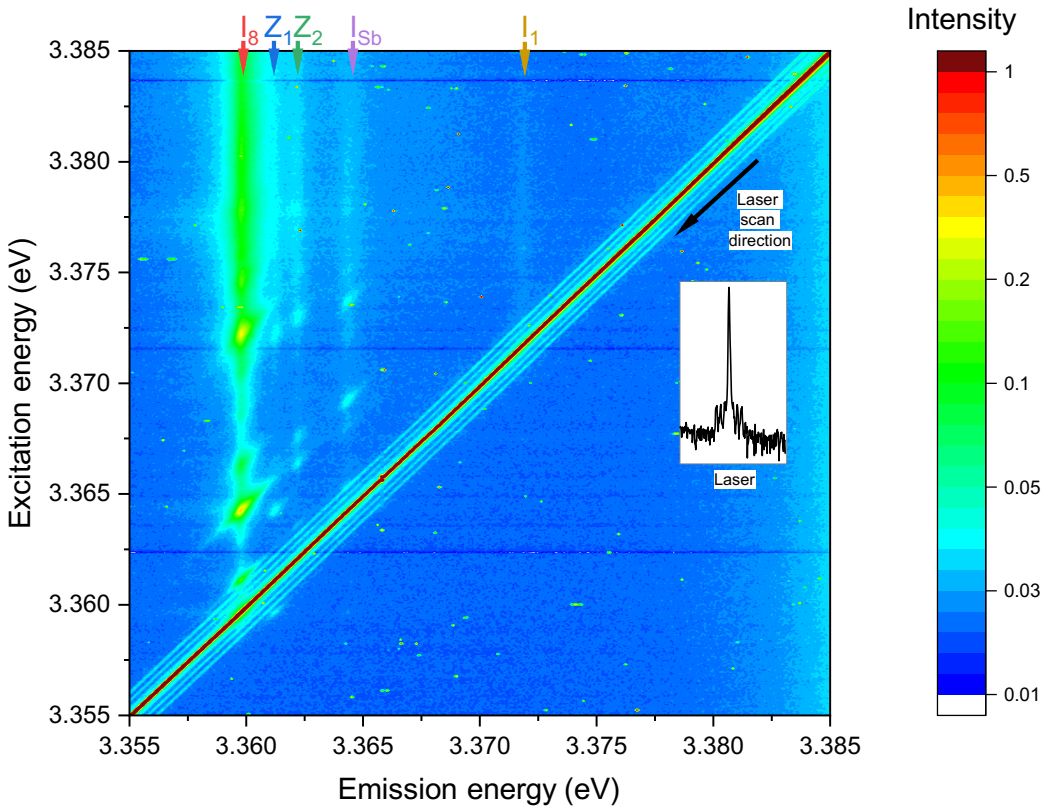

Fig. 4.13.: Photoluminescence excitation (PLE) of Sb-doped ZnO nanowires. The contour plot shows all PL spectra with varying excitation energy.

4.5 meV higher than the ground state [80, 81], hence here indicated by a dotted reference line. The peak at 3.379 eV is visible for all transitions at the same energetic position and most likely the resonant excitation via the free A-exciton. In Table 4.4 the relative and absolute peak positions are presented.

Tab. 4.4.: Absolute and relative Positions of the peaks found in the PLE spectrum of Sb-doped nanowires

		0	1	2	3	4	5	6	7	8
I_8	Pos. (eV)	3.35979	3.36109	3.36426	3.36633	3.36866	3.37068	3.37225	3.3747	3.3770
	Δ (meV)		1.3	4.5	6.5	8.9	10.9	12.5	14.9	17.2
Z_1	Pos. (eV)	3.36123	3.36424	3.36576	3.36758	3.36840	3.3722			
	Δ (meV)		3.0	4.5	6.3	7.2	11.0			
Z_2	Pos. (eV)	3.36191	3.36639	3.36752	3.3730					
	Δ (meV)		4.5	5.6	11.1					
I_{Sb}	Pos. (eV)	3.36433	3.36532	3.36626	3.36810	3.36922	3.37214	3.37373	3.3751	
	Δ (meV)		1.0	1.9	3.8	4.9	7.8	9.4	10.8	

Sb shows again a similarity to I_8 but with a compressed spacing as can be expected from a shallower donor state. According to Meyer et al. [81] rotational and vibrational states can be expected between the ground state involving the A-exciton

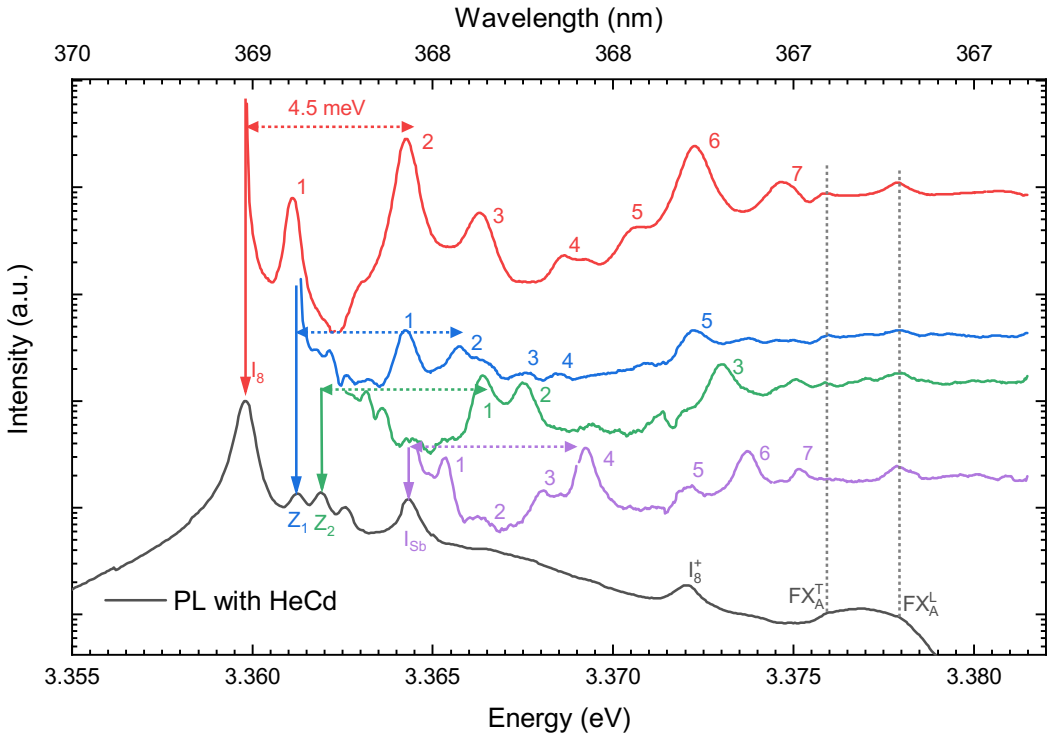

Fig. 4.14.: Photoluminescence excitation (PLE) profiles of Sb-doped ZnO nanowires. The PL spectrum (black) is a reference excited with a He-Cd-laser.

(D^0X_A) and the ground state involving the B-exciton (D^0X_B) and excited states with energies higher than (D^0X_B).

4.3.4 Photoluminescence of single dispersed nanowires

All prior measurements have been carried out for the as-grown sample, hence for an ensemble of different nanowires. To investigate whether the properties of a single nanowire are comparable to an ensemble single nanowires have been investigated. The procedure for the dispersion of the nanowires is described in 3.2.1 as well as the description of the setup. Again the analysis is focused on the medium doped sample.

Figure 4.15 shows the power-dependent photoluminescence of a single dispersed nanowire on sapphire. The specified power is the nominal power of the cw laser excitation of the helium-cadmium (He-Cd) laser measured behind the microscope objective. To be able to convert this into an excitation energy the spot size of the laser is necessary and was assumed to be in the order of $1\ \mu\mathrm{m}$ for the conversion. Since the nanowires are likely to be smaller than this although the precise size cannot be determined here the values should be used just for a rough reference.

The PL spectrum for a single nanowire is not drastically different from that for the ensemble. The near band edge luminescence dominates the spectrum with the I_8 at

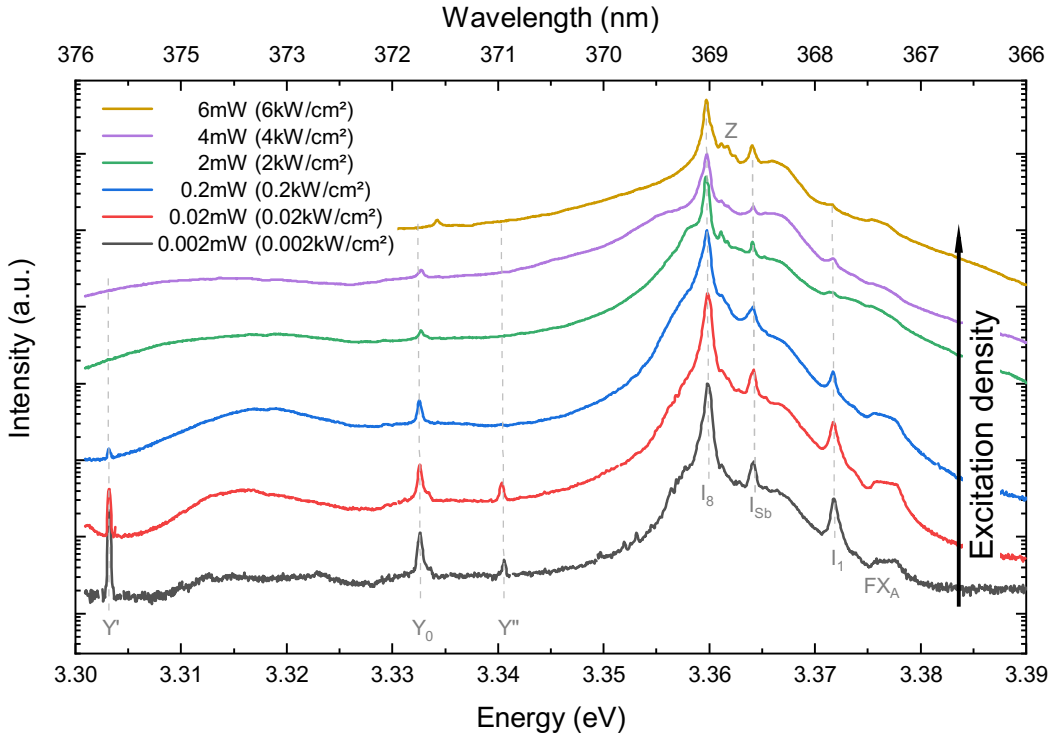

Fig. 4.15.: Power-dependent photoluminescence of a single dispersed nanowire of the medium doped sample.

3.3598 eV. At lower excitation density two additional lines appear at 3.3032 eV and 3.3406 eV labeled as Y' and Y'' respectively, due to their similarity to Y_0 at 3.3327 eV. Also, the ionized donor-bound exciton I_1 at 3.3719 eV is more prominent in lower excitation density as well as the form of the free A-exciton with its transverse and longitudinal components. These effects at lower power excitation are visible due to less screening caused by fewer free charge carriers. This is also in agreement with why in the D^+X region of the PLE spectrum (see figure 4.13) the observed I_1 was considerably weaker as in the normal PL setup. Contrary to these findings the Z-lines between I_8 and I_{Sb} are much more prominent for higher excitation densities.

Several single nanowires have been mapped in the confocal micro-PL (μ-Pl) setup. Figure 4.16 shows the mapping for four different nanowires. The intensity has been integrated over the whole spectral range.

In figure 4.16 a) the elongated form of a nanowire can be seen in the middle of the map but its size appears to be much greater than what would be expected from the optical or SEM image. As can be seen from the isolines (lines of constant intensity) of the contour plot is that the deduced size is dependent on the contrast. Since the intensity in the background of map a) barely shows a constant background a larger area has to be mapped. Map b) therefore covers a larger area. The elongated nanowire form is distorted at the bottom of the map. In map c) a distortion is also

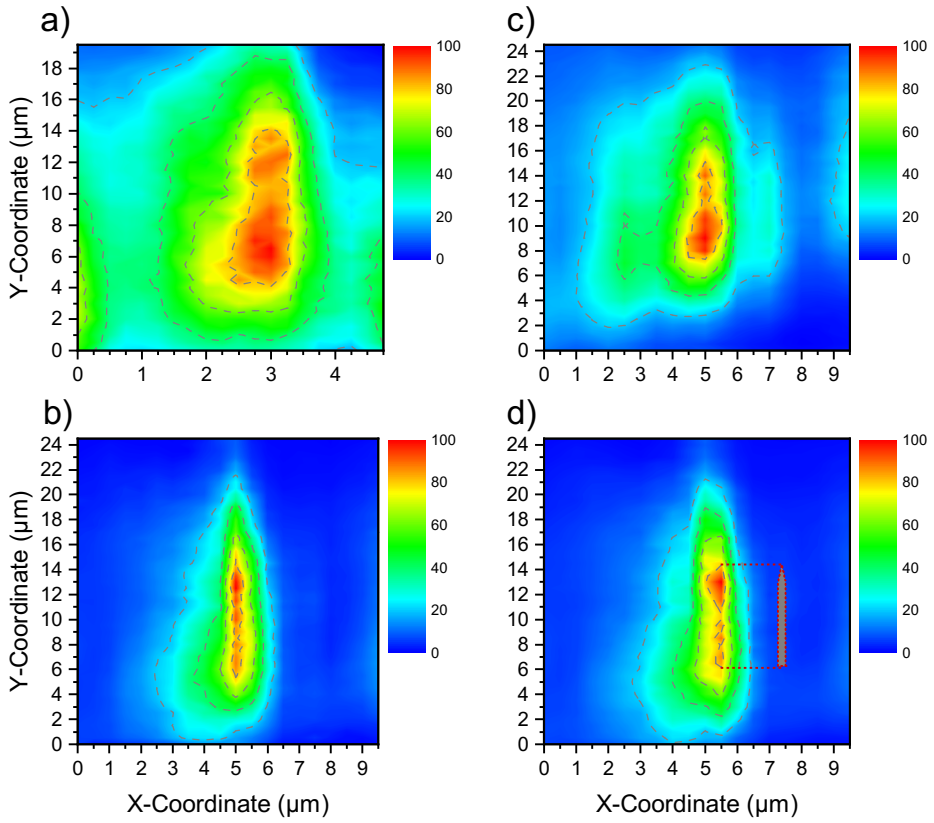

Fig. 4.16.: Lateral mapping of of four dispersed single nanowires

present but in addition, there seems to be ghosting where additional nanowires appear next to the image. This could be caused by a not optimized focus. In map d) the nanowire form is still distorted but it can be estimated that one end, the tip or the bottom, has a higher intensity than the other. However, the mapped size is still much larger than the real size.

It can be concluded that the mapped size of the nanowire is not only the result of the convolution of the excitation laser spot size and the real size of the nanowire. In fact, the detected signal is the integrated intensity over the whole field of view of the setup. Figure 4.17 presents two images seen through the microscope.

Figure 4.17 a) shows the field of view while an additional LED background illumination is turned on. The camera is a standard gray-scale microscope CCD. Since standard CCDs normally have a very low sensitivity below $350\ \mathrm{nm}$ without an additional coating that converts UV into visible light the laser is not directly visible in the images. However, an area of diffusely scattered light of the laser is present. In the center, the emission of a single isolated nanowire can be seen. In b) the back illumination is turned off and an additional emission of another nanowire can

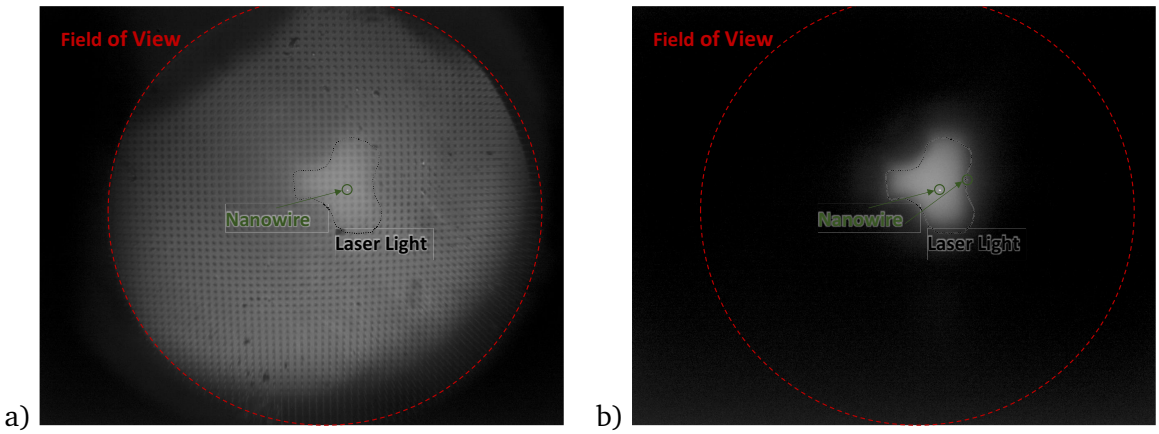

Fig. 4.17.: a) Field of view of the micro-PL setup with illumination on. The laser is diffuse scattered and a single nanowire is visible in the center b) With the illumination off an additional nanowire is visible on the right side.

be seen on the right hand side of the scattered laser light area. Surprisingly the scattered laser is already sufficient to excite a nanowire and since the whole field of view is been detected a distortion occurs if the nanowire is not isolated within the field of view and other nanowires can contribute. This effect could be reduced if the field of view is decreased by spatial filtering which requires additional optics or by a reduction of the density of the dispersed nanowires. Another way is to reduce the likelihood of the excitation of peripheral nanowires. In PL this can optically be achieved by changing to two-photon absorption. Another way to excite the sample with similar properties is the use of an electron beam.

4.4 Cathodoluminescence for increased lateral resolution

In cathodoluminescence (CL) the excitation of the sample is not done by a laser but with an electron beam. All CL measurements were made by Marcus Müller and Peter Veit at the Otto-von-Guericke University in Magdeburg, Germany. The excitation with an electron beam has basically two advantages. Firstly, the focus of the electron beam can be much smaller due to the smaller de-Broglie wavelength of electrons compared to UV photons, hence a higher lateral resolution is possible. Secondly, the electron beam can be deflected electrically or magnetically, and therefore no mechanical movement is required to probe a sample. Simultaneously the precise location can more easily be depicted by the use of secondary electron microscopy (SEM). With the use of a scanning transmission electron microscopy (STEM) in CL mode even higher spatially resolved measurements are possible.

Figure 4.18 shows how precise the selection of a single nanowire is possible compared to an optical microscope. In c) the single nanowire on the top has been measured by CL.

4.4.1 Cathodoluminescence

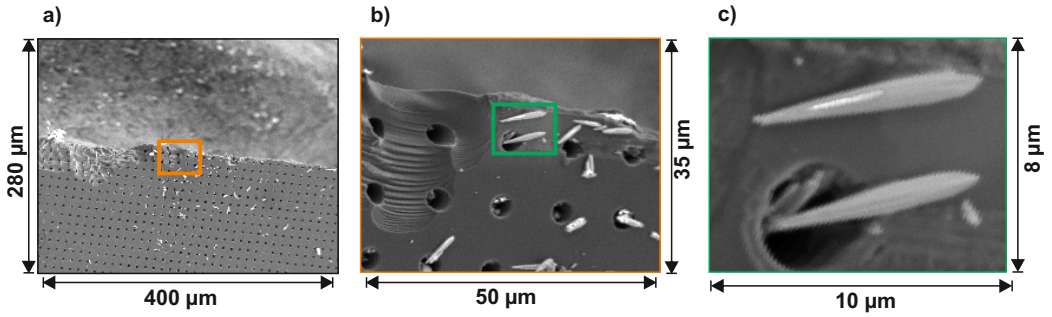

Fig. 4.18.: Secondary electron microscope image a) overview b) close up on the substrate edge c) single nanowire used for cathodoluminescence

For reference a single intentionally undoped nanowire has been measured by CL. Figure 4.19 shows the two linescans, a) from the bottom to the top of the nanowire and b) a scan from edge to edge. The undoped nanowire predominantly

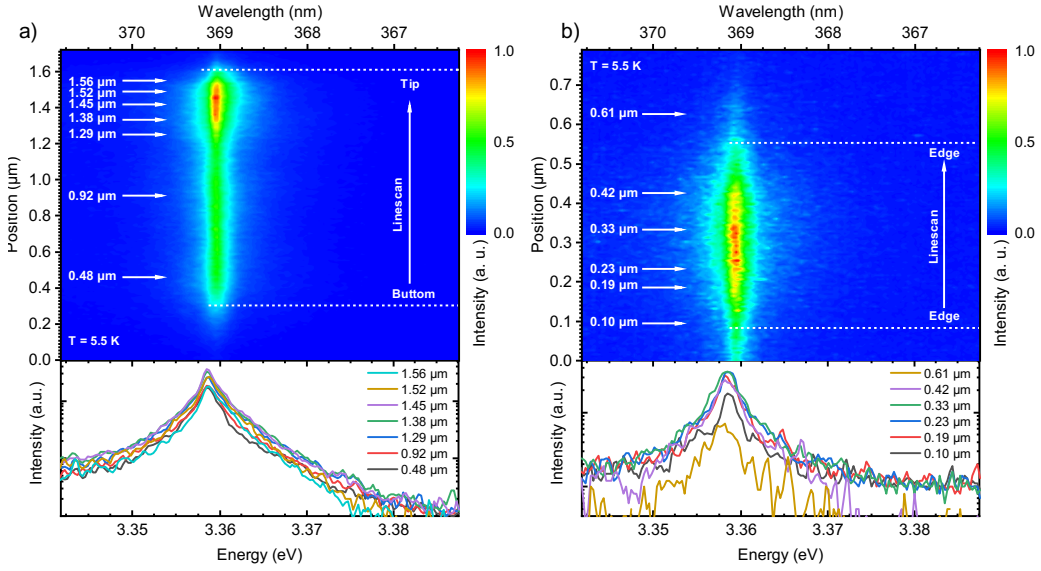

Fig. 4.19.: Cathodoluminescence of a single undoped nanowire a) linescan from bottom to the tip and b) from edge to edge. The graph below shows the detected spectra at the specified position along the scan.

emits spectrally at the near band edge which was also the case by exciting optically (chapter 4.3) with the gallium donor-bound exciton I_8 line. The intensity is highest

at the tip of the nanowire although the different spectra are quite similar along the linescan. The contour plots intensity is scaled linearly. A linescan from edge to edge at a point close to the tip indicates that the emission is quite homogenous radially. The higher intensity at the tip can be explained with a higher incorporation of dopants, gallium in this case or by the larger nanowire volume or surface due to the cone-shaped tip.

Figure 4.20 shows the same experiment but with the medium doped sample.

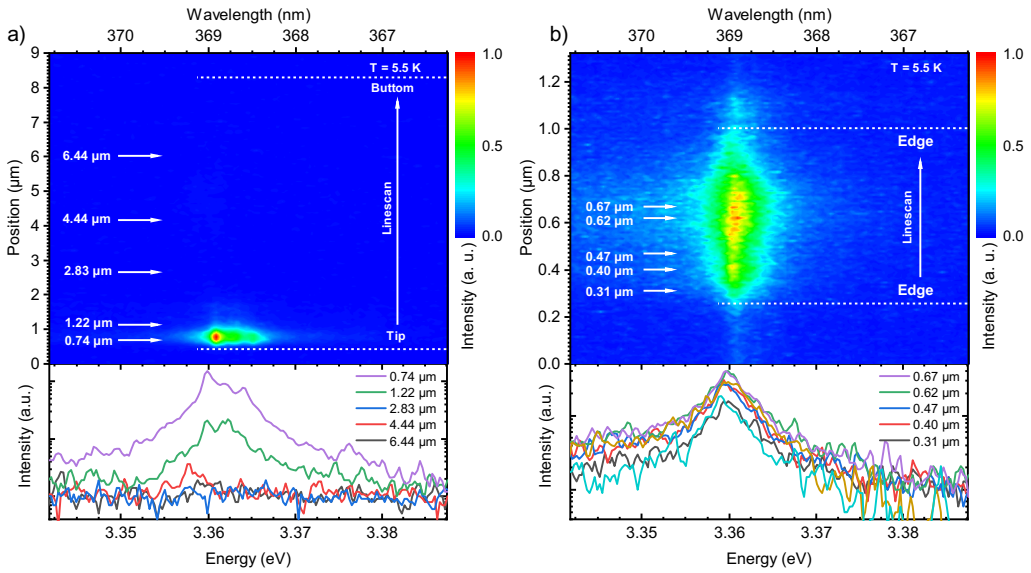

Fig. 4.20.: Cathodoluminescence of a single medium doped nanowire a) linescan from bottom to the tip and b) from edge to edge. The graph below shows the detected spectra at the specified position along the scan.

Again for the medium doped sample, the intensity at the tip is higher but contrary to the undoped sample the intensity differs by two orders of magnitude compared to the rest of the nanowire. A linescan from one edge to the other at a location close to the tip again shows a homogenous intensity. The difference of the intensity at the tip compared to the bottom is unlikely caused by a volume or surface effect if the undoped sample is used as a reference. Although the I_8 line is still the predominant peak throughout all locations as can be seen in the spectra in figure 4.20 a) at the bottom, I_{Sb} also rises significantly towards the tip.

To distinguish whether this might be a surface effect or if the emission comes from the whole volume of the nanowire additional cathodoluminescence measurements with a scanning transmission electron microscopy are presented in the next section.

4.4.2 Cathodoluminescence with scanning transmission electron microscopy

For this measurement, nanowires have been dispersed on a TEM-grid and placed on a cryo-sample holder inside a scanning transmission electron microscopy (STEM). Besides CL measurements also annular dark-field (ADF) and high-angle annular dark-field (HAADF) images have been obtained. Figure 4.21 shows the results for the medium doped sample.

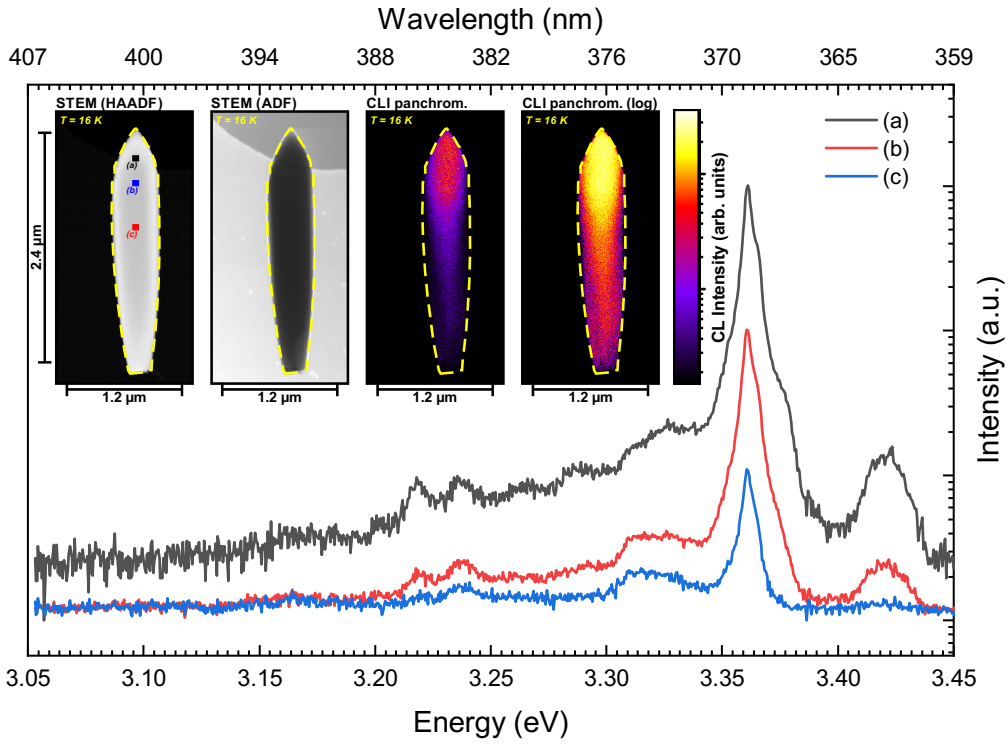

Fig. 4.21.: High-angle annular dark-field (HAADF), and annular dark-field (ADF), panchromatic cathodoluminescence intensity (CLI) with a linear intensity scale as well as CLI with a logarithmic scale.

In the inset, the ADF and HAADF show the outline of the nanowire form with the cone-shaped tip. The outline has been used to assign the spatial distribution of the CL signal. Again, the polychromatic emission stems predominantly from the tip. Single spectra are carried at the indicated points a), b), and c). Unfortunately, the spectral resolution is not sufficient to distinguish individual peaks of the near-band edge luminescence. The spectrum is however similar to the overview PL spectra with low resolution (see fig. 4.3).

The CL measurements affirm the stronger luminescence at the tip of the nanowires. A volume effect can be ruled out since the undoped nanowire does not show such a significant difference. It is still unclear if this effect stems from higher

incorporation of dopants or if the incorporation somehow induce defects which alters the luminescence below the tip. Although the ADF and HAADF signal does not reveal extended structural defects the identification of defects in STEM is far from trivial and therefore defects cannot be ruled out as the cause for the intensity difference.

4.5 Antimony related phonons

The origin of the traces in the luminescence is the incorporation of dopants but from the luminescence alone it is not possible to determine unambiguously whether dopants have been incorporated at the specific location or not. Hence an additional method is necessary. Secondary ion mass spectrometry (SIMS) could reveal the composition of the lattice but it is a very challenging method for nanowires since the nanowire needs to be embedded into a matrix to ensure a layer-by-layer ablation. The incorporation of dopants into the crystal lattice can result in distinct traces in the Raman spectrum as local vibrational modes occur. Therefore, in the next section, the effect of the dopants is analyzed by Raman spectroscopy of the as-grown samples. To increase the lateral resolution and to analyze a single nanowire tip-enhanced Raman spectroscopy (TERS) was performed by Emanuele Poliani (Technische Universität, Berlin, Germany). Both techniques are described in chapter 3.3.

4.5.1 Local vibrational modes

To identify whether Sb have distinct traces, Raman spectroscopy measurements have been carried out for the ensemble as-grown samples. In Figure 4.22 the spectra of the series is presented between $80\ \mathrm{cm}^{-1}$ and $780\ \mathrm{cm}^{-1}$ which is the region of the first order host modes of ZnO as well as where local vibrational mode would be expected.

In the low energy range up to approximately $180\ \mathrm{cm}^{-1}$ the background stems from the filter and alignment of the setup and is visible in a variety of different samples. To identify the specific modes in the spectra the peaks have to be distinguished by ZnO host modes [59, 56], Al_2O_3 (Sapphire) modes [82] which come from the substrate of the nanowires, additional modes which occur if ZnO has been doped with N [83] or Fe, Sb, Al, Ga, N [84]. Some of the modes occur independently of the specific dopant and are likely just caused by the doping but may not involve the dopant itself in the mode. In contrast, some modes do occur exclusivity for distinct dopants such Sb [84].

In the spectra, the gray solid lines are visible ZnO host modes. The gray dotted lines are ZnO host modes for reference which would not be expected here since

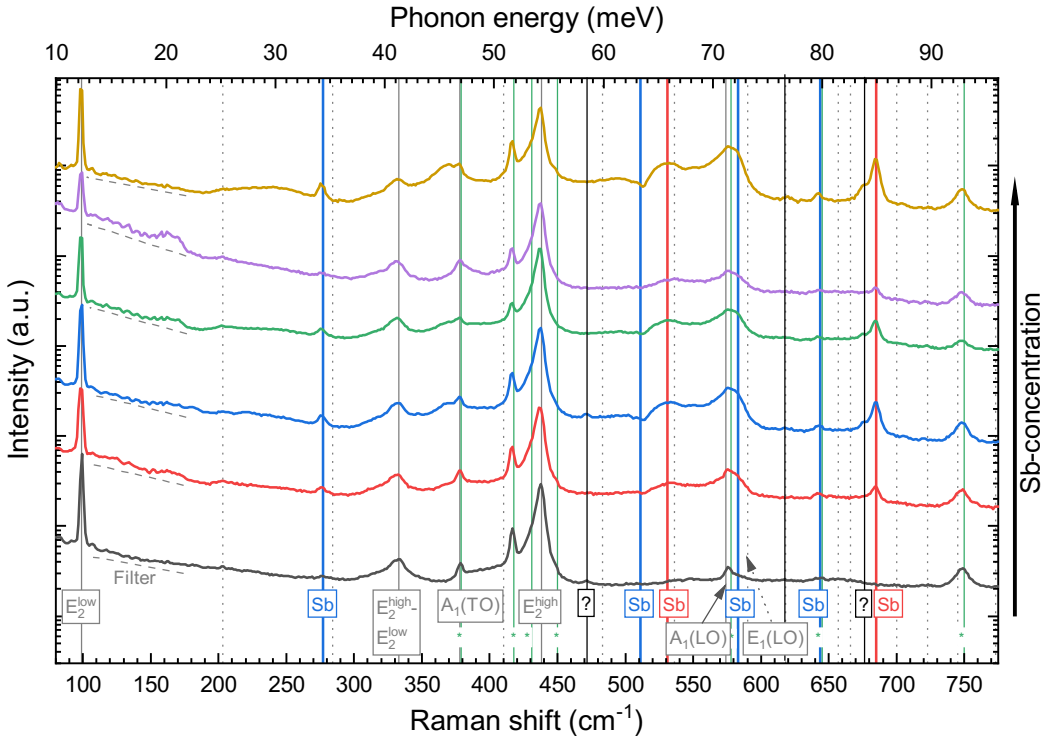

Fig. 4.22.: Raman specroscopy of the doping series of the ensemble. Gray bold lines are ZnO host modes. Blue bold lines are Sb-doped related local vibrational modes. Red bold lines are local vibrational mode which are related exclusively on Sb-doping. Gray dotted lines are ZnO modes involving acoustic modes. Green bold lines marked with an asterisk are Al_2O_3 modes which stem from the substrate.

these modes are either not active at the Γ-point (involving acoustic modes) or are not allowed in this specific $z(x,x)\bar{z}$ geometry. The green lines labeled with an asterisk stem from the substrate. The additional modes marked with solid blue lines labeled with Sb have been prior reported with Sb doping while the red lines have been exclusively reported for Sb-doping. Since some peak positions have double or more occupancy table 4.5 indicates all possible origins in proximity. The Sb-related additional modes (blue and red lines) are visible in contrast to the undoped sample besides the mode reported at $511\ \mathrm{cm}^{-1}$ where interestingly a dip is visible. It is of importance to note that these additional modes also have to obey selection rules in general and might be inactive in specific geometries. The $511\ \mathrm{cm}^{-1}$ for instance is hardly visible in Fe:ZnO thin films in the $z(x,x)\bar{z}$ geometry but clearly visible in the $x(y,z)\bar{x}$ geometry [84]. Unfortunately Raman spectra for different geometries of high quality Sb:ZnO has not been reported yet.

The intensity of the Sb-related modes does not directly follow the nominal Sb-concentration of the sample series compared to the intensity of the Sb-peaks in the PL. For the Raman measurements, a $100X$ objective has been used in contrast to a

Tab. 4.5.: Summary of the identified Raman modes. Peak position and width are based on Lorentzian fits.

Frequency (cm^{-1}) This work	width	Ref.	Origin	Symmetry	Process	Ref.
98.6	1.1	99, 101	ZnO	E_2	E_2^{low}	[59, 56]
275.6	6.5	275-277	Fe, Sb, Al, Ga, N			[84, 83]
332.6	22.6	333, 332	ZnO	$A_1, (E_2, E_1)$	$E_2^{high} - E_2^{low}$	[59, 56]
377.0	5.4	378, 380	ZnO	A_1	$A_1(TO)$	[59, 56]
		378.7	Al_2O_3	E_g		[82]
416.6	5.0	417.4	Al_2O_3	A_{1g}		[82]
436.7	7.4	430.2	Al_2O_3	E_g		[82]
		438, 437	ZnO	E_2	E_2^{high}	[59, 56]
–	–	448.7	Al_2O_3	E_g		[82]
–	–	510-513	Sb, Fe Al, Ga, N			[84, 83]
533.4	**94.0**	**531**	**Sb**			[84]
		536, 541	ZnO	A_1	$2B_1^{low}; 2LA$	[59, 56]
		574, 574	ZnO	A_1	$A_1(LO)$	[59, 56]
576.0	28.8	576.7	Al_2O_3	E_g		[82]
		583	Fe, Sb, Al, Ga, N			[84, 83]
642.0	3.1	644.6	Al_2O_3	A_{1g}		[82]
		644	Fe, Sb, Al, Ga, N			[84, 83]
684.5	**7.0**	**685**	**Sb**			[84]
747.7	12.0	750.0	Al_2O_3	E_g		[82]

$20\ X$ objective in micro-Pl or a lens in the normal PL setup. This would generally result in a smaller spot size and hence a smaller number of nanowires contribute. The Raman effect as a scattering process is additionally very sensitive to the power density and hence a small focus is optimal. In PL this is not necessarily the case. Due to a saturation effect of single nanowires a larger spot size can increase the overall signal if more nanowires contribute but with a smaller power density to avoid such saturation.

The two modes which occur exclusively in Sb:ZnO are also present at $533.4\ \mathrm{cm}^{-1}$ and $684.5\ \mathrm{cm}^{-1}$ and correlate in intensity throughout the series. The

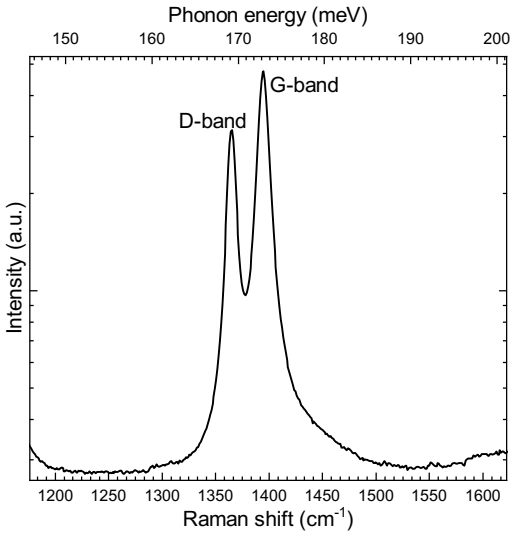

Fig. 4.23.: Modes of carbon doping at higher frequencies of the medium doped sample

mode at $533.4\ \mathrm{cm}^{-1}$ however is broader and is in close proximity to the $2B_1^{low}$ while the mode at $684.5\ \mathrm{cm}^{-1}$ is isolated from other possible modes.

There are also two unidentified peaks at $471.8\ \mathrm{cm}^{-1}$ and $675.9\ \mathrm{cm}^{-1}$. The first peak is also visible in the nominal undoped sample (black) as well as in a lower doped sample (blue). The latter peak occurs in the shoulder of the $684.5\ \mathrm{cm}^{-1}$ Sb exclusive mode and correlates in intensity with it. In addition to the appearance of carbon related Z-lines in PL also carbon related bands are present at higher phonon energies as shown in figure 4.23 for the medium doped sample. The D band at $1365\ \mathrm{cm}^{-1}$ as well as the G-band at $1394\ \mathrm{cm}^{-1}$ confirms the incorporation of carbon.

The mode's intensity is not a suitable reference in the series to identify whether more Sb has been incorporated between different samples due to possible changes in geometry or statistical changes due to the different amount of nanowires contributing to the measurement. However, if these effects can be excluded the comparison of the intensity of a single nanowire can be reliable. The appearance of Sb-related modes in the ZnO nanowires especially the ones which appear exclusively in Sb:ZnO can be used to determine whether the incorporation of Sb increases towards the tip of the nanowire. For sufficient lateral resolution tip-enhanced Raman spectroscopy (TERS) has been performed.

4.5.2 Spatial analysis of local vibrational modes

In the tip-enhanced Raman spectroscopy (TERS) setup an atomic force microscope (AFM) is combined with a regular Raman setup as described in more detail in section 3.3.5. Its advantages is on the one hand the enhancement of the Raman signal by a plasmonic interaction of the sample with the gold tip of the AFM and on the other hand an increased lateral resolution. Nanowires of the medium doped sample have been dispersed on a $\mathrm{Si0_2}$ substrate and mapped by AFM. After that, a linescan on an individual nanowire was made. Figure 4.24 shows the AFM image in an inset as well as the respective spectra at the particular locations.

The spectra show again the ZnO host modes, as well as additional modes at $275\ \mathrm{cm}^{-1}$, $676\ \mathrm{cm}^{-1}$, and only one of the exclusively Sb-related modes at $685\ \mathrm{cm}^{-1}$. The experiment on the dispersed nanowire has a different geometry than the regular Raman spectroscopy on the as-grown samples since the nanowires is laying flat on the substrate. In addition, it cannot trivially be assumed that the plasmonic interaction follows the same selection rules as the regular Raman scattering.

To reduce the influence of the geometry and to make the intensities more comparable all mode intensities have been normalized by the E_2^{high} mode, which is still the dominating peak in all spectra and allowed in all back-scattering geometries. The change in intensity has then been normalized as well by the value of each individual

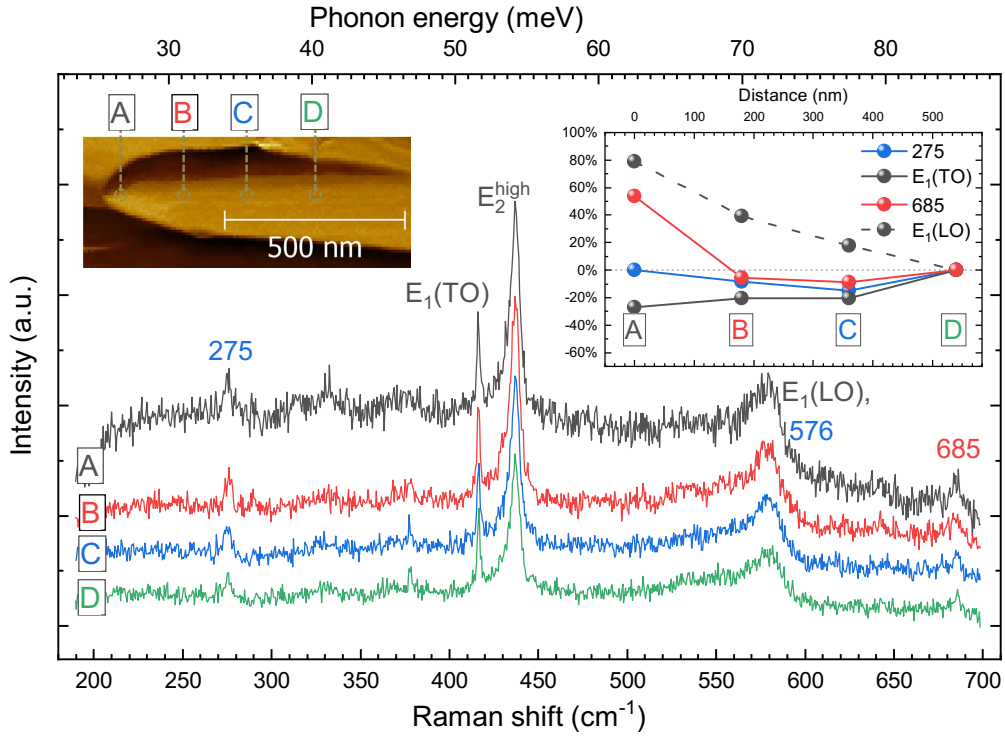

Fig. 4.24.: Tip-enhanced Raman spectroscopy (TERS) of a single nanowire

mode for the spectrum furthest away from the tip (point D) and displayed in the inset.

The $E_1(TO)$ and $E_1(LO)$ show an opposite trend towards the tip. This could be related to a change in the geometry or by the underlying Sb-related local mode at $576\ \mathrm{cm}^{-1}$. The also not exclusively Sb-related local vibrational mode at $275\ \mathrm{cm}^{-1}$ remains almost constant in the linescan with a variation of less than $20\ \%$. The exclusively Sb-related mode at $685\ \mathrm{cm}^{-1}$ follows this trend as well but increases drastically by almost $60\ \%$ at the last point at the tip. This sudden increase at the tip supports the assessment of a higher Sb incorporation at the tip.

4.6 Conclusion

The investigated MOVPE-grown ZnO nanowires had an average diameter of $200\ \mathrm{nm}$ to $600\ \mathrm{nm}$ and an average length of $1\ \mu\mathrm{m}$ and $3\ \mu\mathrm{m}$ with a characteristic cone shape tip revealed by secondary electron microscopy (SEM). In low temperature photoluminescence (PL) spectroscopy the near-band edge predominates the emission with the neutral donor-bound exciton I_8 (Ga) and a new transition I_{Sb} at $3.364(2)\ \mathrm{eV}$. Temperature-dependent PL measurements show a comparable behavior of I_{Sb} to I_8 with an almost constant localization energy (E_{loc}) of $12\ \mathrm{meV}$ and activation energy

(E_{act}) of 13.2 meV. This thermalization behavior suggests that I_{Sb} is not an excited state such as an exciton bound to an ionized donor/acceptor (D^+X/A^+X) or a rotational/vibrational state of a different impurity but rather a bound exciton in a ground state such a neutral donor/acceptor bound exciton (D^0X/A^0X). The similarity to I_8 continues also for the PL measurements under the influence of an external magnetic field. The determined g-factor for g_e, $g_h^{\parallel}$, and $g_h^{\perp}$ for $I_{Sb}$with 1.93, -1.25, and 0.11 respectively are consistent with the values of other D^0X and imply that the involved exciton is an A-exciton with Γ_7-symmetry for its electron and hole. The equivalent thermalization behavior at 5 T of the inner and outer Zeeman pair in the Voigt configuration confirms the assessment that I_{Sb} is a neutral donor-bound exciton (D^0X) and not a neutral acceptor-bound exciton (A^0X).

In μ-PL the spectrum of a single nanowire shows a similar spectrum as for an ensemble of nanowires but a screening effect can be observed for higher excitation powers. The mapped intensity for different nanowires showed an inhomogeneous lateral distribution of the PL emission. To increase lateral resolution and to avoid the excitation of peripheral nanowires cathodoluminescence (CL) and scanning transmission electron microscopy CL (STEM-CL) have been performed on single nanowires. The medium doped nanowire show an increased luminescence at the tip of two magnitudes whereas the undoped nanowire show only a slight linear increase towards the tip. Since both are comparable in shape and size a pure volume or surface effect can be excluded.

The Raman spectrum shows additional modes which could be identified with local vibrational modes caused by the doping. Besides local vibrational modes which occur in a variety of different dopants such as N, Fe, Al, Ga, Li, and Sb, also two modes at 533.4 cm^{-1} and 684.5 cm^{-1} are present which were reported exclusively for Sb doped ZnO. A linescan of a single nanowire with tip-enhanced Raman spectroscopy (TERS) show besides ZnO host modes and a non-exclusive local vibrational mode at 275 cm^{-1} also one of the exclusively Sb local vibrational modes at 685 cm^{-1}. Normalized by the E_2^{high} ZnO host mode the Sb mode shows a drastic increase of up to 60 % at the tip compared to a location approximately 500 nm away from where the other local vibrational mode at 275 cm^{-1} remains almost constant in intensity. A higher incorporation of Sb at the tip is the most likely explanation for the increase of PL and CL emission at the tip while in addition also the exclusively Sb-related local vibrational mode increases.

5 Antimony, carbon, and the effect of hydrogen co-doping

The prior chapter focuses entirely on antimony (Sb) doped ZnO nanowires and on the newly observed bound exciton state I_{Sb} to determine whether the Sb-related new impurity state acts as a donor or acceptor and the spatial origin of the luminescence. In the high resolution photoluminescence measurement, however, additional lines appeared between the I_8 and the I_{Sb} line labeled as Z-lines. Similar multiple lines have been reported before in this region labeled as X-lines [70], although the exact spectral position is different. Raman spectroscopy show the characteristic D and G band at $1356\ \mathrm{cm}^{-1}$ and $1598\ \mathrm{cm}^{-1}$ respectively in the Sb-doped samples indicating the additional incorporation of carbon into the sample. Carbon as unintentional impurity could also be the cause for the appearance of the Z-lines. In addition, Choi et al. [85] observed a reduction in photoluminescence (PL) intensity of C-doped ZnO thin film grown by pulsed laser deposition (PLD) compared to undoped film and concluded that carbon increases non-radiative recombination centers.
The first section of this chapter focus on Sb-doped ZnO nanowires which were co-doped with hydrogen in an attempt to avoid or reduce the incorporation of carbon. The second section shows the reversed scenario of intentionally carbon doped, as well as carbon and hydrogen co-doped ZnO nanowires.

5.1 Antimony and hydrogen co-doped zinc oxide nanowires

By doping with Sb a new transition occurred at $3.3642\ \mathrm{eV}$ which can be attributed to a Sb-related neutral donor state (D^0X) based on PL measurements with an external magnetic field. Besides the incorporation of Sb also traces of carbon are present. In PL up to four distinct peaks can be observed between the I_8 line (Ga related) and the new Sb-line. In Raman the characteristic D and G-band also indicate the incorporation of carbon and have been attributed to Sp^2 carbon clusters [86]. The origin of the carbon which leads to the unintentional doping might be the Sb-source trimethylantimony (TMSb - $(\mathrm{CH}_3)_3\mathrm{Sb}$) itself and could be a cause for a decreased PL intensity. To prevent or reduce the incorporation of carbon during the growth

hydrogen was introduced into the growth chamber. In a first attempt with a low flow rate of 20 sccm of hydrogen gas a substantial increase of the Sb-line intensity could be archived making the Sb-line the dominant line within the PL spectrum [87]. In this case, no hydrogen related line could be observed. The following analyzed sample had an even higher nominal hydrogen flow rate of 50 sccm.

5.1.1 Morphology

Figure 5.1 shows the morphology by SEM of the Sb and H co-doped nanowires with a low and high flow rate of hydrogen gas. In the case of a low hydrogen flux the shape is similar to the purely Sb-doped nanowires (figure 4.2 a)) with an increase of the diameter towards the tip and an cone-shaped tip. For the case of the high hydrogen flux (figure 4.2 b)) the characteristic nanowire form is heavily distorted and shows an inhomogeneous size distribution. While tips are still visible the cone shape changed to step or terrace-like structures.

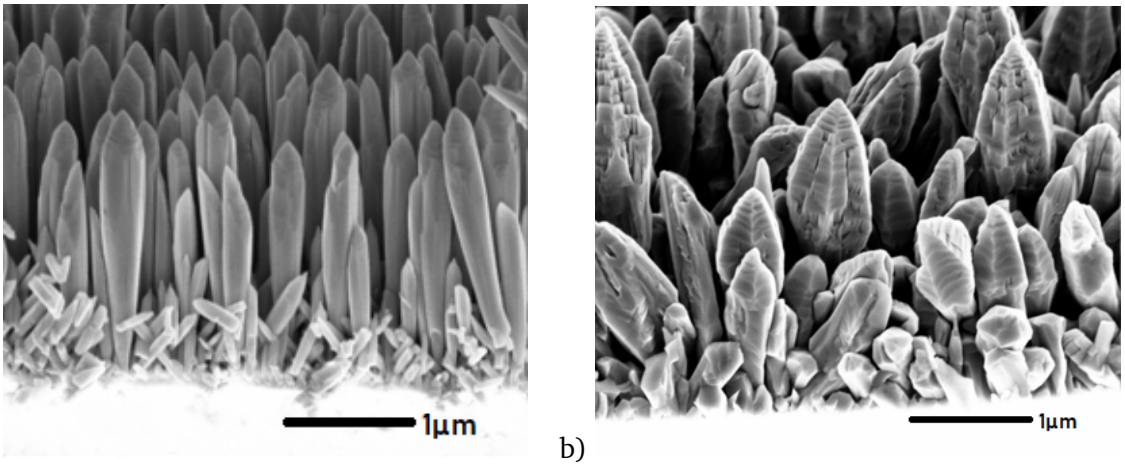

a) b)

Fig. 5.1.: SEM image of Sb-doped ZnO nanowires co-doped with hydrogen and a a) low hydrogen flux (20 sccm) and b) high hydrogen flux (50 sccm).

5.1.2 Optical properties

Although this heavy morphological distortion occurs the PL and reflectance spectra show similar properties at the near-band edge (NBE) with narrow lines (see figure 5.2). As in the case of low hydrogen co-doping the I_{Sb} is now the dominant line in the PL spectrum.

Besides the already identified lines both samples show traces of indium with a D^0X-transition (I_9), gallium (I_8) and it corresponding D^+X-transition (I_1), and the D^0X-transition (I_7) with its D^+X-transition (I_0) of unknown chemical origin.

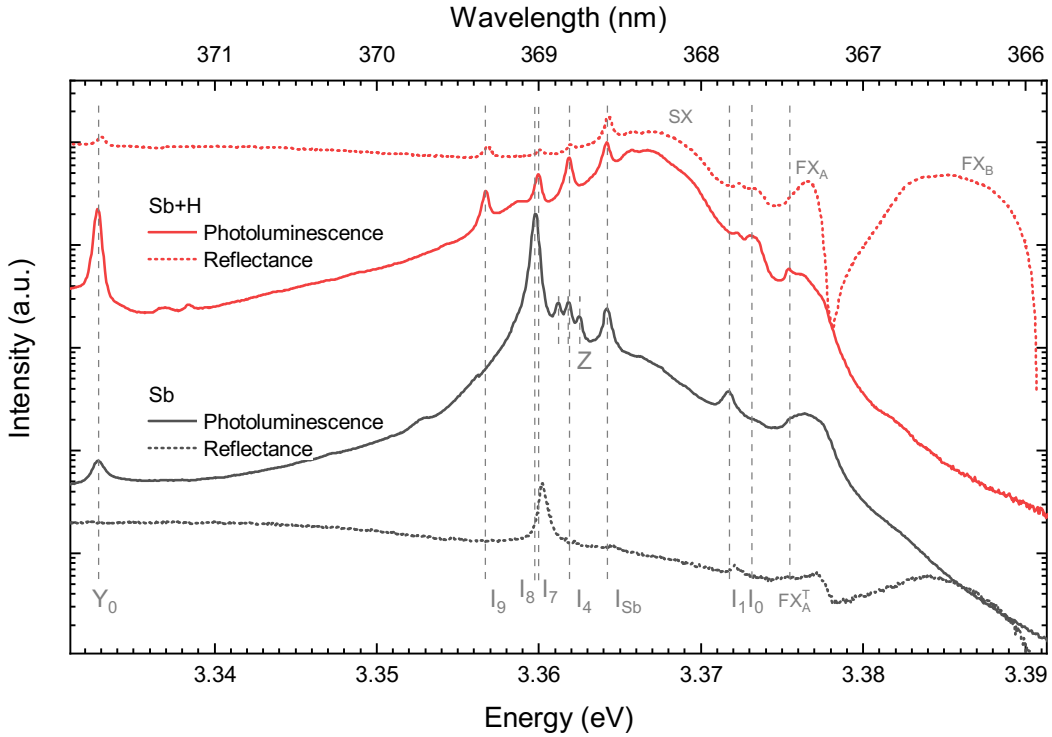

Fig. 5.2.: High resolution photoluminescence and reflectance spectra focused on the NBE emission of ensemble Sb-doped (black) and Sb and hydrogen co-doped (red) nanowires at 5 K from 3.30 eV to 3.39 eV.

Again this is predominately due to a memory effect of the reactor of prior growths. The more pronounced surface-bound-exciton (SX) of the co-doped sample could be the result of a different surface property of the sample. In general, all analyzed Sb-doped ZnO nanowires including the prior discussed in chapter 4 show a decrease of the SX over time may be due to a surface passivation. A more pronounced SX is hence an indicator for a younger sample or one with less passivation. There are no Z-lines in the co-doped sample as described for a comparable sample with a low hydrogen flux [87]. Instead, the I_4-line at 3.3621 eV, which is attributed to hydrogen [66, 88], appears energetically between the I_8 and I_{Sb}-line.

If we consider the temperature dependent PL behavior (see figure 5.3) the carbon related Z-lines observed in the purely Sb doped samples cannot be confused with the I_4-line in the co-doped sample. The identified Z-lines (see figure 4.6) usually quench at temperatures at around 40 K whereas the I_4-line is still visible at temperatures of up to 100 K. The $I4$-line is an exciton bound to a hydrogen donor level where the hydrogen occupies an oxygen place (H_O) and is reported to be thermally unstable and can be annealed out with temperatures above 500°C.[89]. Another donor level can be formed if hydrogen is bound on a bond-centered lattice (H_{BC}) site and a bound exciton transition can be seen in PL at 3.3601 eV [90]. No such line has been

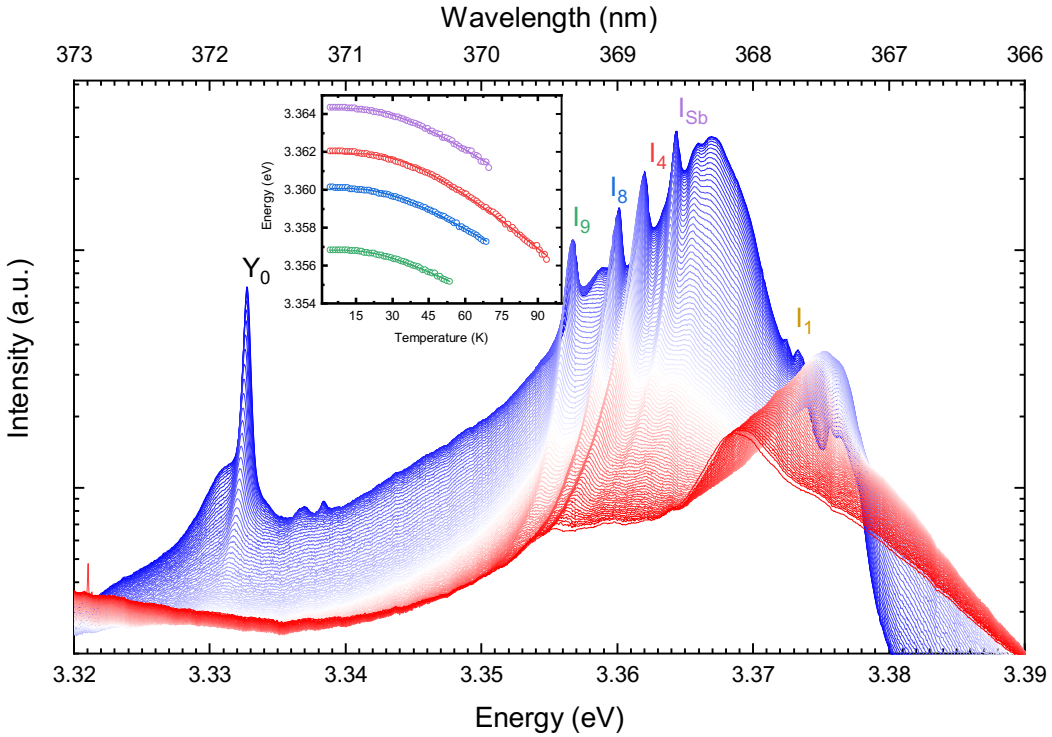

Fig. 5.3.: High resolution photoluminescence spectra focused on the NBE emission of ensemble Sb and H-codoped nanowires (temperature series). Low (blue) to high (red) temperatures between 4.6 K and 90.0 K. The inset represents the peak shift in temperature fitted with a model by Viña [71].

observed in this sample although this expected peak would be in close proximity to the I_8-line.

5.1.3 Raman spectroscopy

In Raman spectroscopy no hydrogen related additional line which can be expected at $742\ \mathrm{cm} - 1$ [88] appeared (see figure 5.4). The reported characteristic vibrational mode for $\mathrm{H_{BC}}$ at $330\ \mathrm{cm}^{-1}$ if present might be covered by the $E_2^{high} - E_2^{low}$ mix-mode. To compare the Raman intensities of the D and G-band both spectra have been normalized to the E_2^{high}-mode and a common baseline. Even though also the Sb and hydrogen co-doped nanowires indicate a D and G-band and hence still incorporate amounts of carbon the quantity is considerably lower (please note the logarithmic intensity scale) if considering the reduction of the D and G-band.

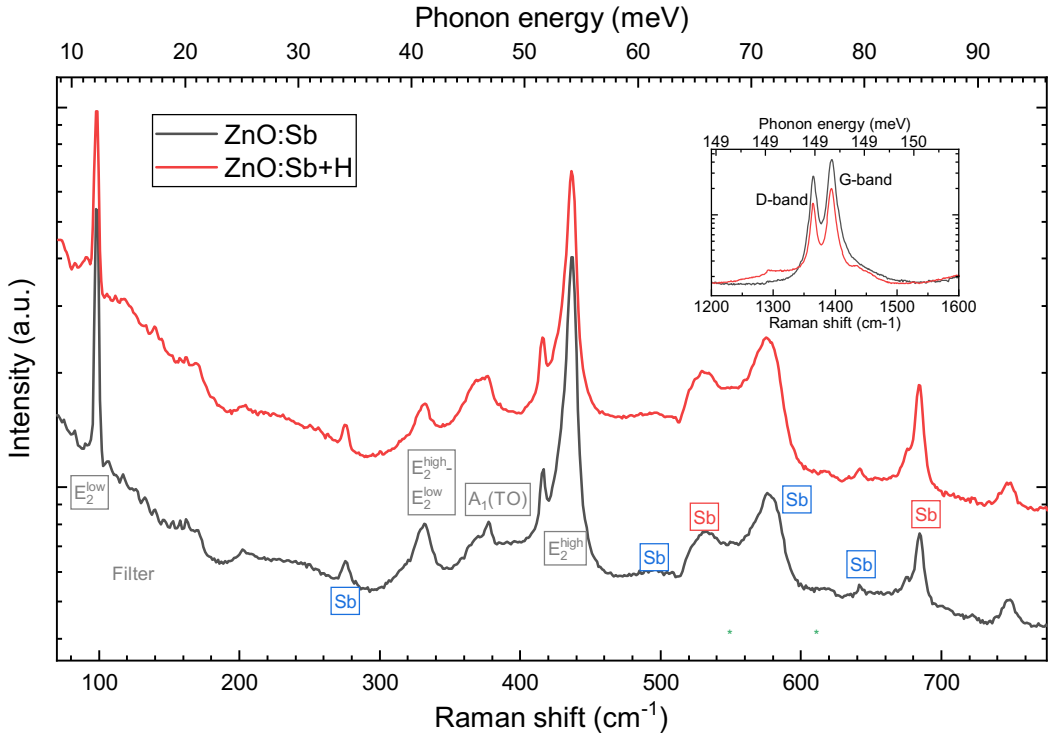

Fig. 5.4.: Comparison of the Raman spectrum of Sb doped (black) and Sb and H co-doped ZnO (red) nanowires.

5.1.4 Conclusion

In conclusion, the co-doping with hydrogen gas during the growth of Sb-doped ZnO nanowires enhanced the PL intensity of the Sb-Line for low and high hydrogen flux rates. The morphology however changed drastically for the high hydrogen flux. In PL a distinct $I4$-line appears for high hydrogen flux rates which is evidence for the incorporation of hydrogen (H_O). The prior observed Z-lines are missing. Although the PL lacks evidence of carbon-related transitions in the Raman spectrum the distinct D and G bands are still present although considerably lower than in the sample without hydrogen co-doping. It is most likely that the co-doping with hydrogen removes not entirely the incorporation but a specific form of a carbon complex which reduces the spectral performance of the Sb-doping and reduces the concentration of non-radiative recombination. In addition, also a more pronounced surface-bound-exciton could be observed.

5.2 Carbon doped and hydrogen co-doped nanowires

In the above discussed samples grown by metalorganic vapor-phase epitaxy (MOVPE) carbon impurities in the resulting ZnO crystal are usually unavoidable since carbon is

always present in the used metalorganic precursors such as the Zn source dimethylzinc (DMZn - $(CH_3)_2Zn$) or the precursor for the dopants such as trimethylantimony (TMSb - $(CH_3)_3Sb$) for the Sb doping and hence carbon is always present in the reactor. As a group IV element carbon can act as a double donor for n-type conductivity [85, 91], double acceptor for p-type conductivity, as a complex with other dopants or form clusters (i.e. carbon-oxygen-cluster [92]). Especially in the attempt to form p-type ZnO doped with nitrogen the formation of carbon related complexes can yield a compensation [93, 94, 95] due to their lower formation energy [96]. To identify the carbon related properties, intentional carbon doped ZnO nanowires were grown in MOVPE with a dilute mixture of carbon tetrachloride (CCl_4) gas in nitrogen (1000 ppm) as carbon source and carbon co-doped with hydrogen nanowires by adding a small amount of hydrogen gas. The hydrogen gas flow was changed to analyze the effect of a co-doped sample with a high (50 sccm) and low (2 sccm) flow rate of hydrogen.

5.2.1 Morphology

In Figure 5.5 the morphology of a) undoped, b) carbon doped, and c) carbon and hydrogen co-doped ZnO nanowires are shown.

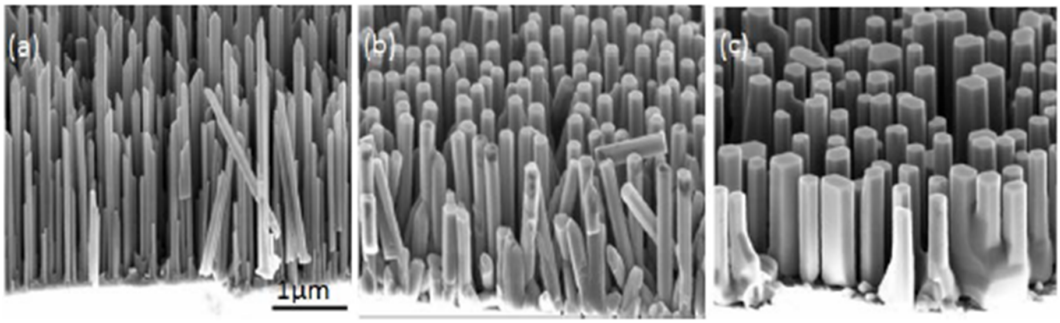

Fig. 5.5.: Secondary-electron microscope (SEM) image of ZnO nanowires a) undoped, b) carbon doped, and c) carbon hydrogen co-doped. [97]

The nanowires have a length of approximately $2-3$ μm and a diameter of approximately 200 nm. The tips have a hexagonal flat shape in contrast to the cone-shaped Sb-doped nanowires (see figure 4.2) and the nanowires are aligned along the c-axis. The nanowires which were co-doped with hydrogen have an increased diameter. Some nanowires coalescent with their neighbors due to an increased growth rate along the side facets $\{\bar{1}100\}$ and $\{01\bar{1}0\}$ compared to the c-axis $[0001]$ since the nanowires coalescent along with their whole length and not only at the tip which could be caused by electrostatic interactions [98].

5.2.2 Optical properties

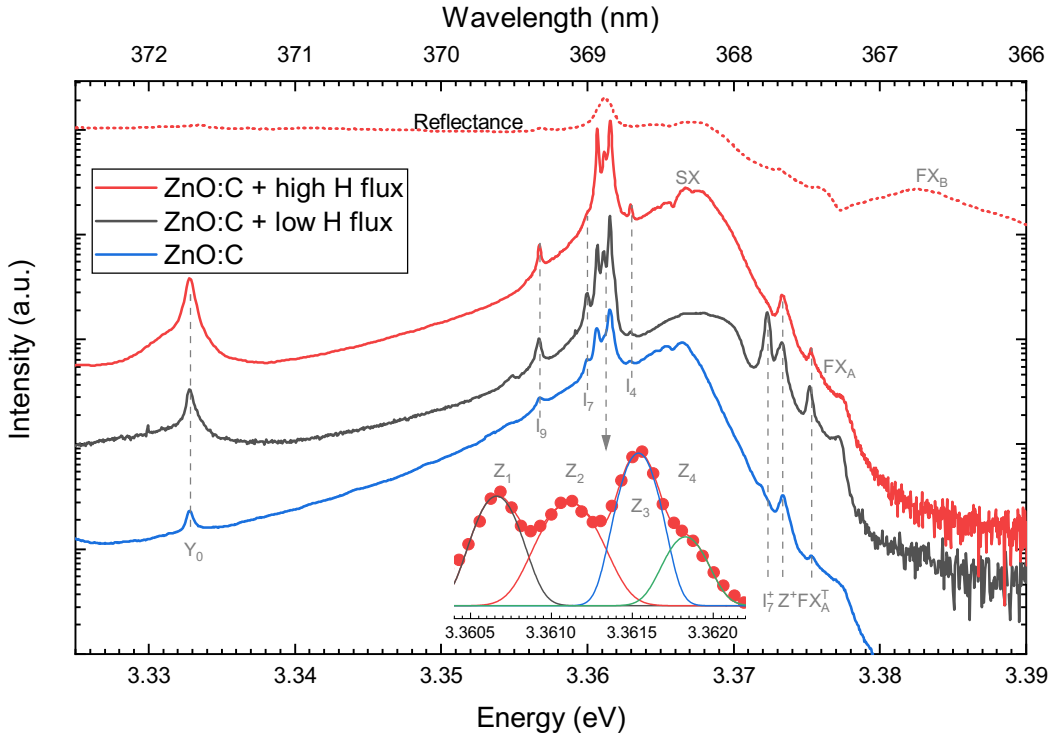

Fig. 5.6.: High resolution photoluminescence and reflectance spectra of ensemble C-doped (blue), C+H co-doped nanowires with low (black) and high (red) hydrogen concentration. The inset shows a close-up of the Z-lines fitted with four Gaussian peaks.

Figure 5.6 shows the photoluminescence spectra of the near-band-edge (NBE) of C-doped and C and H co-doped ZnO nanowires with different H flow rates during the growth at 5 K. Besides the already identified peaks of Y_0, I_9 (indium), I_7, I_4 (hydrogen), I_0 (I_7^+) (unknown chemical origin), surface bound exciton (SX), and free A-exciton (FX_A) four additional lines appear in the all C-doped samples between the I_7 and I_4-lines, here denoted as Z_{1-4}. A close-up for this region is shown in the inset with four Gaussian fits to determine the spectral positions, where Z_{1-4} is at 3.3606 eV, 3.3611 eV, 3.3615 eV, and 3.3618 eV respectively. In addition, a broader peak appears at $3.373 - 3.374$ eV for all three samples and scales with the Z_{1-4} lines and is hence likely the corresponding ionized bound states, labeled as Z_{1-4}^+. The H co-doped samples show an overall higher intensity not only for the Z-lines but also for the other lines compared to the only C-doped sample. The differences between the low and high H co-doped sample are minor but it should be noted that I_7 and I_7^+ is more pronounced in the low H co-doped sample.

5.2.3 Excited states

In photoluminescence excitation spectroscopy (PLE) individual excitation channels for distinct lines can be analyzed. In the following, the C and H co-doped sample with a high H flux has been analyzed. In figure 5.7 all photoluminescence spectra with different excitation power are stacked vertically and plotted as a contour plot. The PLE spectra are therefore lined up horizontally.

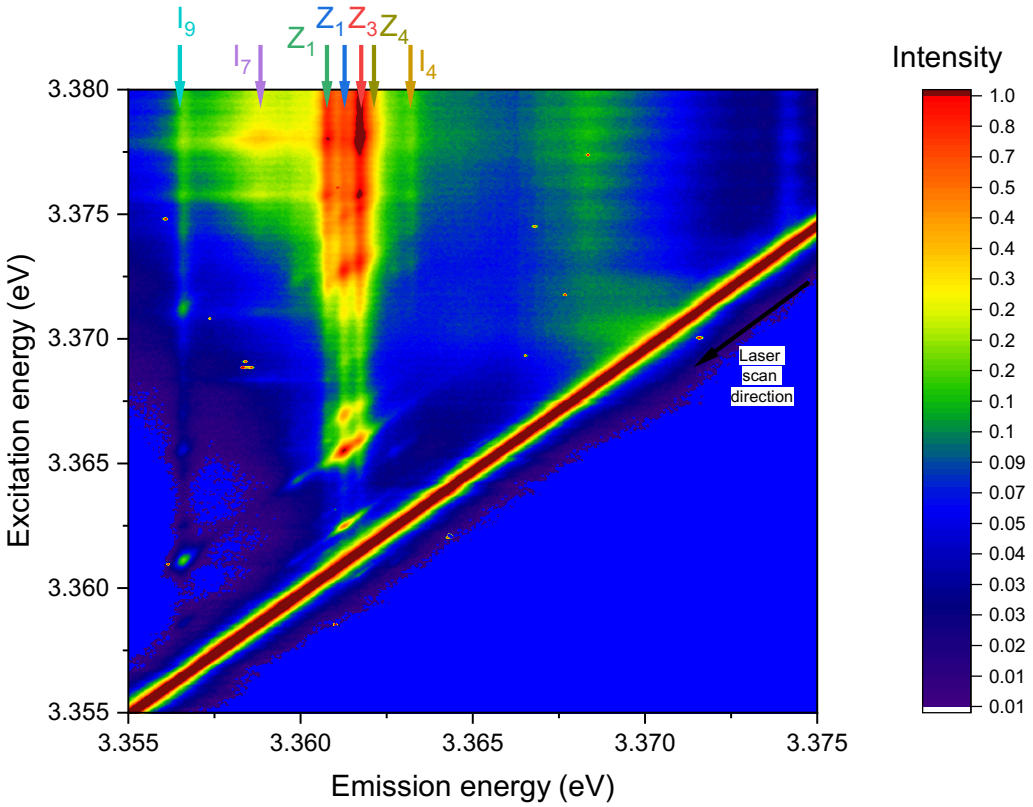

Fig. 5.7.: Photoluminescence excitation (PLE) of C and H (high flux rate) co-doped ZnO nanowires. The contour plot shows all PL spectra with varying excitation energy.

In the higher energy region above the SX, especially in the ionized donor (D^+X) region no individual transition can be identified. This is likely due to the nature of the pulsed excitation laser and hence the in general higher excitation energy. This high excitation results in more free charges carrier and a screening effect, as discussed in chapter 4.3.3. The individual PLE spectra for the labeled lines are shown in figure 5.8.

In the PLE spectra, distinct excitation channels can be identified and are labeled with integers. In addition, all considered lines have a distinct enhanced intensity when excited via the free A-exciton. The absolute and relative energetic positions of these excitation channels are summarized in table 5.1.

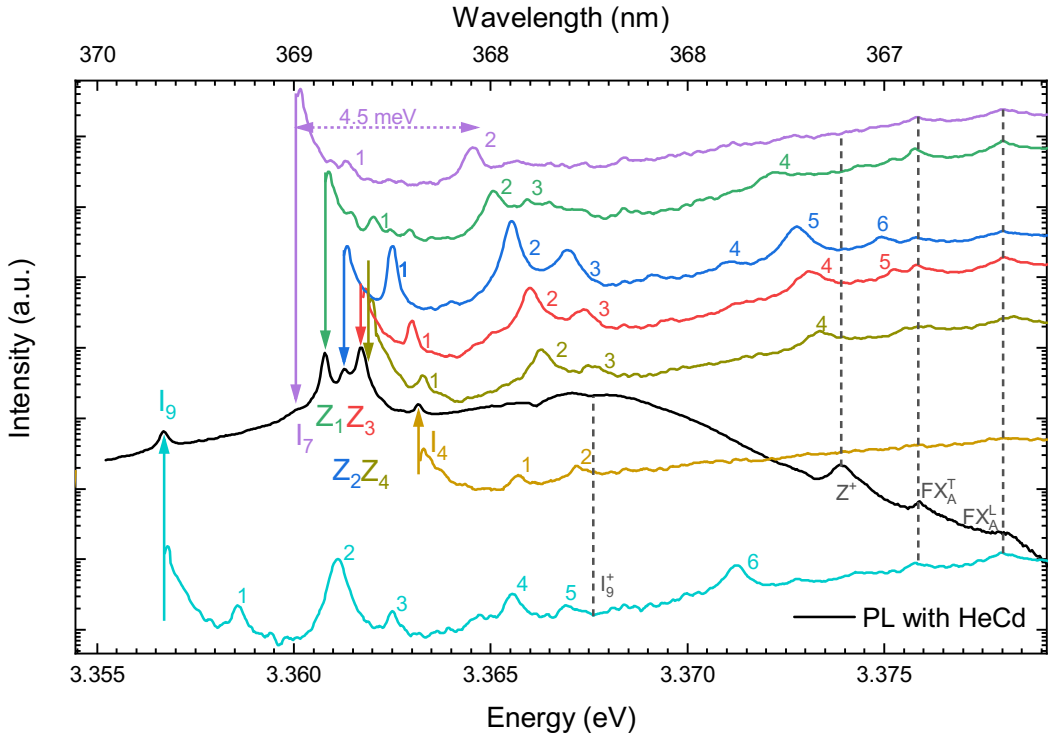

Fig. 5.8.: Photoluminescence excitation (PLE) profiles of C and H (high flux rate) co-doped ZnO nanowires. The PL spectrum (black) is a reference excited with a He-Cd-laser.

Tab. 5.1.: Absolute and relative Positions of the peaks found in the PLE spectrum of C and H (high flux rate) co-doped nanowires

		0	1	2	3	4	5	6
I_9	Pos. (eV)	3.3567	3.3586	3.3611	3.3625	3.3656	3.3669	3.3712
	Δ (meV)		1.9	4.4	5.8	8.9	10.2	
I_7	Pos. (eV)	3.3601	3.3613	3.3646				
	Δ (meV)		1.2	4.5				
Z_1	Pos. (eV)	3.3608	3.3621	3.3651	3.3662	3.3721		
	Δ (meV)		1.3	4.3	5.4	11.3		
Z_2	Pos. (eV)	3.3613	3.3625	3.3655	3.3669	3.3728	3.3749	
	Δ (meV)		1.2	4.2	5.6	11.5	13.6	
Z_3	Pos. (eV)	3.3617	3.3630	3.3660	3.3674	3.3731	3.3753	
	Δ (meV)		1.3	4.3	5.7	11.4	13.6	
Z_4	Pos. (eV)	3.3619	3.3633	3.3662	3.3675	3.3734		
	Δ (meV)		1.4	4.3	5.6	11.5		
I_4	Pos. (eV)	3.3632	3.3657	3.3672				
	Δ (meV)		2.5	4.0				

All lines show a higher intensity when excited approximately 4.5 meV above the ground state. These exciton transitions involve a hole from the B-valence band rather than from the A-valence band [80, 81]. The closest excitation channel 1 for all lines with 1.3 meV above the ground states matches the longitudinal-transverse

splitting of the A-exciton. Unfortunately, no higher intensity could be measured at the spectral position of Z_{1-4}^{+} which could be used to identify the corresponding ionized donor bound transition for each Z-line. For comparison, there is also no higher intensity for I_9 at the nominal excitation energy of its ionized donor bound transition (D^+X) at $3.3676\ \mathrm{meV}$. Again this is likely due to the high screening effect of the laser which prevents a clear identification.

5.2.4 Magneto-optical properties

Similar to chapter 4.3.1 about the Sb-doped ZnO nanowires photoluminescence measurements with an additional external magnetic field can further reveal the nature of the underlying transitions of the Z-lines utilizing the Zeeman effect. In the following the C and H co-doped sample with the low H flux rate is analyzed. The method of the magneto-optical measurement is explained in chapter 3.2.3. The sample was mounted in a bath cryostat with a superconducting split coil and a magnetic field with a strength up to $5\ \mathrm{T}$ was applied in the two main geometric configuration Voigt ($B \perp c$) and Faraday ($B \parallel c$). In addition, it was turned with an arbitrary angle between these two configurations at $5\ \mathrm{T}$. Figure 5.9 shows single spectra for the two configurations and increasing magnetic field strength as well as the angle-dependent spectra in the range from the neutral donor bound region (D^0X) with the I_9 line to the ionized donor bound region (D^+X) and the free A-exciton.

The splitting for the D^0X transitions (e.g. I_9) is smaller in the Faraday than in the Voigt configuration. To show the polarization dependency of the lines in the Faraday configuration the red (black) dotted line at $5\ \mathrm{T}$ shows the σ^- (σ^+) circular polarization of the lower (higher) component of the split lines. In the energetically higher D^+X region no splitting is visible but the rise of an additional prior forbidden component. In direct comparison between the D^0X and D^+X-region especially in the Voigt configuration the Z-lines split with the increase of magnetic field strength indicating a D^0X behavior. For higher magnetic fields the individual split peaks merge with their neighbors. The angle-dependent measurement start in the Faraday configuration ($\theta = 0°$) at $5\ \mathrm{T}$ and then rotate the sample to change the angle between B and c. Due to the 4-fold splitting in the mixed geometry where also $E \parallel c$ components become allowed the number of peaks increases even further. Since the magnetic field has been changed continuously figure 5.10 shows the trend of the Z-lines for each geometry in a contour plot as well as for the I_7.

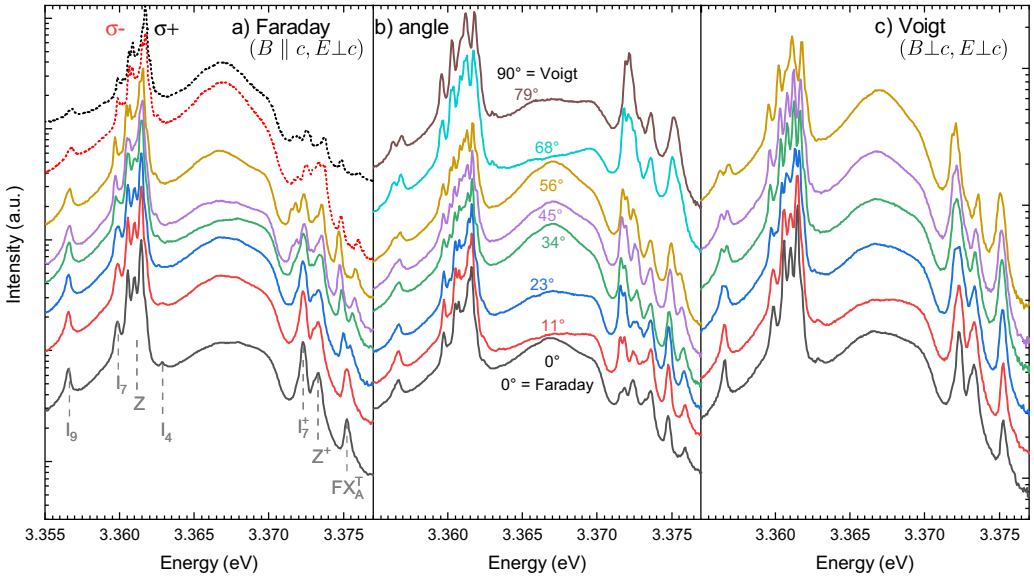

Fig. 5.9.: Photoluminescence spectra for different magnetic fields of C and H co-doped ZnO nanowires a) Faraday configuration ($B \parallel c$). b) angle between B and c at 5 T c) Voigt configuration ($B \perp c$)

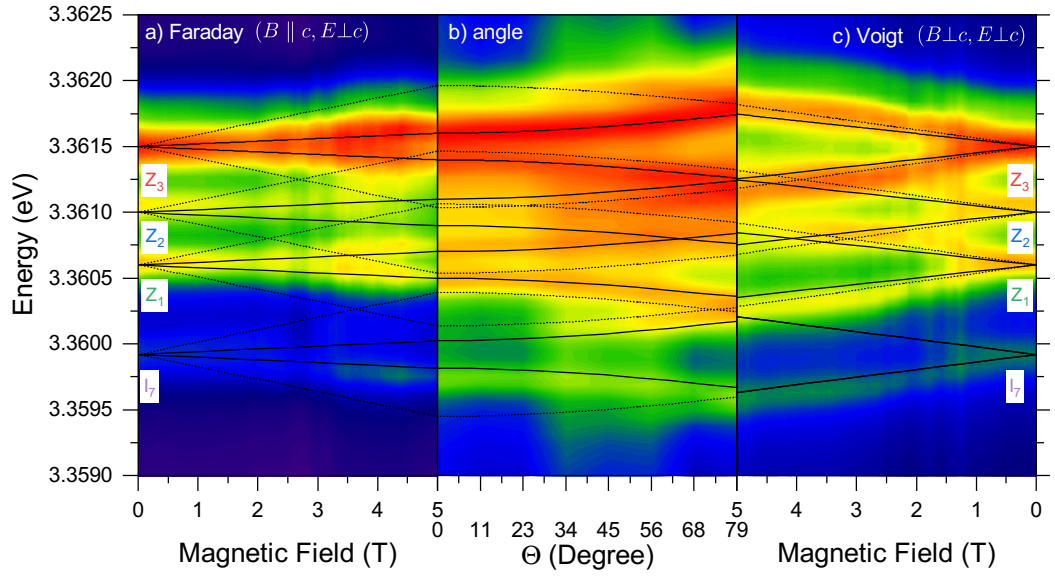

Fig. 5.10.: Contour plot of the Zeeman splitting of the Z-lines of C and H co-doped ZnO. Solid (dotted) lines represent the splitting of the inner (outer) branches based on the g-factors determined for Z_3 for all Z-lines.

In the contour plot, the crossing of the individual lines in the Voigt configuration is clearly traceable. To determine the electron and hole g-factor the angle-dependent measurement is important since all g-factors contribute. Due to the close proximity of the lines only the 4-fold splitting for the most intense line Z_3 could be traced and fitted with Lorentzians. Based on these values the g-factor are determined with

equation 3.7 as fit. The resulting fitting function was then added to the contour plot of each geometry with solid (dashed) line for the inner (outer) branches of the 4-fold Zeeman splitting. As a reference, the same values have been used for the other observed lines $Z_{1,2}$ to plot the Zeeman function into the contour plot. Although the g-factors have not been determined individually for each of the Z-line the Zeeman branches of the fit lie within the region of higher intensity which suggests that only minor deviation should be expected. For comparison, the 4-fold split of the I_7 was analyzed as well and fitted. The resulting g-factors are summarized in table 5.2.

Tab. 5.2.: Electron and hole g-factors for Z_3 and I_7.

Line	g_e	$g_h^{\parallel}$	$g_h^{\perp}$	Ref.
Z_3	1.95 ± 0.03	-1.25 ± 0.05	0.16 ± 0.13	this work
X_i	1.95	-1.57	0.13	[17, 78]
I_7	1.99 ± 0.03	-1.27 ± 0.04	0	this work

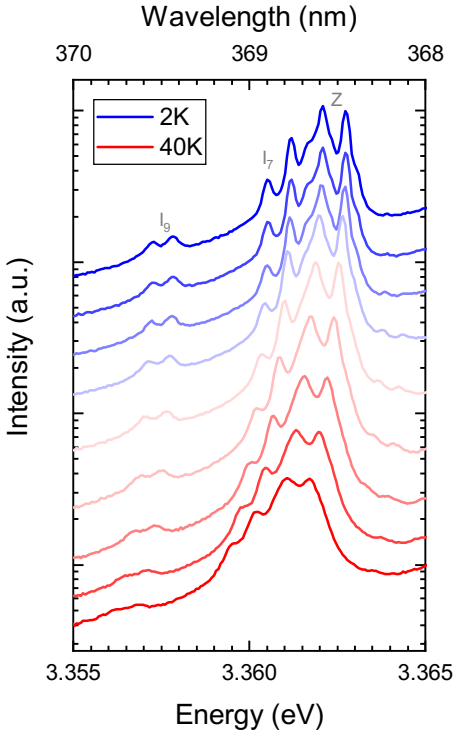

Fig. 5.11.: Thermalization of the Z-lines in the Voigt configuration at 5 T between 2 K and 40 K

The obtained values for the Z_3-line are similar to prior determined values for the X_i-lines, but with a higher value for the hole g-factor in parallel $g^{\parallel}$. For I_7 the gained value for $g_h^{\perp}$ in an initial fit was very small and hence set to 0.

The thermalization behavior of the individual components of the Zeemann branches in the Voigt configuration can reveal the nature of the impurity state whether it is an exciton bound to an acceptor or donor. Figure 5.11 shows the thermalization of the Z-lines in the Voigt configuration at $5\ \mathrm{T}$ between $2\ \mathrm{K}$ and $40\ \mathrm{K}$. All observed peaks shift with the increase of temperature due to the temperature change of the bands, the intensity decreases and the width increases. Although not all buried components of all Z-lines are individually resolved the overall behavior suggests a symmetric quench of the components as visible for the I_9. A final assessment is not possible based on the retrieved data but it is likely that the Z-lines are transitions based on an A-exciton bound to a neutral donor bound state.

5.2.5 Conclusion

The analyzed C-doped ZnO nanowires show a hexagonal shape with a flat top unlike the prior analyzed Sb-doped ZnO nanowires. By adding H gas during the growth the lateral growth dynamic increases and the nanowires start to coalescent. In photoluminescence the purely C-doped and the C and H co-doped ZnO nanowires individual Z-lines were observed at $3.3606\ \mathrm{eV}$, $3.3611\ \mathrm{eV}$, $3.3615\ \mathrm{eV}$, and $3.3618\ \mathrm{eV}$, as well as a broader peak in the region of the ionized donor bound excitons at $3.373 - 3.374\ \mathrm{eV}$, labeled as Z^+. The H co-doping increases the overall PL intensity of all lines already for a low H flux ($2\ \mathrm{sccm}$). With an even higher H flux ($50\ \mathrm{sccm}$) the H-related I_4 is visible in the PL spectrum. The I_7 and I_7^+ lines (unknown chemical origin) are only visible in the sample with low H flux. The increase of the overall PL intensity was also present in the Sb and H co-doped ZnO nanowires in chapter 5.1. Based on these experiments it is evident that H gas even with a low flux during the growth for these samples is beneficial and non-radiative recombination centers which reduce the PL performance decreases. In the Sb-doped nanowires the C-related Z-lines disappeared by co-doping with H but not for the C-doped samples. The exact origin of the non-radiative recombination centers, whether they are related to a specific C impurity or complex or not, as well as the mechanism how H reduces it contribution remains unknown.

In PLE no enhanced intensity of the Z-lines could be detected by the Z^+-peak, as well as for I_9 at the nominal I_9^+ spectral position. This is due to a screening effect of free charge carriers caused by the high excitation power of the pulsed laser. In magneto-optical measurements, the Z-lines split into individual Zeeman branches and show a behavior that can be excepted from a transition of an A-exciton bound to a neutral impurity state while the corresponding Z^+ peak shows no splitting and therefore a behavior expected from a transition of an exciton bound to an ionized

bound impurity. The close proximity of the Z-lines among themselves makes an individual study of the individual lines difficult. However, the electron and hole g-factors determined for Z_3 are good approximations for the other observed lines. The thermalization behavior indicates a symmetrical quench of the Zeeman branches suggesting that the underlying impurity is a donor but since not all branches could be observed individually this analysis is not final.

6 Exciton-polaritons in MBE grown ZnO

Exciton-polaritons are bosonic quasiparticles reflecting the strong coupling between photons and excitons. The result is a unique dispersion relation which has been described in chapter 2.3. The properties of exciton-polaritons have been studied for a variety of different materials, such as CdS [99] CdSe [100], GaAs [101, 102], CuCl [103, 104], ZnSe [105], and polymers [106]. Pekar [107], as well as Thomas and Hopfield [108] formulated a polariton theory about the exciton-photon-system already in the 1950s and 1960s. Today, the study of exciton-polaritons is a wide field in bulk, nanowires, quantum wells, and microcavities with many promising applications. [109] Especially the formation of Bose-Einstein-condensation [110] leads to new types of the exciton-polariton laser without the necessity of population inversion [111] and a much smaller laser threshold than in conventional laser [112]. Polariton lasers in GaN have already been reported for room temperature [113] and with electrical injection [114], as well as in GaAs [115].

Exciton-polaritons in ZnO have been studied with reflectance measurements [116, 117, 118, 21] and with photoluminescence (PL) spectroscopy [119]. For the latter case, a c-plane sample was investigated in cross-section to be able to investigate exciton-polaritons. In the so-called α-geometry with the normal incidence of light to the c-plane surface ($k \parallel c$) no exciton-polaritons can be expected. [21]

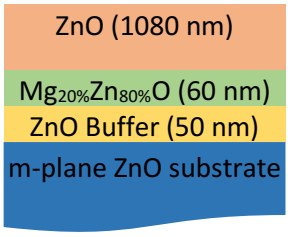

Fig. 6.1.: Structure of the MBE sample to investigate exciton-polaritons.

To be able to investigate exciton-polaritons in an optical experiment with normal incident a non-polar m-plane ZnO sample was produced at the Centre de Recherche sur l'Hétéro-Epitaxie et ses Applications (CRHEA) by Jean-Michel Chauveau using Molecular Beam Epitaxy (MBE). Figure 6.1 shows a sketch of the sample structure. The undoped ZnO layer on top has a thickness of 1080 nm, which matches the proposed critical thickness of 1 μm [118, 21]. To obtain a high crystalline quality with low defect densities the layer was homoepitaxially

grown on ZnO substrate with a buffer layer of 50 nm ZnO and a following layer of ZnMgO layer of 60 nm.

6.1 Exciton-polariton interferences

The sample was investigated in macro-PL with the setup described in chapter 3.2. To be able to differentiate between the two possible polarizations σ ($E \perp c$) and π ($E \parallel c$) a UV-grade analyzer was placed in front of the monochromator adjusted and fixed to the preferred polarization direction of the subsequent gratings. The linear components were then selected with a $\lambda/2$-plate in front of the analyzer. Figure 6.2 show the unpolarized PL spectrum (solid black) as well as the spectrum of the individual components (solid red and blue), and a reference spectrum of the ZnO substrate (dashed).

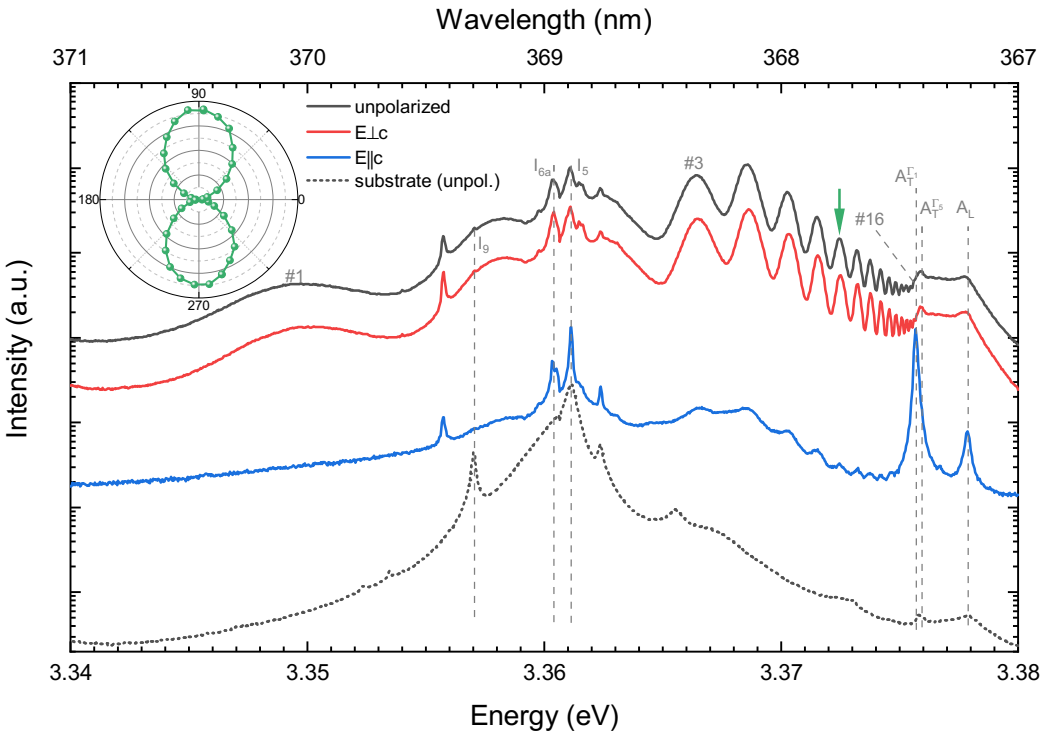

Fig. 6.2.: Photoluminescence spectrum with different polarizations of the MBE sample and the ZnO substrate as reference. The inset show the polarization dependency (angle between E and c) at the position marked with an arrow.

In the unpolarized spectrum, the components of the free A-exciton is visible at $A_T = 3.3759$ and $A_L = 3.3779$, as well as some peaks (i.e. I_{6a} and I_5) in the region of excitons bound to a neutral donor (D^0X). In addition, 16 additional waves (counted from the low energy side) appear, showing a Fabry-Pérot interference pattern. The pattern is σ-polarized and hence only visible for $E \perp c$. In the opposite

π-polarization the pattern is heavily suppressed and a fine structure of the free A-exciton is visible showing the Γ_1 rather than the Γ_5 component (see selection rules in table 2.1). The polarization dependency for one of the oscillations (marked with an arrow) is plotted in the inset as a function of the angle between E and c. In contrast, the ZnO substrate shows no interference pattern.

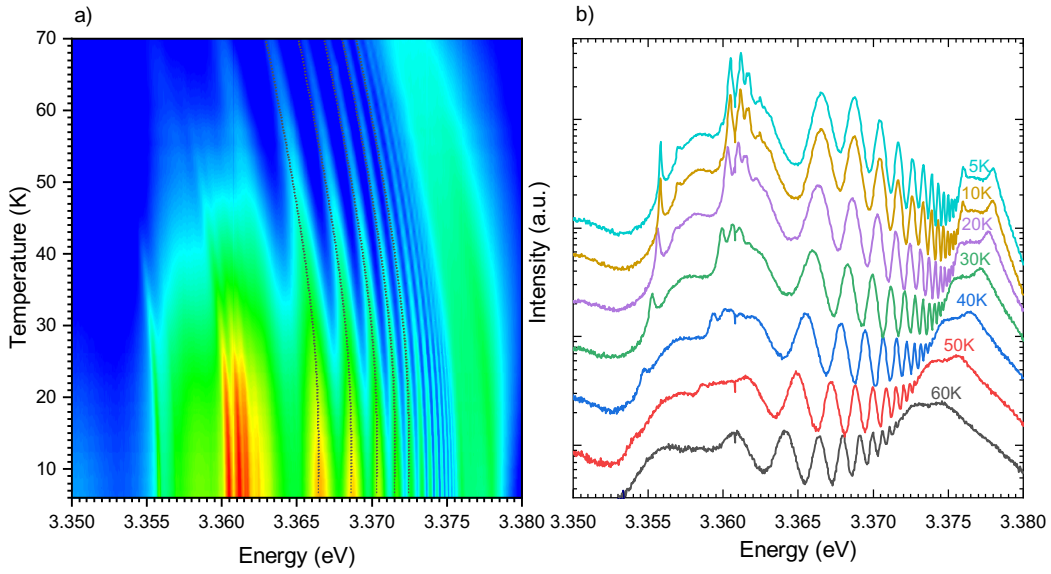

Fig. 6.3.: Temperature depended photoluminescence of the Fabry-Pérot interferences. a) Contour plot with all measurements. Dotted lines represent a fit based on the model by Viña. b) Single spectra for specific temperatures.

Figure 6.3 a) shows the temperature dependency of the PL spectrum between 5 K and 80 K as a contour plot. The free A-exciton has an expected red-shift in temperature and the Fabry-Pérot interference pattern follows this trend. As a reference, the shift was fitted by a model proposed by Viña et al. [71] with the parameters $\alpha = (12.4 \pm 0.5)$ meV/K and $\theta = (105 \pm 2)$ K (dotted lines). The donor bound excitons significantly begin to quench at temperatures of about 40 K while the interference pattern is visible well above 100 K. In figure 6.3 b) spectra are shown for individual temperatures. The free exciton becomes the dominant feature at elevated temperatures and broadens significantly. The interference pattern is not affected by a broadening. The visible number of oscillations reduces beginning from the high energy side.

Since most of the exciton-polariton interference patterns which have been observed in other materials have been analyzed by reflectance rather than PL measurements, figure 6.4 compares both measurements. The interference pattern is not only visible in PL but also in reflectance measurements again with a strong

polarization dependency. Unlike in PL where the interference pattern is only clearly visible energetically below the free A-exciton, in reflectance the pattern is extended between the B and C-exciton and above, again with an increasing frequency of oscillations closer to the exciton state. If compared to the reflectance spectrum also in PL small peaks can be identified (dotted lines) which corresponds to minima of the oscillations in the reflectance spectrum.

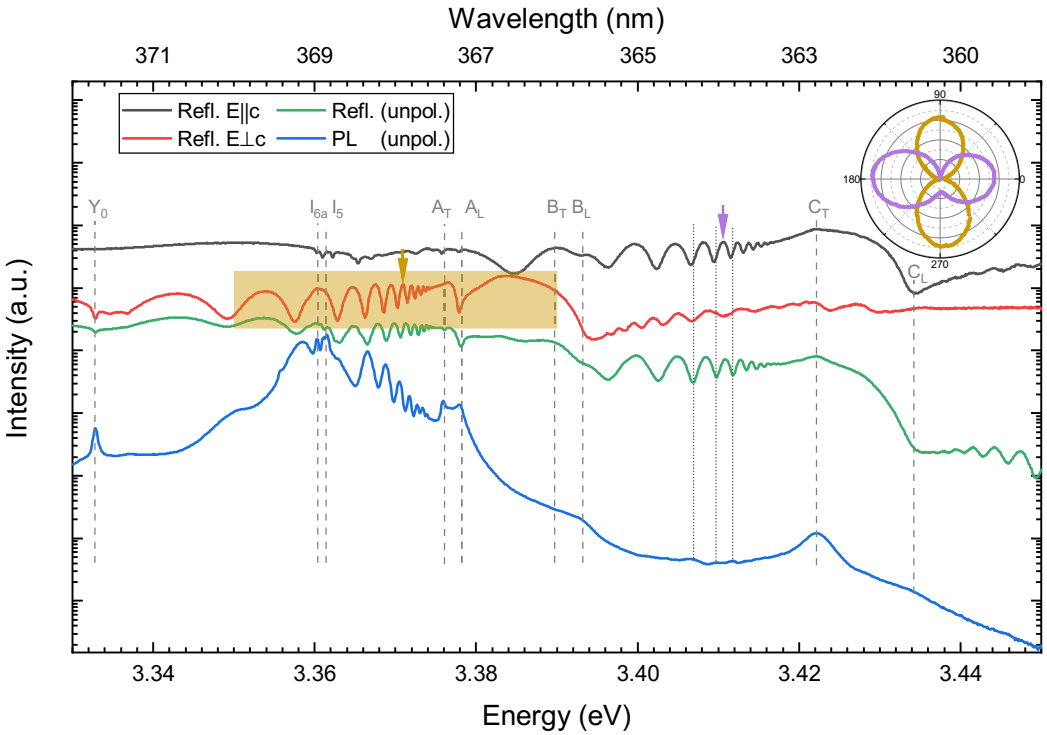

Fig. 6.4.: Photoluminescence and reflectance measurement for different polarizations. The inset show the polarization dependency (angle between E and c) at the position marked with an arrow. The marked area is further analyzed in chapter 6.3.

The polarization depended measurements reveal that the oscillations in the proximity of the C-exciton have the opposite polarization and are π-polarized were the oscillations near the A and B-excitons are σ-polarized. The interference patterns hence corresponds with the selection rules of the respective exciton state with the highest oscillator strength (see table 2.1). The polarization dependency of the intensity for different angles between E and c are plotted in the inset for the position energetically below the A-exciton and C-exciton respectively (position marked with an arrow).

The positions of the identified lines are summarized in table 6.1.

Tab. 6.1.: Position of the of the identified lines based on photoluminescence and reflectance measurements.

Line	Position (eV)	Reference
Y_0	3.332(9)	3.3328 [68]
I_{6a}	3.360(3)	3.3604 [66]
I_5	3.361(5)	3.3614 [66]
A_T	3.376(0)	3.3768 [120], 3.3759 [19]
A_L	3.378(1)	3.3778 [19]
ΔA_{LT} (meV)	2.1	1.9 [19], 2.7 [121], 2.0 [122]
B_T	3.384(5)	3.3834 [120], 3.816 [19]
B_L	3.393(2)	3.3929 [19]
ΔB_{LT} (meV)	8.7	11.3 [19], 10.6 [121],10.2 [122]
C_T	3.422(1)	3.4223 [120], 3.4209 [19]
C_L	3.434(2)	3.4327 [19]
ΔC_{LT} (meV)	12.1	11.8 [19], 12.1 [121], 11.0 [122]

6.2 Crystal orientation and quality based on Raman spectroscopy

The crystallographic orientation of the prior PL and reflectance measurements match the selection rules for the free excitons in ZnO. To confirm the crystallographic orientation, however, additional measurements are necessary. Raman spectroscopy is ideal for this since also the Raman modes depend on the crystallographic orientation as described in chapter 3.3.3 and can in addition give insight into the crystal quality. The measurements were done in the setup described in chapter 3.3.4. For the polarization measurements with an arbitrary angle, a motorized $\lambda/2$-plate was added into the beam path between the notch filter and the microscope objective. In this configuration, the polarization of the excitation beam is rotated as well as the detection signal resulting in a *virtual* turn of the crystallographic axis with respect to the detection setup. The design of this setup was demonstrated by Kranert et al. [123] for β-Ga_2O_3. The rotation of the sample would in principle result in the same outcome but the focus position would vary if the focus would not exactly match the rotation axis.

Figure 6.3 shows the Raman spectra for the backscattering geometry and the four different polarizations labeled with their respective Porto notation, with x as the normal to the m-plane, z collinear to the c-axis and, y perpendicular to both resulting in collinearity to the a-plane. The polarization dependency for arbitrary angles of selected Raman modes are shown in the insets.

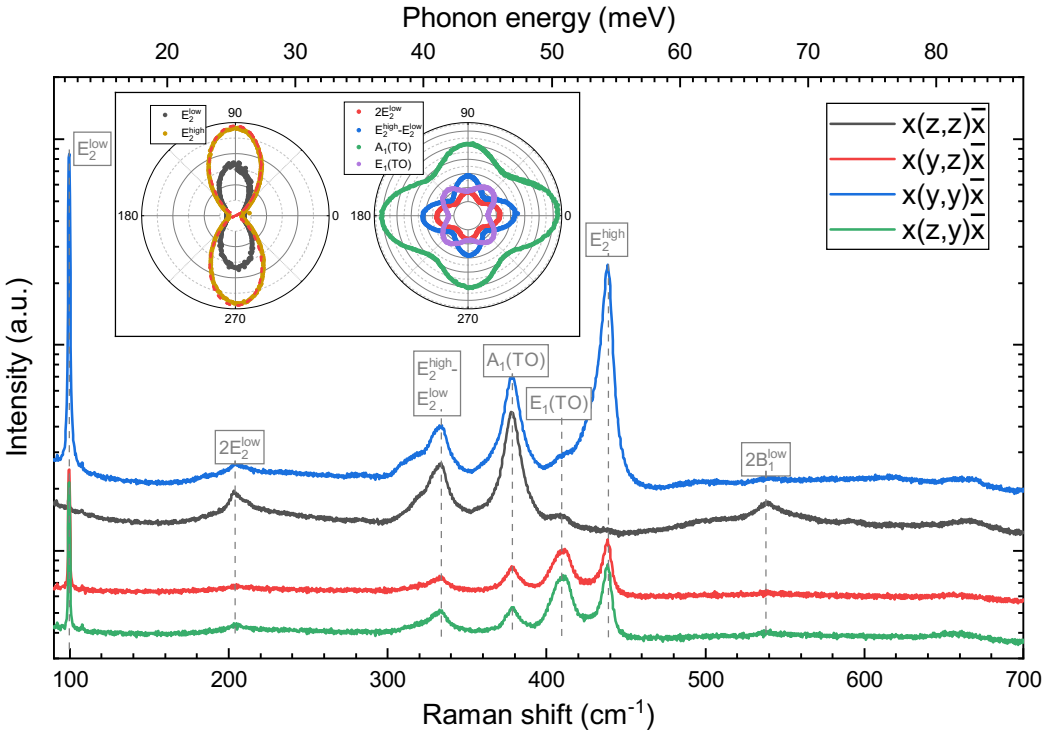

Fig. 6.5.: Polarized Raman spectra for different orientations labeled by the Porto notation. The polarization dependency for arbitrary angles (angle between E and c) of selected Raman modes are shown in the inset.

The E_2^{low} mode at $99.(5)\ \mathrm{cm}^{-1}$ has the lowest width of $w = (0.82 \pm 0.02)\ \mathrm{cm}^{-1}$ (based on a Lorentzian fit) which is close to the resolution limit of the setup indicating good crystalline quality.

Both E_2 modes show the same polarization dependence with a maximum for the intensity in the case of $E \perp c$ ($x(y,y)\bar{x}$) and a minimum for $E \parallel c$ ($x(z,z)\bar{x}$) where both modes vanish. The intensity follows an angle dependency of $I \propto \sin^4(\theta)$ [57] indicated by the red dashed line in the inset. The resulting dumbbell shape has its maximum only at $90°$ and $270°$ while the other modes show a fourfold symmetry.

Both polarization behavior of the E_2-modes are ideal to determine the two crystallographic axis of the surface plane. The identification of the c-axis and the perpendicular normal of the a-plane matches with the prior result of the PL and reflectance measurements.

6.3 Reflectance modeling

To model the reflectance spectra to obtain the dispersion curves of the exciton-polaritons a model presented by Fryar et al. [124] has been used which is based on a model by Thomas and Hopfield [125]. The model has been applied in a similar way on ZnO [117] as well as CuCl [104].

The transverse solution of Maxwell's equation for a single oscillator, i.e. a single exciton transition, the dielectric response is [126]:

$$\epsilon(\omega,k)=\frac{k^2c^2}{\omega^2}=\epsilon_\infty+\frac{1}{\epsilon_0}\left(\frac{\alpha_0\omega_0^2}{\omega_0^2+\beta k^2-\omega^2-i\omega\Gamma}\right), \tag{6.1}$$

where ω is the angular frequency of the incident radiation, k is the wavevector, ϵ_∞ is the static background dielectric constant, α_0 the static exciton polarizability, ω_0 the exciton frequency, Γ is the damping parameter, and with $\beta=\frac{\hbar\omega_0}{m^*}$, where m^* is the effective exciton mass.

The free A and B-exciton are energetically in close proximity in the spectrum, while the C-exciton is further away and active for the perpendicular polarization compared to the A and B-exciton. Hence for the modeling the two oscillators of the A and B-exciton needs to be regarded for the oscillations below the A-exciton (see marked area in figure 6.4). The condition for both excitons becomes [125, 127, 117, 104]

$$\begin{aligned}\frac{k^2c^2}{\omega^2}=\epsilon_\infty&+\frac{\alpha_{A0}}{\epsilon_0}\left(\frac{\omega_{AT}^2}{\omega_{AT}^2+\beta_A k^2-\omega^2-i\omega\Gamma_A}\right)\\&+\frac{\alpha_{B0}}{\epsilon_0}\left(\frac{\omega_{BT}^2}{\omega_{BT}^2+\beta_B k^2-\omega^2-i\omega\Gamma_B}\right),\end{aligned} \tag{6.2}$$

with

$$\beta_{A,B}=\frac{\hbar\omega_{AT,BT}}{m^*_{A,B}}. \tag{6.3}$$

Equation 6.2 can be expressed as

$$Ak^2=\epsilon_\infty+\frac{B}{C+\beta_A k^2}+\frac{D}{E+\beta_B k^2}, \tag{6.4}$$

with the expressions for

$$A = \frac{c^2}{\omega^2} \tag{6.5}$$

$$B = \frac{\alpha_{A0}}{\epsilon_0}\omega_{AT}^2 \tag{6.6}$$

$$C = \frac{\epsilon_0 B}{\alpha_{A0}} - \omega^2 - i\omega\Gamma_A \tag{6.7}$$

$$D = \frac{\alpha_{B0}}{\epsilon_0}\omega_{BT}^2 \tag{6.8}$$

$$E = \frac{\epsilon_0 D}{\alpha_{B0}} - \omega^2 - i\omega\Gamma_B. \tag{6.9}$$

This can rearranged and expressed as

$$\begin{aligned}&(A\beta_A\beta_B)k^6 + (AC\beta_B + AE\beta_A - \epsilon_\infty\beta_A\beta_B)k^4 + \\ &(ACE - \epsilon_\infty C\beta_B - \epsilon_\infty E\beta_A - B\beta_B - D\beta_A)k^2 - (\epsilon_\infty CE + BE + DC) = 0.\end{aligned} \tag{6.10}$$

Since this expression is cubic in k^2, there are six possible wavevectors k for each frequency ω, which can be divided into two sets of three different solutions, positive and negative, symmetric around $k = 0$. These three different solutions can be grouped into three different branches, the upper (lower) polariton branch as well as an intermediate branch between the A and B exciton. In the case of only one real positive solution, especially in the low energy range, the other two become imaginary (i.e. evanescent solutions).

There are two frequencies ω for which the value of the dielectric constant in equation 6.2 becomes zero, corresponding to the longitudinal frequencies ω_{AL} and ω_{BL} of the A and B exciton. The static polarizabilities in equation 6.2 can then expressed with the longitudinal and transverse frequencies of the excitons with the relations

$$\alpha_{A0} = \epsilon_\infty \left(\frac{\epsilon_0}{\omega_{AT}^2}\right)\left(\omega_{BL}^2 - \omega_{AT}^2\right)\left(\frac{\omega_{AL}^2 - \omega_{AT}^2}{\omega_{BT}^2 - \omega_{AT}^2}\right) \tag{6.11}$$

and

$$\alpha_{B0} = \epsilon_\infty \left(\frac{\epsilon_0}{\omega_{BT}^2}\right)\left(\omega_{AL}^2 - \omega_{BT}^2\right)\left(\frac{\omega_{BL}^2 - \omega_{BT}^2}{\omega_{AT}^2 - \omega_{BT}^2}\right). \tag{6.12}$$

To be able to solve the equations for three independent modes additional boundary conditions (ABC) are necessary. There are different conditions which can be applied but the most commonly used is the so called Pekar's ABC describing that the total polarization of each exciton branch vanishes at the crystal interface or at a finite distance from the interface. The boundary conditions are presented in the next

section for two different models. Based on these conditions equation 6.2 is solved for k at every frequency ω from that the refractive indices and polarizabilities are determined. After solving the boundary condition the reflectance can be computed and compared to the measured data. The computation of the fits was established in *Python* [128]. The source code can be found in the appendix in chapter A.2.

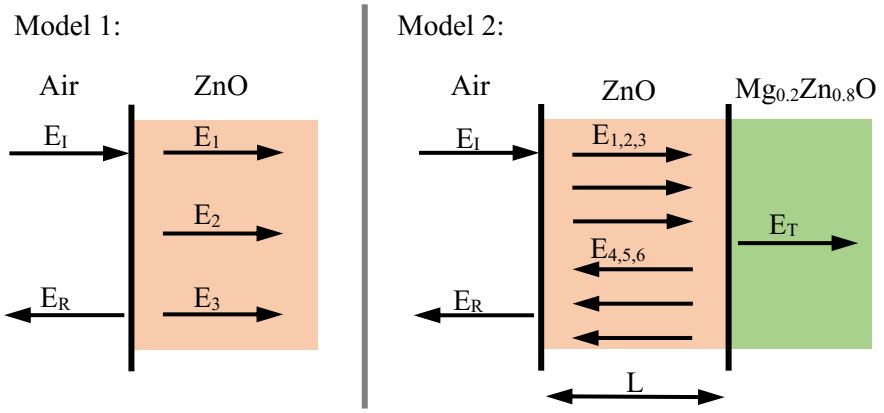

Fig. 6.6.: Sketches of reflectance models. For an infinite thick crystal only the reflectance on the front surface contributes in model 1. In model 2 a second interface to the substrate is considered. E_i are the electric field amplitudes and L the layer thickness.

6.3.1 Model 1: Infinite crystal thickness

For the first simple model, only the reflection on the interface is taken into account which would be the case of a crystal with infinite thickness. The incident and reflected light with their electric field intensities, E_I and E_R respectively, as well as the three possible exciton-polariton waves with their independent wavevector k_{1-3} are considered. Figure 6.6 shows a sketch of this model. Applying Maxwell's boundary conditions two equations can be obtained [125, 127, 117, 104]

$$E_I + E_R = E_1 + E_2 + E_3 \tag{6.13}$$

$$n_0 E_I - n_0 E_R = n_1 E_1 + n_2 E_2 + n_3 E_3, \tag{6.14}$$

and based on Pekar's ABC two additional equations

$$\alpha_A(k_1,\omega)E_1 + \alpha_A(k_2,\omega)E_2 + \alpha_A(k_3,\omega)E_3 = 0 \tag{6.15}$$

$$\alpha_B(k_1,\omega)E_1 + \alpha_B(k_2,\omega)E_2 + \alpha_B(k_3,\omega)E_3 = 0. \tag{6.16}$$

The polarizability of the A and B-exciton is depended on the frequency ω and the three wavevectors of the exciton-polariton modes k_{1-3}

$$\alpha_A(k_{1-3},\omega) = \epsilon_0(\epsilon_\infty - 1)\frac{\alpha_{A0}\omega_{AT}^2}{\omega_{AT}^2 + \beta_A k_{1-3}^2 - \omega^2 - i\omega\Gamma_A} \tag{6.17}$$

$$\alpha_B(k_{1-3},\omega) = \epsilon_0(\epsilon_\infty - 1)\frac{\alpha_{B0}\omega_{BT}^2}{\omega_{BT}^2 + \beta_B k_{1-3}^2 - \omega^2 - i\omega\Gamma_B}. \tag{6.18}$$

The boundary conditions presented in equation 6.13-6.16 can also expressed with the matrix equation

$$\begin{pmatrix} r \\ A \\ B \\ C \end{pmatrix} = \begin{pmatrix} -1 & 1 & 1 & 1 \\ 1 & n_1 & n_2 & n_3 \\ 0 & \alpha_{A1} & \alpha_{A2} & \alpha_{A3} \\ 0 & \alpha_{B1} & \alpha_{B2} & \alpha_{B3} \end{pmatrix}^{-1} \begin{pmatrix} 1 \\ 1 \\ 0 \\ 0 \end{pmatrix}, \tag{6.19}$$

with the reflection coefficient $r = E_R/E_I$ and the relative intensities $A = E_1/E_I$, $B = E_2/E_I$, and $C = E_3/E_I$. The refractive index n_{1-3} corresponds to each exciton-polariton mode by $n_i = \sqrt{\frac{k_i^2 c^2}{\omega^2}}$. By solving the matrix equation 6.19 for the reflection coefficient r, the reflectance can be obtained by squaring the solution.

6.3.2 Model 2: Finite crystal thickness

For the second model the surface interface as well as the interface on the backside of the ZnO layer with the thickness L is considered (see figure6.3. The three exciton-polariton modes with their electric field intensities E_{1-3} have now three additional modes E_{4-6} reflected on the backside of the ZnO layer. The transmitted part into the substrate E_T is modeled with a single mode. [125, 127, 117, 104]

$$E_I + E_R = E_T \tag{6.20}$$

$$E_I + E_R = E_1 + E_2 + E_3 + E_4 + E_5 + E_6 \tag{6.21}$$

$$n_0 E_I - n_0 E_R = n_1 E_1 + n_2 E_2 + n_3 E_3 - n_1 E_4 - n_2 E_5 - n_3 E_6 \tag{6.22}$$

The sets of additional boundary conditions for the air-Zno and ZnO-MgZnO interfaces for the A and B-exciton are

$$\alpha_{0A}(k_1,\omega)(E_1 + E_4) + \alpha_{0A}(k_2,\omega)(E_2 + E_5) + \alpha_{0A}(k_3,\omega)(E_3 + E_6) = 0 \tag{6.23}$$

$$\alpha_{0B}(k_1,\omega)(E_1 + E_4) + \alpha_{0B}(k_2,\omega)(E_2 + E_5) + \alpha_{0B}(k_3,\omega)(E_3 + E_6) = 0, \tag{6.24}$$

and

$$\begin{aligned}
&\alpha_{0A}(k_1,\omega)\left(E_1\exp\left(i\frac{n_1\omega L}{c}\right)+E_4\exp\left(-i\frac{n_1\omega L}{c}\right)\right)+\\
&\alpha_{0A}(k_2,\omega)\left(E_2\exp\left(i\frac{n_2\omega L}{c}\right)+E_5\exp\left(-i\frac{n_2\omega L}{c}\right)\right)+\\
&\alpha_{0A}(k_3,\omega)\left(E_3\exp\left(i\frac{n_3\omega L}{c}\right)+E_6\exp\left(-i\frac{n_3\omega L}{c}\right)\right)=0 \qquad (6.25)\\
&\alpha_{0B}(k_1,\omega)\left(E_1\exp\left(i\frac{n_1\omega L}{c}\right)+E_4\exp\left(-i\frac{n_1\omega L}{c}\right)\right)+\\
&\alpha_{0B}(k_2,\omega)\left(E_2\exp\left(i\frac{n_2\omega L}{c}\right)+E_5\exp\left(-i\frac{n_2\omega L}{c}\right)\right)+\\
&\alpha_{0B}(k_3,\omega)\left(E_3\exp\left(i\frac{n_3\omega L}{c}\right)+E_6\exp\left(-i\frac{n_3\omega L}{c}\right)\right)=0 \qquad (6.26)
\end{aligned}$$

respectively. Again, all sets of equations can be expressed in matrix form

$$\begin{pmatrix} r\\ A\\ B\\ C\\ D\\ E\\ F\\ G\end{pmatrix}=\begin{pmatrix} -1 & 1 & 1 & 1 & 1 & 1 & 1 & 0\\ 1 & n_1 & n_2 & n_3 & -n_1 & -n_2 & -n_3 & 0\\ 0 & e_1 & e_2 & e_3 & e_1^* & e_2^* & e_3^* & -1\\ 0 & n_1e_1 & n_2e_2 & n_3e_3 & -n_1e_1^* & -n_2e_2^* & -n_3e_3^* & -n_s\\ 0 & \alpha_{A1} & \alpha_{A2} & \alpha_{A3} & \alpha_{A1} & \alpha_{A2} & \alpha_{A3} & 0\\ 0 & \alpha_{B1} & \alpha_{B2} & \alpha_{B3} & \alpha_{B1} & \alpha_{B2} & \alpha_{B3} & 0\\ 0 & \alpha_{A1}e_1 & \alpha_{A2}e_2 & \alpha_{A3}e_3 & \alpha_{A1}e_1^* & e_2^*\alpha_{A2} & e_3^*\alpha_{A3} & 0\\ 0 & \alpha_{B1}e_1 & \alpha_{B2}e_2 & \alpha_{B3}e_3 & \alpha_{B1}e_1^* & e_2^*\alpha_{B2} & e_3^*\alpha_{B3} & 0\end{pmatrix}^{-1}\begin{pmatrix}1\\1\\0\\0\\0\\0\\0\\0\end{pmatrix}, \qquad (6.27)$$

with $e_i=\exp\left(i\frac{n_i\omega L}{c}\right)$ and $e_i^*=\exp\left(-i\frac{n_i\omega L}{c}\right)$. As for the first model, the matrix equation contains the relative field intensities as well as the reflective coefficient r which results the reflectance when squared.

6.3.3 Results of the models

To fit the data initial values have been determined based on the PL and reflectance measurement, in particular the energy of the longitudinal free A and B exciton, E_{LA} and E_{LB} respectively, the LA-splitting of the excitons, ΔLT_A, and ΔLT_B as well as the width, which correlates to the damping, Γ_A, and Γ_B. The background dielectric function ϵ_∞ can be derived from the refractive index of ZnO far removed from the exciton-polariton oscillation with $n=\sqrt{\epsilon_\infty}$. The thickness of the ZnO layer L regarded in model 2 was also known from the growth.

Figure 6.7 a) shows a comparison of the obtained reflectance data for $E\perp c$ (see the marked area in figure 6.4) and the results of the two fit models.

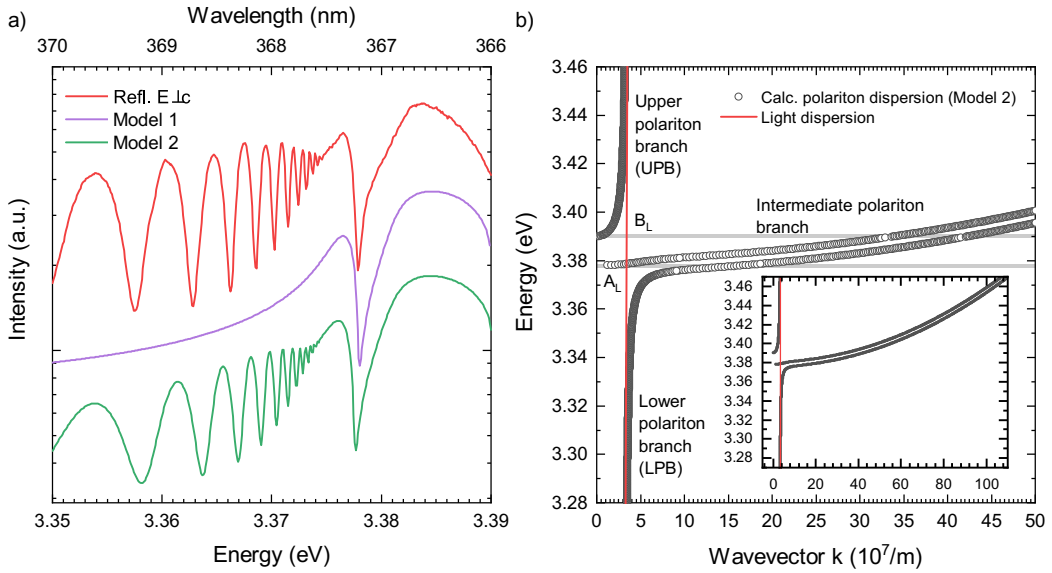

Fig. 6.7.: a) Comparison of the obtained reflectance data for $E \perp c$ and the two different fit models. b) Calculated exciton-polariton dispersion based in model 2. The inset show the same dispersion curve but for a larger interval of k

The results of the first model do not show any of the oscillations since the ZnO layer is treated with an infinite thickness. The model, however, fits the free A and B-exciton region is accurate. Hence, the obtained parameters can be used as new initial values for model 2. Due to the finite layer thickness L in model 2 the exciton-polariton modes can progress in the layer until they reach the backside of the layer, get reflected and are hence able to interfere to yield the Fabry-Pérot interference pattern visible in the reflectance spectrum. Figure 6.7 b) show the individual values of k_{1-3} for every energy E, i.e. the dispersion of the exciton-polaritons as a result of model 2. The red almost vertical line represents the dispersion of light which acts as an asymptote due to the non-crossing rule for the exciton-polariton dispersion curve. The dispersion curve is in good agreement with the prior published data by Wrzesinski and Fröhlich [120] based on two-photon and three-photon spectroscopy on single ZnO crystals. The resulting fit parameters of model 2 are summarized in table 6.2.

6.4 Conclusion

The investigated m-plane ZnO layer show narrow spectral lines in the PL spectrum in the expected region of donor-bound excitons and the region of the free A-exciton. Due to the crystal orientation, a fine structure of the A-exciton is revealed by polarization-dependent measurements, and distinct peaks can be seen for the

Tab. 6.2.: Resulting Fit-Parameters for model 2

Parameter	this work	Reference				
		Bulk [117]	PLD [117]	[127]	[121]	[122]
Transverse A-exciton energy A_T (eV)	3.3760	3.375	3.378	3.3758	3.3778	3.37538
Longitudinal A-exciton energy A_T (eV)	3.3781	3.377	3.380	3.3776	3.3805	3.37735
LT-splitting A-exciton ΔA_{LT} (meV)	2.1	2	2	1.8	2.7	2.0
Transverse B-exciton energy B_T (eV)	3.3845	3.381	3.390	3.381	3.3834	3.3815
Longitudinal B-exciton energy A_T (eV)	3.3932	3.393	3.394	3.3912	3.3940	3.3917
LT-splitting B-exciton ΔB_{LT} (meV)	8.7	12	4	10.2	10.6	10.2
Transverse A-B exciton splitting $\Delta_{A_T B_T}$ (meV)	8.5	6	12	5.2	5.6	6.12
Damping A-exciton $\hbar\Gamma_A$ (meV)	0.3	1	7	0.7	-	-
Damping B-exciton $\hbar\Gamma_B$ (meV)	0.1	1	14	0.7	-	-

Γ_1 transverse A-exciton in π-polarization and the Γ_5 transverse A-exciton in the opposite σ-polarization. In addition, a strong Fabry-Pérot interference pattern can be observed in σ-polarization with an intensity even exceeding the narrow lines of the donor-bound excitons. The interference pattern starts spectrally from the Γ_5 transverse A-exciton to lower energies exceeding the donor-bound exciton lines with an increase of the width and distance of maxima of adjacent oscillations. Temperature-dependent PL reveals the close connection of the Fabry-Pérot interference pattern to the Γ_5 transverse A-exciton by indicating the same spectral shift. The crystal's orientation of the sample is in agreement with the polarization-dependent modes found in Raman spectroscopy and high crystalline quality can be assured based on the narrow linewidth of the modes.

In reflectance measurements, a similar Fabry-Pérot interference pattern is present energetically below the A-exciton but additionally also between the A and C-exciton, as well as above the C-exciton. The greater expansion of the pattern in reflectance compared to PL measurements can be explained by the origin of the light itself. While in reflectance the light is polychromatic and stems from the external light source with high intensity throughout the whole NBE-region, in PL the light for the interference pattern is the background illumination of the sample generated by the laser excitation. In the region energetically above the A-exciton, the luminescence of the sample is several orders of magnitude lower than in the region below the A-exciton, hence no interference pattern is visible.

The interference pattern in the reflectance spectrum in the proximity of the C-exciton is of opposite polarization (π) as the pattern below the A-exciton (σ). Hence, to model the reflectance spectrum below the A-exciton a two-oscillator (to consider A and B exciton) exciton-polariton models with spatial dispersion based by Fryar et al. [117] were used. The model with infinite layer thickness shows no interference pattern as expected, due to the missing back-reflection of the back interface. The

model, however, is already in good agreement with the reflection of the free A and B-exciton. By introducing a back interface in the model with finite thickness a Fabry-Pérot interference pattern becomes visible in the model. As a result of this second model, an exciton-polariton dispersion with an upper, lower, and intermediate polariton branch was calculated.

The damping of the A and B exciton is lower as in other samples presented in the literature (see table 6.2) and is directly related to the crystal and optical quality. Samples grown with a growth method that would commonly yield crystals with a poorer quality such as grown by pulsed laser deposition show a significant larger exciton damping. In conclusion, the m-plane crystal geometry as well an extraordinary high optical quality due to a low defect and impurity density are responsible for the appearance of the Fabry-Pérot interference pattern. In m-plane samples transverse exciton-polaritons can be directly observed in a normal backscattering geometry. An interference pattern can hence only be observed if the exciton-polariton modes can propagate at least two passes through the film.

Bibliography

[1] J. W. Nowak, R. Braithwaite, J. Nowak, et al. “Formation of large synthetic zincite (ZnO) crystals during production of zinc white”. In: *J. Gemmol.* 30.5 (2007), pp. 257–267. DOI: 10.15506/jog.2007.30.5.257 (cit. on p. 3).

[2] H. Morkoç and Ü. Özgür. *Zinc oxide: fundamentals, materials and device technology*. 2008 (cit. on p. 3).

[3] C. Klingshirn, A. Waag, A. Hoffmann, and J. Geurts. *Zinc Oxide: From Fundamental Properties Towards Novel Applications*. 2010 (cit. on pp. 3, 6, 9).

[4] M. S. Ramachandra Rao and T. Okada. *ZnO Nanocrystals and Allied Materials*. Vol. 180. 2014. DOI: 10.1007/978-81-322-1160-0 (cit. on p. 3).

[5] M. J. Mehl. “A Brief History of Strukturbericht Symbols and Other Crystallographic Classification Schemes”. In: *J. Phys. Conf. Ser.* Vol. 1290. 1. Institute of Physics Publishing, Oct. 2019, p. 12016. DOI: 10.1088/1742-6596/1290/1/012016 (cit. on p. 4).

[6] W. Friedrich, P. Knipping, and M. Laue. “Interferenzerscheinungen bei Röntgenstrahlen”. In: *Ann. Phys.* 346.10 (Jan. 1913), pp. 971–988. DOI: 10.1002/andp.19133461004 (cit. on p. 4).

[9] H. Morkoç and Ü. Özgür. *General Properties of ZnO*. 2009, pp. 1–76. DOI: 10.1002/9783527623945.ch1 (cit. on p. 5).

[11] G. Aminoff. “XXIV. Über Lauephotogramme und Struktur von Zinkit”. In: *Zeitschrift für Krist. - Cryst. Mater.* 56.1-6 (1921), pp. 495–505. DOI: 10.1524/zkri.1921.56.1.495 (cit. on p. 5).

[13] C. F. MacRae, I. Sovago, S. J. Cottrell, et al. “Mercury 4.0: From visualization to analysis, design and prediction”. In: *J. Appl. Crystallogr.* 53.1 (Feb. 2020), pp. 226–235. DOI: 10.1107/S1600576719014092 (cit. on p. 5).

[14] D. G. Thomas. “The exciton spectrum of zinc oxide”. In: *J. Phys. Chem. Solids* 15.1-2 (Aug. 1960), pp. 86–96. DOI: 10.1016/0022-3697(60)90104-9 (cit. on p. 6).

[15] J. J. Hopfield. “Fine structure in the optical absorption edge of anisotropic crystals”. In: *J. Phys. Chem. Solids* 15.1-2 (Aug. 1960), pp. 97–107. DOI: 10.1016/0022-3697(60)90105-0 (cit. on p. 6).

[16] G. Cantwell, W. C. Harsch, and B. Jogai. “Valence-band ordering in zno”. In: *Phys. Rev. B - Condens. Matter Mater. Phys.* 60.4 (1999), pp. 2340–2344. DOI: 10.1103/PhysRevB.60.2340 (cit. on p. 6).

[17] M. R. Wagner. “Fundamental properties of excitons and phonons in ZnO : A spectroscopic study of the dynamics , polarity , and effects of external fields”. PhD thesis (cit. on pp. 6, 15, 16, 39, 68).

[18] M. R. Wagner, J. H. Schulze, R. Kirste, et al. “Γ7 valence band symmetry related hole fine splitting of bound excitons in ZnO observed in magneto-optical studies”. In: *Phys. Rev. B - Condens. Matter Mater. Phys.* 80.20 (Nov. 2009), p. 205203. DOI: 10.1103/PHYSREVB.80.205203/FIGURES/4/MEDIUM (cit. on pp. 6, 15, 16, 39).

[19] M. Fiebig, D. Fröhlich, and C. Pahlke-Lerch. “Multiphoton Polariton Spectroscopy on ZnO”. In: *Phys. status solidi* 177.1 (May 1993), pp. 187–199. DOI: 10.1002/pssb.2221770114 (cit. on pp. 6, 75).

[20] M. Cobet. “Ellipsometric study of ZnO from multimode formation of Exciton-Polaritons to the Core-level regime”. In: *Ellipsom. study ZnO from multimode Form. Excit. to Core-level regime* (2010) (cit. on p. 7).

[21] K. Hümmer. “Exzitonische Polaritonen in einachsigen Kristallen”. PhD thesis. Friedrich- Alexander-Universität, Erlangen-Nürnberg, 1978 (cit. on pp. 7, 71).

[22] J. Qiu, J. M. DePuydt, H. Cheng, and M. A. Haase. “Heavily doped p-ZnSe:N grown by molecular beam epitaxy”. In: *Appl. Phys. Lett.* 59.23 (June 1991), pp. 2992–2994. DOI: 10.1063/1.105821 (cit. on p. 8).

[23] H. Amano, M. Kito, K. Hiramatsu, and I. Akasaki. “P-type conduction in Mg-doped GaN treated with low-energy electron beam irradiation (LEEBI)”. In: *Jpn. J. Appl. Phys.* 28.12 A (Dec. 1989), pp. L2112–L2114. DOI: 10.1143/JJAP.28.L2112 (cit. on p. 8).

[25] S. Nakamura, S. Pearton, and G. Fasol. *The Blue Laser Diode*. Springer Berlin Heidelberg, 2000. DOI: 10.1007/978-3-662-04156-7 (cit. on p. 8).

[26] D. C. Look, J. W. Hemsky, and J. R. Sizelove. “Residual native shallow donor in ZnO”. In: *Phys. Rev. Lett.* 82.12 (Mar. 1999), pp. 2552–2555. DOI: 10.1103/PhysRevLett.82.2552 (cit. on p. 9).

[27] Y. Kanai. “Admittance spectroscopy of cu-doped zno crystals”. In: *Jpn. J. Appl. Phys.* 30.4 (Apr. 1991), pp. 703–707. DOI: 10.1143/JJAP.30.703 (cit. on p. 9).

[28] Y. J. Zeng, Z. Z. Ye, W. Z. Xu, et al. “Dopant source choice for formation of p -type ZnO: Li acceptor”. In: *Appl. Phys. Lett.* 88.6 (Feb. 2006), p. 62107. DOI: 10.1063/1.2172743 (cit. on p. 9).

[29] K. Minegishi, Y. Koiwai, Y. Kikuchi, et al. “Growth of p-type zinc oxide films by chemical vapor deposition”. In: *Japanese J. Appl. Physics, Part 2 Lett.* 36.11 PART A (Nov. 1997), p. 1453. DOI: 10.1143/jjap.36.l1453 (cit. on p. 9).

[30] K. K. Kim, H. S. Kim, D. K. Hwang, J. H. Lim, and S. J. Park. “Realization of p-type ZnO thin films via phosphorus doping and thermal activation of the dopant”. In: *Appl. Phys. Lett.* 83.1 (July 2003), pp. 63–65. DOI: 10.1063/1.1591064 (cit. on p. 9).

[31] Y. R. Ryu, T. S. Lee, and H. W. White. “Properties of arsenic-doped p-type ZnO grown by hybrid beam deposition”. In: *Appl. Phys. Lett.* 83.1 (July 2003), pp. 87–89. DOI: 10.1063/1.1590423 (cit. on p. 9).

[32] T. Aoki, Y. Shimizu, A. Miyake, et al. *p-type ZnO layer formation by excimer laser doping*. Tech. rep. 2. 2002, pp. 911–914. DOI: 10.1002/1521-3951(200201)229:2<911::AID-PSSB911>3.0.CO;2-R (cit. on p. 9).

[33] J. L. Lyons, A. Janotti, and C. G. Van De Walle. “Why nitrogen cannot lead to p -type conductivity in ZnO”. In: *Appl. Phys. Lett.* 95.25 (Dec. 2009), p. 252105. DOI: 10.1063/1.3274043 (cit. on p. 9).

[34] M. C. Tarun, M. Z. Iqbal, and M. D. McCluskey. “Nitrogen is a deep acceptor in ZnO”. In: *AIP Adv.* 1.2 (June 2011), p. 22105. DOI: 10.1063/1.3582819 (cit. on p. 9).

[35] A. Janotti, E. Snow, and C. G. Van De Walle. “A pathway to p-type wide-band-gap semiconductors”. In: *Appl. Phys. Lett.* 95.17 (Oct. 2009), p. 172109. DOI: 10.1063/1.3247890 (cit. on p. 9).

[36] S. Limpijumnong, S. B. Zhang, S. H. Wei, and C. H. Park. “Doping by large-size-mismatched impurities: The microscopic origin of arsenicor antimony-doped p-type zinc oxide”. In: *Phys. Rev. Lett.* 92.15 (Apr. 2004), pp. 155504–1. DOI: 10.1103/PhysRevLett.92.155504 (cit. on p. 9).

[37] F. X. Xiu, Z. Yang, L. J. Mandalapu, et al. “High-mobility Sb-doped p-type ZnO by molecular-beam epitaxy”. In: *Appl. Phys. Lett.* 87.15 (2005), pp. 1–3. DOI: 10.1063/1.2089183 (cit. on p. 9).

[38] F. X. Xiu, Z. Yang, L. J. Mandalapu, D. T. Zhao, and J. L. Liu. “Photoluminescence study of Sb-doped p -type ZnO films by molecular-beam epitaxy”. In: *Appl. Phys. Lett.* 87.25 (2005), pp. 1–3. DOI: 10.1063/1.2146208 (cit. on p. 9).

[39] F. X. Xiu and J. L. Liu. “Response to "Comment on ’Photoluminescence study of Sb-doped p -type ZnO films by molecular-beam epitaxy’" [Appl. Phys. Lett. 90, 116102 (2007)]”. In: *Appl. Phys. Lett.* 90.11 (2007), pp. 116102–116104. DOI: 10.1063/1.2713174 (cit. on p. 9).

[40] Y. J. Zeng, Z. Z. Ye, W. Z. Xu, et al. “P-type behavior in nominally undoped ZnO thin films by oxygen plasma growth”. In: *Appl. Phys. Lett.* 88.26 (2006). DOI: 10.1063/1.2217165 (cit. on p. 9).

[41] Y. J. Zeng and Z. Z. Ye. “Comment on "Photoluminescence study of Sb-doped p-type ZnO films by molecular-beam epitaxy" [Appl. Phys. Lett. 87, 252102 (2005)]”. In: *Appl. Phys. Lett.* 90.11 (2007), pp. 116101–116103. DOI: 10.1063/1.2713173 (cit. on p. 9).

[42] George Gabriel Stokes. “XXX. On the change of refrangibility of light”. In: *Philos. Trans. R. Soc. London* 142 (Dec. 1852), pp. 463–562. DOI: 10.1098/rstl.1852.0022 (cit. on p. 11).

[44] D. M. Hofmann, A. Hofstaetter, F. Leiter, et al. “Hydrogen: A Relevant Shallow Donor in Zinc Oxide”. In: *Phys. Rev. Lett.* 88.4 (Jan. 2002), p. 045504. DOI: 10.1103/PhysRevLett.88.045504 (cit. on p. 14).

[45] D. Savchenko, A. Vasin, O. Kuz, et al. “Role of the paramagnetic donor-like defects in the high n-type conductivity of the hydrogenated ZnO microparticles”. In: *Sci. Rep.* 10.1 (Dec. 2020). DOI: 10.1038/S41598-020-74449-3 (cit. on p. 14).

[46] D. Block, A. Hervé, and R. T. Cox. “Optically detected magnetic resonance and optically detected ENDOR of shallow indium donors in ZnO”. In: *Phys. Rev. B* 25.9 (May 1982), p. 6049. DOI: 10.1103/PhysRevB.25.6049 (cit. on p. 14).

[47] C. A. Arguello, D. L. Rousseau, and S. P. Porto. “First-order raman effect in wurtzite-type crystals”. In: *Phys. Rev.* 181.3 (May 1969), pp. 1351–1363. DOI: 10.1103/PhysRev.181.1351 (cit. on p. 18).

[48] T. C. Damen, S. P. Porto, and B. Tell. “Raman effect in zinc oxide”. In: *Phys. Rev.* 142.2 (Feb. 1966), pp. 570–574. DOI: 10.1103/PhysRev.142.570 (cit. on p. 18).

[49] A. Smekal. “Zur Quantentheorie der Dispersion”. In: *Naturwissenschaften* 11.43 (Oct. 1923), pp. 873–875. DOI: 10.1007/BF01576902 (cit. on p. 19).

[50] C. G. DARWIN. “A Quantum Theory of Optical Dispersion”. In: *Nature* 110.2773 (Dec. 1922), pp. 841–842. DOI: 10.1038/110841a0 (cit. on p. 19).

[51] C. V. Raman and K. S. Krishnan. “A New Type of Secondary Radiation”. In: *Nature* 121.3048 (Mar. 1928), pp. 501–502. DOI: 10.1038/121501c0 (cit. on p. 19).

[53] G. Landsberg and L. Mandelstam. “Über die Lichtzerstreuung in Kristallen”. In: *Zeitschrift für Phys.* 50.11-12 (Nov. 1928), pp. 769–780. DOI: 10.1007/BF01339412 (cit. on p. 19).

[54] R. Singh. “C. V. Raman and the Discovery of the Raman Effect”. In: *Phys. Perspect.* 4.4 (Dec. 2002), pp. 399–420. DOI: 10.1007/s000160200002 (cit. on p. 19).

[55] P. Y. Yu and M. Cardona. “Optical Properties II”. In: 2010, pp. 345–426. DOI: 10.1007/978-3-642-00710-1_7 (cit. on pp. 19, 21).

[56] J. M. Calleja and M. Cardona. “Resonant Raman scattering in ZnO”. In: *Phys. Rev. B* 16.8 (Oct. 1977), pp. 3753–3761. DOI: 10.1103/PhysRevB.16.3753 (cit. on pp. 21, 22, 51, 53).

[57] T. Sander, S. Eisermann, B. K. Meyer, and P. J. Klar. “Raman tensor elements of wurtzite ZnO”. In: *Phys. Rev. B* 85.16 (Apr. 2012), p. 165208. DOI: 10.1103/PhysRevB.85.165208 (cit. on pp. 22, 76).

[58] V. S. Vinogradov, V. N. Dzhagan, T. N. Zavaritskaya, et al. “Optical phonons in the bulk and on the surface of ZnO and ZnTe/ZnO nanowires in Raman spectra”. In: *Phys. Solid State* 54.10 (2012), pp. 2083–2090. DOI: 10.1134/S1063783412100332 (cit. on p. 22).

[59] R. Cuscó, E. Alarcón-Lladó, J. Ibáñez, et al. “Temperature dependence of Raman scattering in ZnO”. In: *Phys. Rev. B - Condens. Matter Mater. Phys.* 75.16 (Apr. 2007), p. 165202. DOI: 10.1103/PhysRevB.75.165202 (cit. on pp. 23, 51, 53).

[60] M. Fleischmann, P. J. Hendra, and A. J. McQuillan. “Raman spectra of pyridine adsorbed at a silver electrode”. In: *Chem. Phys. Lett.* 26.2 (May 1974), pp. 163–166. DOI: 10.1016/0009-2614(74)85388-1 (cit. on p. 23).

[61] M. G. Albrecht and J. A. Creighton. “Anomalously intense Raman spectra of pyridine at a silver electrode”. In: *J. Am. Chem. Soc.* 99.15 (1977), pp. 5215–5217. DOI: 10.1021/ja00457a071 (cit. on p. 23).

[62] E. Poliani, M. R. Wagner, A. Vierck, et al. “Breakdown of Far-Field Raman Selection Rules by Light–Plasmon Coupling Demonstrated by Tip-Enhanced Raman Scattering”. In: *J. Phys. Chem. Lett.* 8.22 (Nov. 2017), pp. 5462–5471. DOI: 10.1021/ACS.JPCLETT.7B02505 (cit. on p. 24).

[63] M. D. C. Ries. “Optical analysis of InN and InGaN nanostructures”. Doctoral Thesis. Berlin: Technische Universität Berlin, 2021. DOI: 10.14279/depositonce-11647 (cit. on p. 24).

[64] E. Poliani, M. R. Wagner, J. S. Reparaz, et al. “Nanoscale Imaging of InN Segregation and Polymorphism in Single Vertically Aligned InGaN/GaN Multi Quantum Well Nanorods by Tip-Enhanced Raman Scattering”. In: *Nano Lett.* 13.7 (July 2013), pp. 3205–3212. DOI: 10.1021/NL401277Y (cit. on p. 24).

[65] P. E. Ciddor. “Refractive index of air: new equations for the visible and near infrared”. In: *Appl. Opt.* 35.9 (1996), p. 1566. DOI: 10.1364/ao.35.001566 (cit. on p. 24).

[66] B. K. Meyer, H. Alves, D. M. Hofmann, et al. “Bound exciton and donor–acceptor pair recombinations in ZnO”. In: *Phys. status solidi* 241.2 (Feb. 2004), pp. 231–260. DOI: 10.1002/pssb.200301962 (cit. on pp. 31, 35, 59, 75).

[67] M. Biswas, Y. S. Jung, H. K. Kim, et al. “Microscopic origins of the surface exciton photoluminescence peak in ZnO nanostructures”. In: *Phys. Rev. B - Condens. Matter Mater. Phys.* 83.23 (June 2011), p. 235320. DOI: 10.1103/PhysRevB.83.235320 (cit. on p. 31).

[68] M. R. Wagner, G. Callsen, J. S. Reparaz, et al. “Bound excitons in ZnO: Structural defect complexes versus shallow impurity centers”. In: *Phys. Rev. B* 84.3 (July 2011), p. 035313. DOI: 10.1103/PhysRevB.84.035313 (cit. on pp. 32, 37, 75).

[69] J. Cullen, D. Byrne, K. Johnston, E. McGlynn, and M. O. Henry. “Chemical identification of luminescence due to Sn and Sb in ZnO”. In: *Appl. Phys. Lett.* 102.19 (2013), p. 192110. DOI: 10.1063/1.4807288 (cit. on p. 32).

[70] S. Lautenschlaeger, J. Sann, N. Volbers, et al. “Asymmetry in the excitonic recombinations and impurity incorporation of the two polar faces of homoepitaxially grown ZnO films”. In: *Phys. Rev. B* 77.14 (Apr. 2008), p. 144108. DOI: 10.1103/PhysRevB.77.144108 (cit. on pp. 32, 57).

[71] L. Vina and S. Logothetidis. “Temperature dependence of the dielectric function of germanium”. In: *Phys. Rev. B* (1984) (cit. on pp. 35, 36, 60, 73).

[72] Y. P. Varshni. “Temperature dependence of the energy gap in semiconductors”. In: *Physica* 34.1 (Jan. 1967), pp. 149–154. DOI: 10.1016/0031-8914(67)90062-6 (cit. on p. 35).

[73] G. D. Cody. “Chapter 2 The Optical Absorption Edge of a-Si: H”. In: *Semicond. Semimetals* 21.PB (Jan. 1984), pp. 11–82. DOI: 10.1016/S0080-8784(08)62910-5 (cit. on p. 35).

[74] M. B. Bouzourâa, Y. Battie, S. Dalmasso, et al. “Comparative study of ZnO optical dispersion laws”. In: *Superlattices Microstruct.* 104 (Apr. 2017), pp. 24–36. DOI: 10.1016/j.spmi.2017.01.044 (cit. on p. 35).

[75] K. P. O’Donnell and X. Chen. “Temperature dependence of semiconductor band gaps”. In: *Appl. Phys. Lett.* 58.25 (1991), p. 2924. DOI: 10.1063/1.104723 (cit. on p. 35).

[76] R. Pässler. “Semi-empirical descriptions of temperature dependences of band gaps in semiconductors”. In: *Phys. status solidi* 236.3 (Apr. 2003), pp. 710–728. DOI: 10.1002/pssb.200301752 (cit. on p. 35).

[77] M. Hegde, F. Mohammadbeigi, T. Kure, et al. “Triple group-V donors in ZnO”. In: *J. Appl. Phys.* 127.7 (Feb. 2020), p. 075705. DOI: 10.1063/1.5144203 (cit. on p. 38).

[78] A. V. Rodina, M. Strassburg, M. Dworzak, et al. “Magneto-optical properties of bound excitons in ZnO”. In: *Phys. Rev. B - Condens. Matter Mater. Phys.* 69.12 (Mar. 2004), p. 125206. DOI: 10.1103/PhysRevB.69.125206 (cit. on pp. 39, 68).

[79] B. K. Meyer, J. Sann, S. Lautenschläger, M. R. Wagner, and A. Hoffmann. “Ionized and neutral donor-bound excitons in ZnO”. In: *Phys. Rev. B - Condens. Matter Mater. Phys.* 76.18 (Nov. 2007), p. 184120. DOI: 10.1103/PhysRevB.76.184120 (cit. on p. 40).

[80] J. Gutowski, N. Presser, and I. Broser. “Acceptor-exciton complexes in ZnO: A comprehensive analysis of their electronic states by high-resolution magnetooptics and excitation spectroscopy”. In: *Phys. Rev. B* 38.14 (Nov. 1988), pp. 9746–9758. DOI: 10.1103/PhysRevB.38.9746 (cit. on pp. 43, 65).

[81] B. K. Meyer, J. Sann, S. Eisermann, et al. “Excited state properties of donor bound excitons in ZnO”. In: *Phys. Rev. B - Condens. Matter Mater. Phys.* 82.11 (Sept. 2010), p. 115207. DOI: 10.1103/PhysRevB.82.115207 (cit. on pp. 43, 65).

[82] G. H. Watson, W. B. Daniels, and C. S. Wang. “Measurements of Raman intensities and pressure dependence of phonon frequencies in sapphire”. In: *J. Appl. Phys.* 52.2 (Feb. 1981), pp. 956–958. DOI: 10.1063/1.328785 (cit. on pp. 51, 53).

[83] a. Kaschner, U. Haboeck, M. M. Strassburg, et al. “Nitrogen-related local vibrational modes in ZnO:N”. In: *Appl. Phys. Lett.* 80.11 (2002), pp. 1909–1911. DOI: 10.1063/1.1461903 (cit. on pp. 51, 53).

[84] C. Bundesmann, N. Ashkenov, M. Schubert, et al. “Raman scattering in ZnO thin films doped with Fe, Sb, Al, Ga, and Li”. In: *Appl. Phys. Lett.* 83.10 (2003), pp. 1974–1976. DOI: 10.1063/1.1609251 (cit. on pp. 51–53).

[85] S.-H. Choi, D. Lim, J. W. Park, D. H. Kim, and M. Lee. “The Role of Carbon Doping in ZnO”. In: *J. Korean Phys. Soc.* 57.6 (Dec. 2010), pp. 1482–1485. DOI: 10.3938/JKPS.57.1482 (cit. on pp. 57, 62).

[86] N. H. Nickel, F. Friedrich, J. F. Rommeluère, and P. Galtier. “Vibrational spectroscopy of undoped and nitrogen-doped ZnO grown by metalorganic chemical vapor deposition”. In: *Appl. Phys. Lett.* 87.21 (Nov. 2005), p. 211905. DOI: 10.1063/1.2133917 (cit. on p. 57).

[87] S. P. Watkins, F. Mohammadbeigi, K. Stirling, and E. S. Kumar. “Identification of the shallow donor state in Sb doped ZnO by photoluminescence excitation spectroscopy”. In: *J. Appl. Phys.* 124.19 (2018), p. 195701. DOI: 10.1063/1.5054337 (cit. on pp. 58, 59).

[88] R. Heinhold, A. Neiman, J. V. Kennedy, et al. “Hydrogen-related excitons and their excited-state transitions in ZnO”. In: *Phys. Rev. B* 95.5 (Feb. 2017), p. 054120. DOI: 10.1103/PhysRevB.95.054120 (cit. on pp. 59, 60).

[89] A. Janotti and C. G. Van de Walle. “Hydrogen multicentre bonds”. In: *Nat. Mater. 2007 61* 6.1 (Dec. 2006), pp. 44–47. DOI: 10.1038/nmat1795 (cit. on p. 59).

[90] E. V. Lavrov, F. Herklotz, and J. Weber. “Identification of two hydrogen donors in ZnO”. In: *Phys. Rev. B - Condens. Matter Mater. Phys.* 79.16 (2009), pp. 1–13. DOI: 10.1103/PhysRevB.79.165210 (cit. on p. 59).

[91] F. Mohammadbeigi, E. S. Kumar, S. Alagha, I. Anderson, and S. P. Watkins. “Carbon related donor bound exciton transitions in ZnO nanowires”. In: *J. Appl. Phys.* 116.5 (Aug. 2014), p. 053516. DOI: 10.1063/1.4892090 (cit. on p. 62).

[92] S. T. Tan, X. W. Sun, Z. G. Yu, et al. “p-type conduction in unintentional carbon-doped ZnO thin films”. In: *Appl. Phys. Lett.* 91.7 (Aug. 2007), p. 072101. DOI: 10.1063/1.2768917 (cit. on p. 62).

[93] X. Li, S. E. Asher, S. Limpijumnong, et al. “Unintentional doping and compensation effects of carbon in metal-organic chemical-vapor deposition fabricated ZnO thin films”. In: *J. Vac. Sci. Technol. A Vacuum, Surfaces, Film.* 24.4 (June 2006), p. 1213. DOI: 10.1116/1.2167981 (cit. on p. 62).

[94] K. Tang, S. Gu, S. Zhu, et al. “Carbon clusters in N-doped ZnO by metal-organic chemical vapor deposition”. In: *Appl. Phys. Lett.* 93.13 (Sept. 2008), p. 132107. DOI: 10.1063/1.2992197 (cit. on p. 62).

[95] K. Tang, S. Gu, S. Zhu, et al. “Suppression of compensation from nitrogen and carbon related defects for p-type N-doped ZnO”. In: *Appl. Phys. Lett.* 95.19 (Nov. 2009), p. 192106. DOI: 10.1063/1.3262965 (cit. on p. 62).

[96] S. Limpijumnong, X. Li, S.-H. Wei, and S. B. Zhang. “Substitutional diatomic molecules NO, NC, CO, N2, and O2: Their vibrational frequencies and effects on p doping of ZnO”. In: *Appl. Phys. Lett.* 86.21 (May 2005), p. 211910. DOI: 10.1063/1.1931823 (cit. on p. 62).

[97] F. Mohammadbeigi. “Optical Characterization of Doped Zinc Oxide Nanowires”. In: *Thesis* (2017) (cit. on p. 62).

[98] L. Zhu, M. R. Phillips, and C. Ton-That. “Coalescence of ZnO nanowires grown from monodisperse Au nanoparticles”. In: *CrystEngComm* 17.27 (July 2015), pp. 4987–4991. DOI: 10.1039/C5CE00579E (cit. on p. 62).

[99] P. Wiesner and U. Heim. “Dynamics of exciton-polariton recombination in CdS”. In: *Phys. Rev. B* 11.8 (Apr. 1975), p. 3071. DOI: 10.1103/PhysRevB.11.3071 (cit. on p. 71).

[100] V. A. Kiselev, B. S. Razbirin, and I. N. Uraltsev. “Additional waves and Fabry-Perot interference of photoexcitons (polaritons) in thin II–VI crystals”. In: *Phys. Status Solidi* 72.1 (1975), pp. 161–172. DOI: 10.1002/pssb.2220720117 (cit. on p. 71).

[101] Y. Chen, F. Bassani, J. Massies, C. Deparis, and G. Neu. “Interference of the exciton-polariton waves in gaas thin layers.” In: *Epl* 14.5 (1991), pp. 483–488. DOI: 10.1209/0295-5075/14/5/016 (cit. on p. 71).

[102] A. Tredicucci, Y. Chen, F. Bassani, et al. “Center-of-mass quantization of excitons and polariton interference in GaAs thin layers”. In: *Phys. Rev. B* 47.16 (Apr. 1993), p. 10348. DOI: 10.1103/PhysRevB.47.10348 (cit. on p. 71).

[103] T. Mita and N. Nagasawa. “Anomalous wave interference at Z3-exciton resonance of CuCl”. In: *Solid State Commun.* 44.7 (1982), pp. 1003–1006. DOI: 10.1016/0038-1098(82)90322-2 (cit. on p. 71).

[104] B. Foy, E. McGlynn, A. Cowley, P. J. McNally, and M. O. Henry. “Study of exciton-polariton modes in nanocrystalline thin films of CuCl using reflectance spectroscopy”. In: *J. Appl. Phys.* 112.3 (2012). DOI: 10.1063/1.4739726 (cit. on pp. 71, 77, 79, 80).

[105] E. D. Sim, J. H. Song, and S. K. Chang. “Center-of-mass quantization of excitons and Fabry-Perot modes of the polariton in ZnSe epilayers”. In: *Solid State Commun.* 121.9-10 (2002), pp. 513–517. DOI: 10.1016/S0038-1098(02)00047-9 (cit. on p. 71).

[106] S. Kéna-Cohen and S. R. Forrest. “Room-temperature polariton lasing in an organic single-crystal microcavity”. In: *Nat. Photonics 2010 46* 4.6 (Apr. 2010), pp. 371–375. DOI: 10.1038/nphoton.2010.86 (cit. on p. 71).

[107] S. I. Pekar. “Supplementary light waves in crystals and exciton absorption”. In: *Sov. Phys. Uspekhi* 5.3 (Mar. 1962), p. 515. DOI: 10.1070/PU1962V005N03ABEH003435 (cit. on p. 71).

[108] D. G. Thomas and J. J. Hopfield. “Exciton Spectrum of Cadmium Sulfide”. In: *Phys. Rev.* 116.3 (Nov. 1959), p. 573. DOI: 10.1103/PhysRev.116.573 (cit. on p. 71).

[109] M. D. Fraser, S. Höfling, and Y. Yamamoto. “Physics and applications of exciton–polariton lasers”. In: *Nat. Mater. 2016 1510* 15.10 (Sept. 2016), pp. 1049–1052. DOI: 10.1038/nmat4762 (cit. on p. 71).

[110] J. Kasprzak, M. Richard, S. Kundermann, et al. “Bose–Einstein condensation of exciton polaritons”. In: *Nat. 2006 4437110* 443.7110 (Sept. 2006), pp. 409–414. DOI: 10.1038/nature05131 (cit. on p. 71).

[111] A. Imamoglu, R. J. Ram, S. Pau, and Y. Yamamoto. “Nonequilibrium condensates and lasers without inversion: Exciton-polariton lasers”. In: *Phys. Rev. A* 53.6 (June 1996), p. 4250. DOI: 10.1103/PhysRevA.53.4250 (cit. on p. 71).

[112] H. Deng, G. Weihs, D. Snoke, J. Bloch, and Y. Yamamoto. “Polariton lasing vs. photon lasing in a semiconductor microcavity”. In: *Proc. Natl. Acad. Sci.* 100.26 (Dec. 2003), pp. 15318–15323. DOI: 10.1073/PNAS.2634328100 (cit. on p. 71).

[113] G. Malpuech, A. D. Carlo, A. Kavokin, et al. “Room-temperature polariton lasers based on GaN microcavities”. In: *Appl. Phys. Lett.* 81.3 (July 2002), p. 412. DOI: 10.1063/1.1494126 (cit. on p. 71).

[114] P. Bhattacharya, T. Frost, S. Deshpande, et al. “Room Temperature Electrically Injected Polariton Laser”. In: *Phys. Rev. Lett.* 112.23 (June 2014), p. 236802. DOI: 10.1103/PhysRevLett.112.236802 (cit. on p. 71).

[115] C. Schneider, A. Rahimi-Iman, N. Y. Kim, et al. “An electrically pumped polariton laser”. In: *Nat. 2013 4977449* 497.7449 (May 2013), pp. 348–352. DOI: 10.1038/nature12036 (cit. on p. 71).

[116] E. McGlynn, J. Fryar, M. O. Henry, et al. “Exciton–polariton behaviour in bulk and polycrystalline ZnO”. In: *Phys. B Condens. Matter* 340-342 (Dec. 2003), pp. 230–234. DOI: 10.1016/J.PHYSB.2003.09.019 (cit. on p. 71).

[117] J. Fryar, E. McGlynn, M. O. Henry, and J. P. Mosnier. “Study of exciton-polariton modes in nanocrystalline thin films of ZnO using reflectance spectroscopy”. In: *Nanotechnology* 16.11 (2005), pp. 2625–2632. DOI: 10.1088/0957-4484/16/11/026 (cit. on pp. 71, 77, 79, 80, 83).

[118] M. Rosenzweig. “Optische Eigenschaften exzitonischer Polaritonen in ZnO”. PhD thesis. 1975 (cit. on p. 71).

[119] A. A. Toropov, O. V. Nekrutkina, T. V. Shubina, et al. “Temperature-dependent exciton polariton photoluminescence in ZnO films”. In: *Phys. Rev. B - Condens. Matter Mater. Phys.* 69.16 (2004), pp. 1–4. DOI: 10.1103/PhysRevB.69.165205 (cit. on p. 71).

[120] J. Wrzesinski and D. Fröhlich. “Two-photon and three-photon spectroscopy of ZnO under uniaxial stress”. In: *Phys. Rev. B - Condens. Matter Mater. Phys.* 56.20 (1997), pp. 13087–13093. DOI: 10.1103/PhysRevB.56.13087 (cit. on pp. 75, 82).

[121] M. Cobet, C. Cobet, M. R. Wagner, et al. “Polariton effects in the dielectric function of ZnO excitons obtained by ellipsometry”. In: *Appl. Phys. Lett.* 96.3 (Jan. 2010), p. 031904. DOI: 10.1063/1.3284656 (cit. on pp. 75, 83).

[122] M. R. Wagner, G. Callsen, J. S. Reparaz, et al. “Effects of strain on the valence band structure and exciton-polariton energies in ZnO”. In: *Phys. Rev. B - Condens. Matter Mater. Phys.* 88.23 (Dec. 2013), p. 235210. DOI: 10.1103/PHYSREVB.88.235210/FIGURES/9/MEDIUM. arXiv: 1312.0529 (cit. on pp. 75, 83).

[123] C. Kranert, C. Sturm, R. Schmidt-Grund, and M. Grundmann. “Raman tensor elements of β-Ga2O3”. In: *Sci. Reports 2016 61* 6.1 (Nov. 2016), pp. 1–9. DOI: 10.1038/srep35964 (cit. on p. 75).

[124] J. Fryar. “Optical and AFM Studies of ZnO: Excitonic Properties, Surface Morphology and Etching Effects”. PhD thesis. 2005 (cit. on pp. 77, 107).

[125] J. J. Hopfield and D. G. Thomas. “Theoretical and Experimental Effects of Spatial Dispersion on the Optical Properties of Crystals”. In: *Phys. Rev.* 132.2 (Oct. 1963), p. 563. DOI: 10.1103/PhysRev.132.563 (cit. on pp. 77, 79, 80).

[126] J. Lagois. “Dielectric theory of interacting excitonic resonances”. In: *Phys. Rev. B* 16.4 (Aug. 1977), p. 1699. DOI: 10.1103/PhysRevB.16.1699 (cit. on p. 77).

[127] J. Lagois. “Dielectric theory of interacting excitonic resonances”. In: *Phys. Rev. B* 16.4 (1977), pp. 1699–1705. DOI: 10.1103/PhysRevB.16.1699 (cit. on pp. 77, 79, 80, 83).

[128] G. van Rossum. *Python tutorial*. Jan. 1995 (cit. on p. 79).

Webpages

[@7] *Max von Laue - Biographical*. URL: https://www.nobelprize.org/prizes/physics/1914/laue/biographical/ (visited on Aug. 5, 2020) (cit. on p. 4).

[@8] *The Nobel Prize in Physics 1915*. URL: https://www.nobelprize.org/prizes/physics/1915/summary/ (visited on Mar. 7, 2021) (cit. on p. 4).

[@10] *Crystallography Open Database*. URL: http://www.crystallography.net/cod/ (visited on Aug. 5, 2020) (cit. on p. 5).

[@12] *Crystallography Open Database: Information card for entry 1011258*. URL: http://www.crystallography.net/cod/1011258.html (visited on Aug. 5, 2020) (cit. on p. 5).

[@24] *The Nobel Prize in Physics 2014*. URL: https://www.nobelprize.org/prizes/physics/2014/summary/ (visited on May 28, 2021) (cit. on p. 8).

[@43] *The Nobel Prize in Physics 1902*. URL: https://www.nobelprize.org/prizes/physics/1902/summary/ (visited on July 6, 2021) (cit. on p. 13).

[@52] *The Nobel Prize in Physics 1930*. URL: https://www.nobelprize.org/prizes/physics/1930/summary/ (visited on Sept. 2, 2019) (cit. on p. 19).

List of Figures

List of Tables

Appendix A

A.1 List of Publications

1. **Triple group-V donors in ZnO**
   M. Hegde, F. Mohammadbeigi, T. Kure, E. Senthil Kumar, M. R. Wagner, A. Hoffmann, S. P. Watkins
   Journal of Applied Physics **127**, 075705 (2020)
   DOI: 10.1063/1.5144203

2. **Auger recombination in AlGaN quantum wells for UV light-emitting diodes**
   F. Nippert, M. T. Mazraehno, M. J. Davies, M. P. Hoffmann, HJ. Lugauer, T. Kure, M. Kneissl, A. Hoffmann, M. R. Wagner
   Appl. Phys. Lett. **113**, 071107 (2018)
   DOI: 10.1063/1.5044383

3. **Electronic excitations stabilized by a degenerate electron gas in semiconductors**
   C. Nenstiel, G. Callsen, F. Nippert, T. Kure, S. Schlichting, N. Jankowski, M.P. Hoffmann, A. Dadgar, S. Fritze, A. Krost, M. R. Wagner, A. Hoffmann, F. Bechstedt
   Commun Phys **1**, 38 (2018)
   DOI: 10.1038/s42005-018-0033-4

4. **Excited states of neutral donor bound excitons in GaN**
   G. Callsen, T. Kure, M. R. Wagner, R. Butté, N. Grandjean
   Journal of Applied Physics **123**, 215702 (2018)
   DOI: 10.1063/1.5028370

5. **Influence of carbon doping and hydrogen co-doping on acceptor related optical transitions in ZnO nanowires**
   F. Mohammadbeigi, T. Kure, G. Callsen, E. Senthil Kumar, M.R. Wagner, A. Hoffmann, S.P. Watkins
   Semicond. Sci. Technol. **32** 045017 (2017)
   DOI: 10.1088/1361-6641/aa600e

6. **Intrinsic electronic properties of high-quality wurtzite InN**
   H. Eisele, J. Schuppang, M. Schnedler, M. Duchamp, C. Nenstiel, V. Portz, T. Kure, M. Bügler, A. Lenz, M. Dähne, A. Hoffmann, S. Gwo, S. Choi, J.S. Speck, R.E. Dunin-Borkowski, Ph. Ebert
   Phys. Rev. B **94**, 245201 (2016)
   DOI: 10.1103/PhysRevB.94.245201

7. **Temperature-dependent recombination coefficients in InGaN light-emitting diodes: Hole localization, Auger processes, and the green gap**
   F. Nippert, S. Y. Karpov, G. Callsen, B. Galler, T. Kure, C. Nenstiel, M. R. Wagner, M. Straßburg, HJ. Lugauer, A. Hoffmann
   Appl. Phys. Lett. **109**, 161103 (2016)
   DOI: 10.1063/1.4965298

8. **Polarization-induced confinement of continuous hole-states in highly pumped, industrial-grade, green InGaN quantum wells**
   F. Nippert, A. Nirschl, T. Schulz, G. Callsen, I. Pietzonka, S. Westerkamp, T. Kure, C. Nenstiel, M. Strassburg, M. Albrecht, A. Hoffmann
   Journal of Applied Physics **119**, 215707 (2016)
   DOI: 10.1063/1.4953254

9. **Determination of recombination coefficients in InGaN quantum-well light-emitting diodes by small-signal time-resolved photoluminescence**
   F. Nippert, S. Y. Karpov, I. Pietzonka, B. Galler, A. Wilm, T. Kure, C. Nenstiel, G. Callsen, M. Straßburg, HJ. Lugauer, A. Hoffmann
   Jpn. J. Appl. Phys. **55** 05FJ01 (2016)
   DOI: 10.7567/JJAP.55.05FJ01

10. **Analysis of the exciton–LO-phonon coupling in single wurtzite GaN quantum dots**
    G. Callsen, G. MO. Pahn, S. Kalinowski, C. Kindel, J. Settke, J. Brunnmeier, C. Nenstiel, T. Kure, F. Nippert, A. Schliwa, A. Hoffmann, T. Markurt, T. Schulz, M. Albrecht, S. Kako, M. Arita, Y. Arakawa
    Phys. Rev. B **92**, 235439 (2015)
    DOI: 10.1103/PhysRevB.92.235439

11. **Germanium–the superior dopant in n-type GaN**
    C. Nenstiel, M. Bügler, G. Callsen, F. Nippert, T. Kure, S. Fritze, A. Dadgar, H. Witte, J. Bläsing, A. Krost, A. Hoffmann
    Phys. Status Solidi RRL, **9**: 716-721 (2015)
    DOI: 10.1002/pssr.201510278

12. **Phonon pressure coefficients and deformation potentials of wurtzite AlN determined by uniaxial pressure-dependent Raman measurements**
G. Callsen, M.R. Wagner, J.S. Reparaz, F. Nippert, T. Kure, S. Kalinowski, A. Hoffmann, M.J. Ford, M.R. Phillips, R.F. Dalmau, R. Schlesser, R. Collazo, Z. Sitar
Phys. Rev. B **90**, 205206 (2014)
DOI: 10.1103/PhysRevB.90.205206

13. **Non-polar GaN quantum dots integrated into high quality cubic AlN microdisks**
M. Bürger, G. Callsen, T. Kure, A. Hoffmann, A. Pawlis, D. Reuter, D.J. As
Phys. Status Solidi C, **11**: 790-793. (2014)
DOI: doi.org/10.1002/pssc.201300411

14. **Identification of electric dipole moments of excitonic complexes in nitride-based quantum dots**
G. Hönig, S. Rodt, G. Callsen, I. A Ostapenko, T. Kure, A. Schliwa, C. Kindel, D. Bimberg, A. Hoffmann, S. Kako, Y. Arakawa
Phys. Rev. B **88**, 045309 (2013)
DOI: 10.1103/PhysRevB.88.045309

15. **Lasing properties of non-polar GaN quantum dots in cubic aluminum nitride microdisk cavities**
M. Bürger, G. Callsen, T. Kure, A. Hoffmann, A. Pawlis, D. Reuter, D.J. As
Appl. Phys. Lett. **103**, 021107 (2013)
DOI: 10.1063/1.4813408

16. **Compensation effects in GaN: Mg probed by Raman spectroscopy and photoluminescence measurements**
R.Kirste, M. P. Hoffmann, J. Tweedie, Z. Bryan, G. Callsen, T. Kure, C. Nenstiel, M. R. Wagner, R. Collazo, A. Hoffmann, Z. Sitar
Journal of Applied Physics 113, 103504 (2013)
DOI: 10.1063/1.4794094

17. **Optical signature of Mg-doped GaN: Transfer processes**
G. Callsen, M.R. Wagner, T. Kure, J.S. Reparaz, M. Bügler, J. Brunnmeier, C. Nenstiel, A. Hoffmann, M. Hoffmann, J. Tweedie, Z. Bryan, S. Aygun, R. Kirste, R. Collazo, Z. Sitar
Phys. Rev. B **86**, 075207 (2012)
DOI: 10.1103/PhysRevB.86.075207

18. **Temperature dependent photoluminescence of lateral polarity junctions of metal organic chemical vapor deposition grown GaN**
R. Kirste, R. Collazo, G. Callsen, M. R. Wagner, T. Kure, J. S. Reparaz, S. Mita, J. Xie, A. Rice, J. Tweedie, Z. Sitar, A. Hoffmann
Journal of Applied Physics 110, 093503 (2011)
DOI: 10.1063/1.3656987

A.2 Python code for the reflectance modeling

For the modeling of the reflection in chapter 6.3, the setup of the model function as well as the fitting routine is necessary. The code used has been ported from MATLAB code presented in Fryar et al. [124] into python code.

A.2.1 Definition of model 1 and 2

```python
# Fit function ready for lmfit minimize
import numpy as np

def ref_modelling(data_x, model, LT_A, LT_B, width_A, width_B, m_star_A, m_star_B,
    e_inf, L, e_AL, e_BL, n_sub, slope, const):
    "fit_model 1 and 2"

    #parameters values
    # data_x: data in eV
    # LT_A: LT-splitting of A exciton in eV
    # LT_A: LT-splitting of B exciton in eV
    # width_A: width (damping) of A exciton in eV
    # width_B: width (damping) of B exciton in eV
    # m_star_A: effective mass exciton A (multiple of electron mass)
    # m_star_B: effective mass exciton B (multiple of electron mass)
    #e_inf: background dielectric constant
    #L: layer thickness
    #e_AL: energetic position of the long. A exciton in eV
    #e_BL: energetic position of the long. B exciton in eV

    #physical constants
    c = 2.998e8 # in m/s, speed of light
    e = 1.602e-19 # in C, elementary charge
    h_bar = 6.63e-34/(2*np.pi) # in Js, reduced Planck constant
    m_elec = 9.1e-31 # in kg, electron mass
    e_vac = 8.85e-12 # in C/(Vm), epsilon_0; vacuum permittivity

    #initial values
    w_AL = e_AL*e/h_bar # omega_LA in 1/s, w_l_a
    w_BL = e_BL*e/h_bar # omega_LB in 1/s, w_l_b
    gam_A = width_A*e/h_bar # Gamma_A (damping) in 1/s
    gam_B = width_B*e/h_bar # Gamma_B (damping) in 1/s
    m_eff_A = m_star_A*m_elec # effective mass exciton A in kg
    m_eff_B = m_star_B*m_elec # effective mass exciton B in kg

    w_AT = w_AL-LT_A*e/h_bar # w_o_a in 1/s
    w_BT = w_BL-LT_B*e/h_bar # w_o_b in 1/s

    b_A = h_bar*w_AT/m_eff_A
```

```
    b_B = h_bar*w_BT/m_eff_B

    #expressions
    a_A0 =
    ↪  e_inf*(e_vac/w_AT**2)*(w_BL**2-w_AT**2)*((w_AL**2-w_AT**2)/(w_BT**2-w_AT**2))
    a_B0 =
    ↪  e_inf*(e_vac/w_BT**2)*(w_AL**2-w_BT**2)*((w_BL**2-w_BT**2)/(w_AT**2-w_BT**2))

    fit_y = np.zeros_like(data_x)
    k1m = np.zeros_like(data_x)
    k2m = np.zeros_like(data_x)
    k3m = np.zeros_like(data_x)
    k1r = np.zeros_like(data_x)
    k2r = np.zeros_like(data_x)
    k3r = np.zeros_like(data_x)
    f21r = np.zeros_like(data_x)
    k22r = np.zeros_like(data_x)
    k23r = np.zeros_like(data_x)
    dcoeff = np.zeros_like(data_x)

    for count in range(data_x.size):
        w = data_x[count]*e/h_bar # w in 1/s

        A = (c**2)/(w**2)
        B = a_A0/e_vac*(w_AT**2)
        C = (w_AT**2)-(w**2)-(1j*w*gam_A)
        D = a_B0/e_vac*(w_BT**2)
        E = (w_BT**2)-(w**2)-(1j*w*gam_B)

        coeff = [A*b_A*b_B,
                 A*C*b_B+A*E*b_A-(e_inf*b_A*b_B),
                 A*C*E-(e_inf*C*b_B)-(e_inf*E*b_A)-(B*b_B)-(D*b_A),
                 -(e_inf*C*E+B*E+D*C)]
        term1 = ((w_AT**2)-(w**2)-(1j*w*gam_A)) #C
        term2 = ((w_BT**2)-(w**2)-(1j*w*gam_B)) #E

        k = np.sqrt(np.roots(coeff)) # p[0] * x**n + p[1] * x**(n-1) + ... +
        ↪  p[n-1]*x + p[n]

        if k[0].imag>0:
            k[0] = k[0]
        else: k[0] = -k[0]

        if k[1].imag>0:
            k[1] = k[1]
        else: k[1] = -k[1]

        if k[2].imag>0:
```

```
            k[2] = k[2]
        else: k[2] = -k[2]

        k1m[count]=k[0].imag
        k2m[count]=k[1].imag
        k3m[count]=k[2].imag

        k1r[count]=k[0].real #abs(k_1)
        k2r[count]=k[1].real #abs(k_2)
        k3r[count]=k[2].real #abs(k_3)

        n_1 = k[0]*c/w # n_a
        n_2 = k[1]*c/w # n_b
        n_3 = k[2]*c/w # n_c

        a_A1 = (a_A0*w_AT**2/e_vac)/(w_AT**2-w**2-1j*w*gam_A+b_A*w**2*n_1**2/c**2)
        a_A2 = (a_A0*w_AT**2/e_vac)/(w_AT**2-w**2-1j*w*gam_A+b_A*w**2*n_2**2/c**2)
        a_A3 = (a_A0*w_AT**2/e_vac)/(w_AT**2-w**2-1j*w*gam_A+b_A*w**2*n_3**2/c**2)

        a_B1 = (a_B0*w_BT**2/e_vac)/(w_BT**2-w**2-1j*w*gam_B+b_B*w**2*n_1**2/c**2)
        a_B2 = (a_B0*w_BT**2/e_vac)/(w_BT**2-w**2-1j*w*gam_B+b_B*w**2*n_2**2/c**2)
        a_B3 = (a_B0*w_BT**2/e_vac)/(w_BT**2-w**2-1j*w*gam_B+b_B*w**2*n_3**2/c**2)

        ###
        # For Model 2 (L Layer)
        e_1 = np.exp(1j*n_1*w*L/c) #d_a
        e_2 = np.exp(1j*n_2*w*L/c) #d_b
        e_3 = np.exp(1j*n_3*w*L/c) #d_c
        es_1 = np.exp(-1j*n_1*w*L/c) #d_a_1
        es_2 = np.exp(-1j*n_2*w*L/c) #d_b_2
        es_3 = np.exp(-1j*n_3*w*L/c) #d_c_3

        # Model 1 Air-ZnO-
        #matrix 1 (4x4)
        mat1 = np.matrix([[-1, 1, 1, 1],
                  [1, n_1, n_2, n_3],
                  [0, a_A1, a_A2, a_A3],
                  [0, a_B1, a_B2, a_B3]])
        v1 = np.matrix('1;1;0;0')

        # Model 2 Air-ZnO-MgZnO
        #matrix 2 (8x8)
        mat2 = np.matrix([[-1, 1, 1, 1, 1, 1, 1, 0],
                  [1, n_1, n_2, n_3, -n_1, -n_2, -n_3, 0],
                  [0, e_1, e_2, e_3, es_1, es_2, es_3, -1],
                  [0, n_1*e_1, n_2*e_2, n_3*e_3, -n_1*es_1, -n_2*es_2, -n_3*es_3,
                  ↪ -n_sub],
                  [0, a_A1, a_A2, a_A3, a_A1, a_A2, a_A3, 0],
```

```
                    [0, a_B1, a_B2, a_B3, a_B1, a_B2, a_B3, 0],
                    [0, a_A1*e_1, a_A2*e_2, a_A3*e_3, a_A1*es_1, a_A2*es_2,
                    ↪  a_A3*es_3, 0],
                    [0, a_B1*e_1, a_B2*e_2, a_B3*e_3, a_B1*es_1, a_B2*es_2,
                    ↪  a_B3*es_3, 0]])
         v2 = np.matrix('1;1;0;0;0;0;0;0')

        if model == 1:
            invmat = np.linalg.inv(mat1)
            v = invmat*v1
        elif model == 2:
            invmat = np.linalg.inv(mat2)
            v = invmat*v2

        r1 = v.item(0)
        fit_y[count] = abs(r1)**2*slope+const #fit_y Reflectance

    return fit_y, k1r, k2r, k3r, k1m, k2m, k3m;
```

A.2.2 Setup of the fitting routine

```
import numpy as np
import matplotlib.pyplot as plt
from lmfit import minimize, Parameters, fit_report
#install numdifftools package for errors

params = Parameters()
# add with tuples: (NAME, VALUE, VARY, MIN,  MAX,  EXPR,  BRUTE_STEP)
params.add_many(('LT_A', initial_1, True, 0.0001, 0.0025, None, None),
                ('LT_B', initial_2, True, 0.01, 0.020, None, None),
                ('width_A', initial_3, True, 0, 1, None, None),
                ('width_B', initial_4, True, 0, 1, None, None),
                ('m_star_A', initial_5, True, 0, 1, None, None),
                ('m_star_B', initial_6, True, 0, 1, None, None),
                ('e_inf', initial_7, True, 3, 4, None, None),
                ('L', 1.04e-06, False, 0, 1, None, None),
                ('e_AL', initial_8, True, 3.37, 3.38, None, None),
                ('e_BL', initial_9, True, 3.38, 3.40, None, None),
                ('n_sub', initial_10, True, 1, 3, None, None),
                ('slope', 1, True, -3, 3, None, None),
                ('const', 0, True, -1, 1, None, None),
                )

def iter_cb(params, iteration, resid, args, nan_policy='propagate',
↪  method='nelder'):
    #call after iteration
    chi = np.sum(resid**2)
```

```
26      print('\r', 'Iteration: ', iteration, '   Chi: ', chi, end='')
27
28  #Select model
29  model = 1
30
31  def residual(pars, data_x, data_y, model, eps=None):
32      # unpack parameters: extract .value attribute for each parameter
33      parvals = pars.valuesdict()
34
35      if eps is None:
36          model_r = ref_modelling(data_x, model, **parvals)[0]
37          return  model_r - data_y
38      return (ref_modelling(data_x, model, **parvals) - data_y) / eps;
39
40  fit_result = minimize(residual, params, args=(data_x, data_y, model),
    ↪  nan_policy='propagate', method='nelder', iter_cb=iter_cb,
    ↪  options={'maxiter':5000})
41
42  parvals = fit_result.params.valuesdict()
43  print(parvals)
44  result = parvals
45  print(fit_report(fit_result))
```

A.3 Additional Graphs

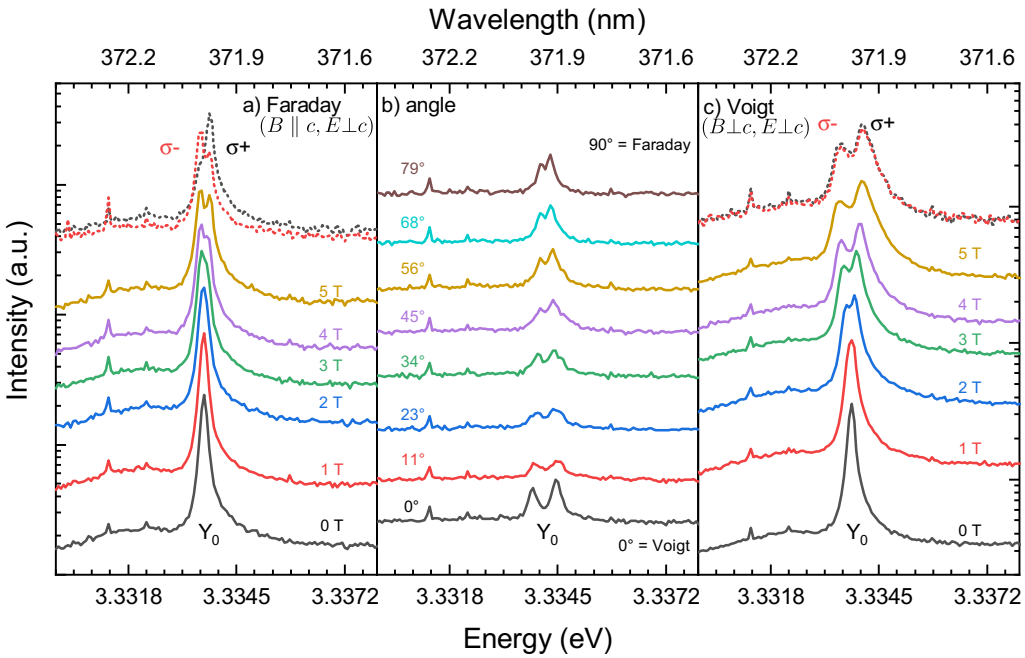

Fig. A.1.: Photoluminescence spectra for different magnetic fields in the Y_0-region a) Faraday configuration ($B \parallel c$). b) angle between B and c at 5 T c) Voigt configuration ($B \perp c$)

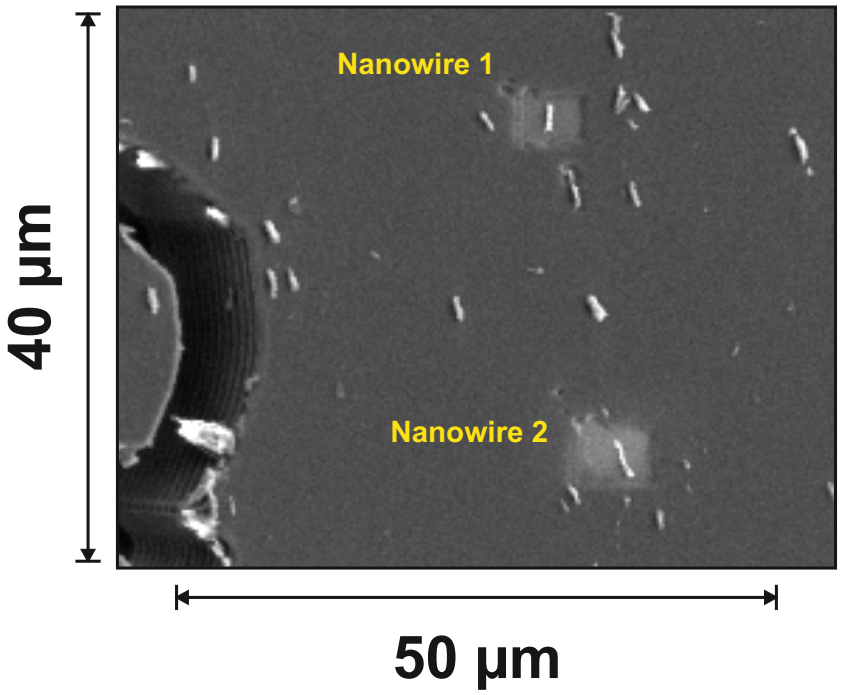

Fig. A.2.: Secondary-electron microscope (SEM) of Sb-doped ZnO nanowires taken after cathodoluminescence with scanning transmission electron microscopy (TEM-CL) measurements indicating damages of the substrate surface.

Acknowledgement

This thesis would not be possible without the support of people who helped me on my path. I would like to express my gratitude to:

- My adviser Prof. Dr. Axel Hoffmann who gave me the opportunity to continue my work in his group as a graduate student and for his support not only with my thesis but also with my career path in the Collaborative Research Center 787 (CRC 787).
- Prof. Dr. Markus R. Wagner for co-supervision of my thesis, his help, and input and all the fruitful discussions.
- Prof. Dr. Jean-Michel Chauveau for reviewing my thesis and taking part in my defense, as well as for providing the high quality MBE exciton-polariton sample.
- Prof. Dr. Michael Lehmann for chairing my defense.
- Prof. Dr. Simon Watkins, Dr. Senthil Kumar Eswaran, and Dr. Faezeh Mohammadbeigi for the collaboration on the ZnO nanowires, as well as the hospitality in Vancouver.
- Dr. Felix Nippert for sharing the office, long darts sessions, and his python-support.
- Daniela Beiße, Marco Haupt, Wolfgang Pieper, and Andreas Ludewig for the construction of all custom parts in the labs.
- Dr. Dirk Heinrich and Dr. Harald Scheel for the early morning coffee round to start the day.
- All former and current members of the working groups Hoffmann, Wagner, Maultzsch, and Thomsen
- My parents for their eternal support.
- My children Joshua, Emilia, and Malie. I love you all and I am so happy to have you in my life.